# Techniques to Leverage RF Signals for Context Sensing

by

**Phuc Nguyen**

B.S., University of Science, Vietnam National University, 2010

M.S., Sungkyunkwan University, 2014

A thesis submitted to the

Faculty of the Graduate School of the

University of Colorado in partial fulfillment

of the requirements for the degree of

Doctor of Philosophy

Department of Computer Science

2018

This thesis entitled:
Techniques to Leverage RF Signals for Context Sensing
written by Phuc Nguyen
has been approved for the Department of Computer Science

Prof. Tam Vu

Prof. Richard Han

Prof. Qin (Christine) Lv

Prof. Nikolaus Correll

Prof. Sriram Sankaranarayanan

Date

The final copy of this thesis has been examined by the signatories, and we find that both the content and the form meet acceptable presentation standards of scholarly work in the above mentioned discipline.

Nguyen, Phuc (Ph.D., Computer Science)

Techniques to Leverage RF Signals for Context Sensing

Thesis directed by Prof. Tam Vu

RF signals and devices have been used for wireless communication to improve the mobility and ubiquity of mobile devices. In this dissertation, we show that these RF signals can also be used for context sensing applications. Specifically, we present cyber-physical systems and algorithms to sense human vital signals, object vibrations and movements, and object's location to deliver new sensing capabilities for a variety of new applications including health-care monitoring, privacy protection, and indoor localization. We deliver three fundamental contributions. First, we develop an RF-based system to "sense" human breathing volume continuously in fine-grained from afar. Second, we develop a technique to "sense" the wireless signals emitted from drones/fly-cams to detect them and alert users for privacy protection. Last, we present our preliminary study on building a system to enable the mobile device to "sense" their global locations at the indoor environment. To deliver these contributions, we exploit the properties of physical characteristics of RF signals, analyze and understand targeted subjects behaviors (i.e., human, drones), work across different limitations and hardware-software barriers, and introduce novel systems and new algorithms to overcome the challenges. We implement and evaluate the system on real users/patients, test the systems across different environments, and demonstrate how they can enable many other real-world applications.

*To my family*

## Acknowledgements

I would like to express my sincere gratitude to many people who helped me during my Ph.D study. First, I am deeply grateful to my advisor, Professor Tam Vu, for his guidance and support throughout my Ph.D. study. Professor Vu gave me a perfect research environment where I can focus on research and pursue interesting projects. He imparts not only knowledge, but also methodologies for managing time, distilling innovative ideas, leading and mentoring other junior students, etc. He has also been a role-model for me in maintaining an energetic and enthusiastic state even under pressure situations. The spirits that I inherited from him will continue inspiring me throughout my career and life. I would also like to thank Professors Richard Han, Qin Li, Nicolaus Correl, Sriram Sankaranarayanan, and Eric Frew for serving on my thesis committee. I thank them for spending time to review the thesis and provide valuable feedback. I am thankful to colleagues in the Mobile and Networked Systems Laboratory (MNS) including Hoang Truong, Nam Bui, Anh Nguyen, Nhat Pham, and Taeho Kim who have contributed to the development of this thesis. I am also grateful to Shane Transue, Duy Pham, Vennela Gandluri, Ed Salisbury, Bradley Dufresne, Lily Dam, Sean Kuhlman, Cory Coellen, Michael Hunsinger, and Raphael O'Flynn for helping me with developing research prototype and user's interface for my developed systems. Last but not least, I wish to express my gratitude to my family, my parents Ren Nguyen and My Nguyen, my sister Huong Nguyen whose unconditional support has been the most important power that made me persevere throughout the past years. To them I dedicate this thesis.

# Contents

**Chapter**

# Figures

**Figure**

# Chapter 1

# Introduction

This thesis explores the use of RF signals for context sensing applications. In particular, we present techniques that utilize RF signals and devices to enable new sensing capabilities including *human sensing*, *objects sensing*, and *location sensing*. While the thesis focuses on the first two sensing capabilities, we would like to also present a feasibility of using RF signal to allow mobile devices to sense their indoor locations. These sensing capabilities can be used for three domain applications including 1) *health-care*, 2) *privacy protection* and 3) *emergency response*. Specifically, we first demonstrate the feasibility of using RF signal to sense human by developing an unobtrusive RF system to monitor human vital signs (breathing volume) during sleep. The RF system includes a wireless transmitter to send out an RF signal, this signal then hits the human chest and bounces off. The bounced off signal is captured by the wireless receiver and extract the human breathing volume. The system does not require a user to wear any sensor/device. Second, we demonstrate the feasibility of sensing object using RF signal by developing a system to detect their presence for protecting user's privacy. The proposed system examines whether physical characteristics of the drone can be detected in the wireless signal transmitted by drones during communication. Last but not least, we would like to present a preliminary study on design system to make GPS signal available inside the building for enabling GPS-enabled devices to sense their global locations to help firefighters and 911 callers to continuously track their locations in emergency scenarios.

There are many challenges preventing us from realizing these systems. First, the signal of interests (human vital signals, drone vibration, etc.) are usually very weak and buried under the

noises floor. Second, sensing the human or object from afar is challenging because the wireless signal drops quickly over distance. Third, since the RF band is unlicensed, it is heavily used by others such as Wi-Fi devices, there will be a lot of interference in the environment. Last but not least, the systems will be deployed at urban environments with buildings around in which RF interference and multi-path maybe exacerbated.

Beside algorithm innovations, addressing the above challenges require designing hardware and software systems that allow us to fully control each component in the system. For example, to sense the human chest movements to infer breathing volume during sleep, the RF transmitter, receiver, mechanical movements need to be synchronized so that the signal will always hit the monitored human chest area for accurate monitoring. As another example, to detect the presence of the drones, we had to carefully analyze the signal at different stages of RF receiver stack (RF front end, base-band data, etc.) to identify the drone's physical signature for reliable detection.

The combination of algorithms and hardware-software systems allow us to fully utilize RF signals for new sensing capabilities. Our designs have the followings advantages: First, there is no need for a specific assumption for the testing environment. The system has to deal with all of the challenges of the wireless signal and targeted subject, i.e., noises, power reduction over distance, human body movement, unpredictable drone's vibrations and movements, and so on. Second, we built the prototypes using COTS components that are available around us. And last, the system is implemented and evaluated on real-users, different environments, settings, conditions to validate the practicality of the solution, and demonstrate their feasibility and high accuracy.

## 1.1 Research Areas and Contributions

Utilizing the ubiquity of RF signals and devices around us, my research focus on using these signals to enable unconventional context sensing applications. Below, I highlight the contributions of each of these systems in chronological order of their development:

**Sensing human breathing volume using RF signals.** We propose an autonomous system, called WiSpiro, that continuously monitors individual's *breathing volume* with high resolution dur-

ing sleep from afar. Breathing volume has been widely used as an important indication for diagnosis and treatment of pulmonary diseases and other health care related issues such as critically ill patients neonatal ventilation, post-operative monitoring and various others. Most of existing technologies for respiration volume monitoring require physical contact with the human body. WiSpiro

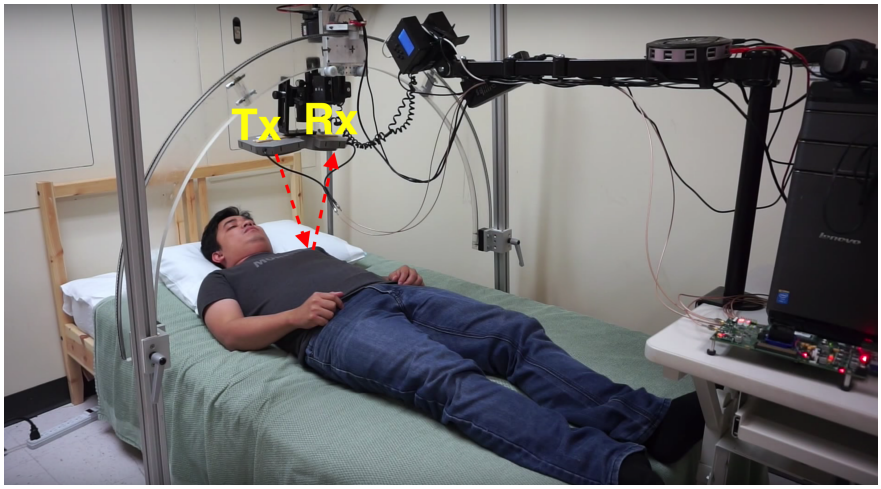


Figure 1.1: WiSpiro is a system to monitor breathing volume continuously in fine-grained using wireless signal. WiSpiro includes a transmitter antenna sending out 2.4 GHz signal. This signal is then reflected off the human body and captured by a receiver. By observing the phase variation of the reflected signal, WiSpiro calculates the chest movements and then infers to breathing volume. https://youtu.be/APqgPOxlfIs.

relies on a phase-motion demodulation algorithm that reconstructs minute chest and abdominal movements by analyzing the subtle phase changes that the movements cause to the continuous wave signal sent by a 2.4 GHz directional radio. These movements are mapped to breathing volume, where the mapping relationship is obtained via a short training process. To cope with body movement, the system tracks the large-scale movements and posture changes of the person by analyzing the received signal strength and phase changes of the signal, and moves its transmitting antenna accordingly to a proper location in order to maintain its beam to specific areas on the frontal part of the person's body. It also incorporates interpolation mechanisms to account for possible inaccuracy of our posture detection technique and the minor movement of the person's body. We have built WiSpiro prototype, and demonstrated through a user study that it can accurately and continuously monitor user's breathing volume with a median accuracy from 90% to 95.4% (or 0.058$l$ to 0.11$l$ of

error) to even in the presence of body movement. The monitoring granularity and accuracy are sufficiently high to be useful for diagnosis by clinical doctor.

**Sensing drones presence by identifying their signatures from RF signals.** Drones are increasingly flying in sensitive airspace where their presence may cause harm, such as near airports, forest fires, large crowded events, secure buildings, and even jails. This problem is likely to expand given the rapid proliferation of drones for commerce, monitoring, recreation, and other applications. A cost-effective detection system is needed to warn of the presence of drones in such cases. We


Figure 1.2: Matthan is a system to detect the presence of the drone by recognizing its body shifting and body vibration signature utilizing RF AP architecture. In particular, Matthan receiver captures the signal emitted from RF transmitters in the surrounding environment, and then analyzes the captured signals to detect the presence of drones to alert and protect their privacy. https://youtu.be/id2LxOsr_G8.

explore the feasibility of inexpensive RF-based detection of the presence of drones. We examine whether physical characteristics of the drone, such as body vibration and body shifting, can be detected in the wireless signal transmitted by drones during communication. We consider whether the received drone signals are uniquely differentiated from other mobile wireless phenomena such as cars equipped with Wi-Fi or humans carrying a mobile phone. The sensitivity of detection at distances of hundreds of meters as well as the accuracy of the overall detection system are evaluated using software defined radio (SDR) implementation.

**Exploring the feasibility of sensing indoor location leveraging forwarded GPS signal.** While outdoor localization needs have been largely met by satellite-based positioning systems (e.g.,

GPS), indoor localization has not been able to take advantage of these systems since GPS signals are often too weak or unavailable indoor. To fill in that gap, we explore the feasibility of developing a global in-building positioning system that utilizes the ubiquity of Wi-Fi Access Points (APs) to relay GPS signals from outdoor to indoor environments. The proposed system will allow off-the-shelf GPS-enabled devices to localize their own global positions in 3-dimensional space (3D). Its key enabling techniques are two fold: a hardware add-on and accompanied algorithms. Steamed from an observation on the modern Wi-Fi AP hardware architecture, a plug-n-play hardware add-on is introduced to allow existing Wi-Fi APs to receive and relay GPS signal, making it available inside the building. A series of localization algorithms allow the GPS-enabled mobile device to convert

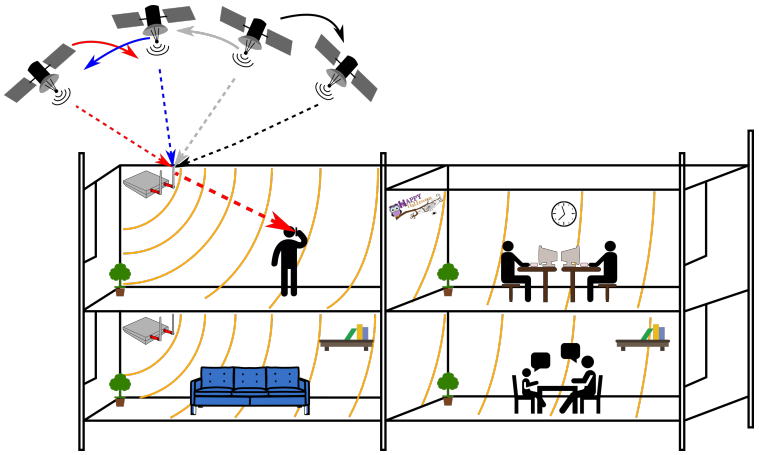

Figure 1.3: We explore a system to relay GPS signal from outdoor to indor allowing user to localize their global location continuously. The proposed system includes a plug-n-play add-on attached to Wi-Fi AP access point, which relay GPS signal from outdoor to indoor and localization algorithms allowing receiver to accurately localize its location.

these relayed GPS signals into an accurate 3D location. We prototype the system's hardware and GPS receiver software to validate the feasibility of using the system. The preliminary results show that the proposed system obtains a median error in 3D space of *1.038m* and *2.304m* at 95%, ±6 degree error in azimuth estimation, and ±5 degree error in elevation estimation.

## 1.2 Beyond the developed systems

The dissertation explores the use of RF signals as sensing tools to solve a variety of societal and technological challenges. Nonetheless, the synergies identified during this thesis between RF systems, other computer science communities (mechanical engineering, vision, localization) extend beyond the problems addressed in this thesis. This dissertation contributes the foundation for an on-going exploration, we believe RF sensing research will expand and grow.

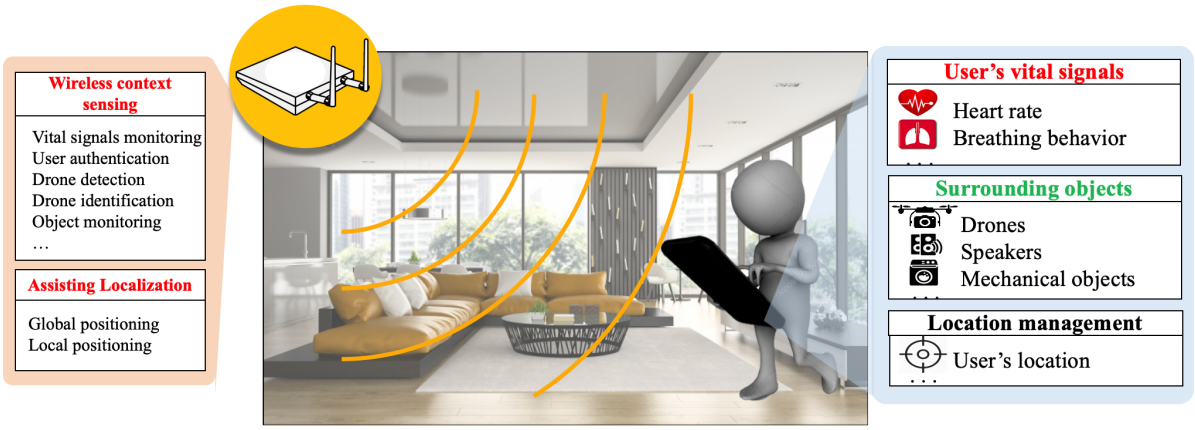


Figure 1.4: Techniques to Leverage RF Signals for Context Sensing

Fig. 1.4 illustrates a new generation of RF devices (e.g., Wi-Fi AP) that supports a variety of wireless sensing and positioning capabilities. Specifically, Wi-Fi AP is designed to monitor 1) user's health condition (e.g., vital signals, activities), 2) user's bio identification (e.g., heart rate and breathing patterns), 3) status of the surrounding environments (e.g., machines are operating such as coffee maker, washing, dryer, speakers, and even drones flying around), and support 4) user to localize their global and local positioning.

On user's side, upon receiving the monitored vital signals from RF devices (e.g., Wi-Fi AP) (Fig. 1.4 right), user's mobile devices will use these signals for different types of applications including 1) vital signals monitoring, 2) breathing analysis, 3) heart failure monitoring, and so on. This will cut the cost of hospitalization significantly as the user can monitor their health everywhere they go (office, home, coffee shop). Next, the user will know when coffee is made, washing and drying tasks are done, and which drones are around. Lastly, the user can globally and locally

localize their locations continuously.

## 1.3 Existing Literature

**Non-contact vital sign sensing:** Radar technique has been widely used in estimating vital signs. The frequency and phase shift of body-reflected radar signals have be used to estimated the heart and breathing rate [1, 2, 3, 4]. Droidcour *et al.* [5] introduce a linear correlation model to approximate the chest movement based on phase information. Linearity holds only if the movement is much smaller compared with the wavelength so that the chest movement is linearly proportional to the phase change. Using this approach, breathing rate and heart beat can be extracted by analyzing the received signal on frequency domain. Changi *et al.* [6] analyze the breathing activities using Fourier series and exploit the harmonics information to obtain the respiration rate and heart beat regardless of the distance from subject to radar. The dependency of movement and wavelength of the signal has also been resolved. Adib [7] used FMCW technique to collect the change of distance between radar to multiple objects and infer their breathing rates based on the traveling time of the signal. These approaches triggered substantial investigation along the same line. In addition, Patwari *et al.* [3] presented the feasibility of using Wi-Fi of the shelf device to track respiration rate in real time. However, breathing volume estimation, a problem equally important to medical practitioners, has not been thoroughly solved. Early efforts in tidal volume estimation (*e.g.*, [8]) focused on controlled settings and short-term monitoring, which is of less clinical significance. To our knowledge, our breathing volume estimation marks the first step to systematically investigate the problem under practical settings involving body area heterogeneity, body movement, etc.

**Non-contact object (drone) sensing:** Multiple sensing modalities have been employed for detecting objects (including drones), including audio, video and RF. First, an acoustic approach collects a database of acoustic signatures from different drones and uses this database to compare with observed sound signals to make a decision [9]. Challenges to this approach include detection accuracy in noisy urban environments and at distance, keeping this database updated, and new quieter drone models [10]. Second, a video-based solution employs a camera to detect drones [11].

Challenges to this approach include operation at night, compute-intensive image processing that must distinguish between a drone and say a bird at distance, and occlusion by buildings that limit distance in an urban environment. Thermal cameras have been proposed to detect drones at night [12] but are a relatively expensive technique.

A variety of RF-based solutions have been proposed for drone detection. One approach is to monitor the 1MHz - 6.8GHz band, and any unknown transmitter is assumed to be a drone [13]. This would suffer from false positives. Another approach is MAC address collection and analysis [14], but this can be bypassed easily by spoofing the MAC address. The frequency of packet communication on the uplink and downlink between the drone and its controller has also been used for detection[15]. However, other periodic packet sources at similar rates such as VOIP traffic could be mistaken as drone communication. Radar-based techniques actively transmit RF waves and look for the reflection to determine the presence of the drone. WiDop [16] is a non-coherent radar system which exploits the modulation produced by a target in a clutter with a non-coherent X-band radar. WiDop is claimed to have advantages over a coherent radar in terms of low cost radar and high range, but there exist disadvantages due to the radar angle and lack of high precision. Another radar technique is passive bistatic radar [17, 18, 19, 20, 21], which consists of a passive receiver to process a received signal from a known source of transmission and reflected signals from the moving target. These systems have advantages of low cost, fast update of the target position and variable frequency allocation. In conjunction with the usage of abundant WiFi sources as reference transmitters, multiple algorithms [22, 23] have been proposed for signal processing in passive bistatic radar systems such as MTI and LS adaptive filters [24] or compressive sensing [25]. Moreover, multistatic radar [26, 27], which includes more than two receivers, is also used to detect flying objects by calculating the radar cross section. The use of multiple receivers increase the accuracy of the system. Radar generally introduces interference due to active transmissions, which is especially problematic when there is a large amount of legitimate packet traffic over RF bands such as Wi-Fi, especially in crowded environments.

**Indoor global position sensing:** For indoors, the naive solution is using pseudo satellite or

so-called pseudolite architectures [28, 29, 30, 31, 32, 33, 34]. In this technique, GPS signals are received and replayed with amplification to be able to transmit inside a building. The indoor transmitters are placed at corners to gather the strongest GPS signals and then starts forwarding. Receivers might not be able to identify the incoming signal clearly because it can be distorted after reflecting from multiple transmitters. In order to fill the gap, transmitters should take turn forwarding the signals considering their relative positions. The cycling approach is called repeaters [35]. The more advanced solution, namely repealites combining the repeaters and peseudolites to establish a flexible transmission scheme [36, 37, 38, 39, 40, 41, 42, 43]. Each transmitter does not need to follow the sequential mode. Instead it plans to avoid interference with packages sent by the previous repealites. The authors in [44] propose to extract each satellite signal from the GPS signals and deliver through the indoor antennas. Recently, COIN-GPS [45] tries to achieve direct GPS-based indoor localization using a steerable, high-gain directional antenna and leverages the advantage of CO-GPS [46] to offload the computation to the cloud for robust signal acquisition.

Due to limitation of GPS, several works have explored other types of signals to carry longitude and latitude information. In [47], the authors take advantage of ADS-B, an aircraft signal, which is strong enough to be captured inside buildings. However, the technique does not work with existing mobile devices at the moment. GSM signal is another option to locate indoor objects. For example, the authors of [48, 49, 50, 51, 52, 53, 54, 55] show their attempt to utilize GSM signals in various ways to perform the indoor localization. However, the accuracy is around 30 meters [49] which are not adequate for localization in a less than 10-story building. Bluetooth GPS spoofing [56] is one solution to send the fake GPS signal to the mobile device via Bluetooth connection using NMEA message format. This won't work with device only support GPS chip. Other approaches leverage FM signals [57, 58, 59, 60, 61, 62, 63, 64] and visible light [65, 66, 67, 68, 69, 70, 71, 72, 56] to perform the indoor positioning. The error distance under the FM technique is less than 10 meters at 87% confidence level.

There have been many localization efforts using Wi-Fi signals including SpotFi [73], Tone-Track [74], Phaser [75], Tagoram [76], LTEye [77], ArrayTrack [78] and others [79, 80, 81, 82, 83, 84]

to detect the angle and/or distance between Wi-Fi AP and clients, both of which should be equipped with multiple antennas. Among others, Chronos [85] allows two Wi-Fi devices to approximate their distance precisely at decimeter accuracy. However, this system requires two devices to connect to each other to exchange packets for ToF measurement as well as for synchronization between multiple frequency bands. all the above approaches assume that the location of the APs are known from offline to calculate the location of the target device. In contrast, our work doesn't impose any communication channels between the two devices. The Wi-Fi AP simply acts as a relay to repeat the GPS signal from outdoor to indoor and the user device runs its dedicated localization component upon the receipt of the relayed GPS signal.

## 1.4 Thesis Organization

The remainder of this dissertation is organized as follows. In Chapter 2, we introduce a system that utilizes Wi-Fi signal to continuous and fine-grained monitor human breathing volume. In Chapter 3, we describe how Wi-Fi signal emitted from an object can be used to analyze its physical characteristics. In particular, we show how could we detect the presence of the drones to protect user's privacy and safety. In Chapter 4 we present a preliminary study on developing technique to allow mobile devices to sense their location with indoor environment for protecting user safety especially emergency scenarios. Finally, Chapter 5 summarizes the contribution of this dissertation and proposes future work.

# Chapter 2

# Continuous and Fine-grained Breathing Volume Monitoring from Afar Using RF Signals

## 2.1 Introduction

Monitoring patient tidal volume can be effectively used to extract important indicators of pulmonary and other medical conditions that are identifiable through a patients respiration patterns. While an abnormality in breathing rate is a good indication of respiratory diseases such as interstitial lung disease (too fast) or drug overdose (too slow), *fine-grained breathing volume information* adds valuable information about the physiology of the disease. Common obstructive airway diseases such as *asthma* and *chronic obstructive pulmonary disease* (COPD), for example, are characterized by the decreased flow rate measure at different breathing volumes. A constant loss of lung volume in these diseases not only indicates acute changes in the disease stability but also reveals lung remodeling and other irreversible states of diseases. Further, patients with lower airway diseases such as cystic fibrosis or tuberculosis could be diagnosed when sudden drops in breathing volume are frequently detected []. Therefore, accurate and fine-grained breathing volume measurements could offer rapid and effective diagnostic clues to the development of disease progression [86].

Being able to unobtrusively and continuously monitor lung volume has a high clinical impact. In many instances, patients with respiratory disease only show their symptoms for a short period and at a random time. In another important health care practice, breathing volume of prematurely-born, or preterm, babies needs to be closely and continuously monitored. A decrease of the babies'

breathing flow and volume must be promptly detected well before it causes oxygen desaturation for doctors to give an effective neonatal ventilation intervention. In a recent study on the effects of sleep apnea during pregnancy [87], it has been shown that detection of sleep-disordered breathing is possible in women who did not have sleep apnea prior to pregnancy, and that apnea leads to abnormal pregnancy outcomes [88]. In these cases, many only develop apnea for a short period of time. Hence, monitoring them non-invasively over a longer term to detect lung volume changes is critical. Last, but not least, long-term monitoring of breathing volume during sleep detects sleep-related breathing disorders common in 5% of children and 10-40% of adults population [89, 90]. Fine-grained and continuous breathing volume information will help classifying different types of hypopnea (partial airflow obstruction common in children) during sleep to better define the abnormality and direct proper treatment strategies where obstructive hypopnea is treated differently than central apnea [91]. In all above mentioned health care practices, the detection of disease and the observation of disease progression or remission could only be viable with an accurate and fine-grained breathing volume monitoring technique over an extended period of time.

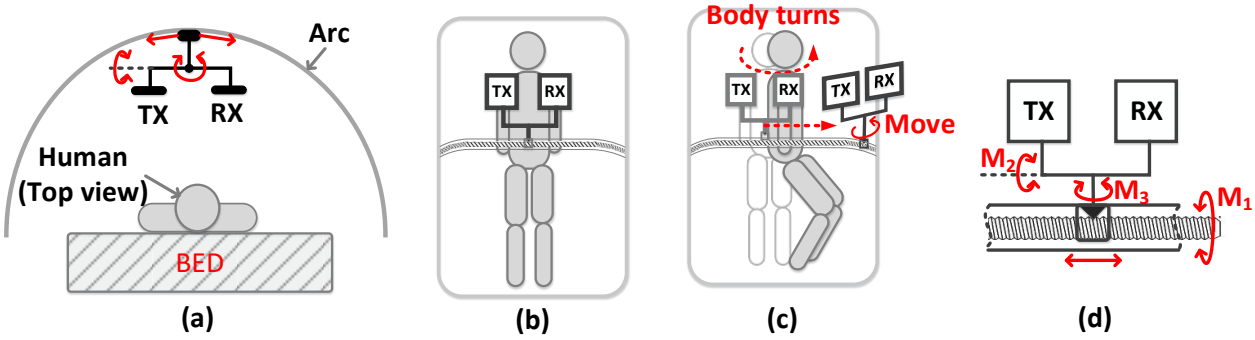


Figure 2.1: The conceptual design of WiSpiro. A radar beams to human's heart area to observe the respiratory and heart beat activities, as shown in (a, b). If a body movement or posture change is detected during sleep, the radar is then moved to a new location and redirects its radio beam to maintain its orientation pointing to the heart area, as shown in (c).The radar navigator could roll, pitch, and yaw with 360 degree of freedom using three motors $M_1$, $M_2$, and $M_3$ to control antennas' position and their beaming directions, as shown in (d).

Current practice for long-term breathing volume monitoring is obtrusive: airflow are measured from the nose and mouth qualitatively or at best semi-quantitatively with pressure manome-

ters or impedance chest belt [91]. Non-obtrusive approaches are apparently more attractive and usable. So far, however, the literature has mainly focused on the problem of **breathing rate** estimation using camera [92], laser [93, 94], infrared (IR) signal [95], earphones [96], and most recently using radio signals [5, 6, 97, 7, 98]. While these breathing rate estimation solutions are accurate and practical, little progress has been made along the line of breathing volume estimation. Massagram *et al.* [1] presented a technique to calculate breathing volume of a person from radio signal reflected off the subject's chest. While the technique is promising and works with a static subject, it is not applicable for long-term monitoring where subject movement is unavoidable. Moreover, it can only estimate breathing volume once in every breathing cycle. Shane *et al.* present a new technique to estimate breathing volume using camera [99], but this technique doesn't in case the user weary thick cloths or blanket.

This chapter introduces WiSpiro, a system that uses directional radios to continuously monitor a person's breathing volume with high resolution during sleep from afar. WiSpiro relies on a phase-motion demodulation algorithm that reconstructs minute chest and abdominal movements by analyzing the subtle phase changes that the movements caused to the continuous wave signal beamed out by WiSpiro's transmitter, as shown in Fig. 2.1(a, b). These movements are used to estimate breathing volume, whose relationship is obtained via a short neural-network training process. More importantly, the key feature of WiSpiro is the ability to work with the presence of human's random body movement. WiSpiro autonomously tracks the large-scale movements and posture changes of the person, and moves its transmitting antenna accordingly to a proper location in order to maintain its beam to specific areas on the frontal part of the person's body during sleep, as conceptually illustrated in Fig 2.1(c) and (d). WiSpiro also incorporates interpolation mechanisms to account for possible inaccuracy of our posture detection technique and the minor movement of the subject's body.

We have built WiSpiro prototype and demonstrated its potential through a user study that it can accurately and continuously monitor user's breathing volume with a median accuracy from 90% to 95.4% even in the presence of body movement and posture changes during sleep. Our results

also show granularity of the estimation is sufficiently high to be useful for sleep study analysis. They key findings and contributions of this work are as follows:

- *Theoretical and practical design of a breathing volume estimator.* We derive a model for the effects of chest movement and posture change on radar signals in terms of phase and signal strength. We adopt a calibration technique inspired by Bayesian's neural network back propagation training model to calculate breathing volume from the chest movements (Sec. 2.4).

- *A set of algorithms to address challenges caused by body and body part movement.* Posture detection and point localization techniques are developed to guide the antenna movement and orientation when movement occurs. To improve the correctness of inferring breathing volume from chest movement, an interpolation technique is introduced to integrate with the point localization output which helps correcting the estimation results (Sec. 2.6).

- *Implementation and evaluation show the feasibility, performance, and potential of the system.* We propose and implement 5 algorithms including chest movement reconstruction, posture estimation, point localization, and volume interpolation on our prototype. We conducted experiment on 6 users for 360 minutes and report the results. The results show high estimation accuracy after integrating of the 5 above-mentioned optimization techniques (Sec. 4.6).

## 2.2 Goals and Challenges

WiSpiro is designed to be able to *unobtrusively and autonomously* estimate the *breathing volume* with *fine-granularity at sub-breathing cycle level* even with the presence of random body movements. At a high level idea, the radar always directs its beam to human chest to observe the movements. When the user changes her posture during sleep, the radar then navigates to a new location and orientation orthogonal to the human chest. We now discuss challenges in realizing such goals including the ones caused by the nature of by body movement, breathing activities and

non-uniformed shape of human chest areas , and the nature of radio signals.

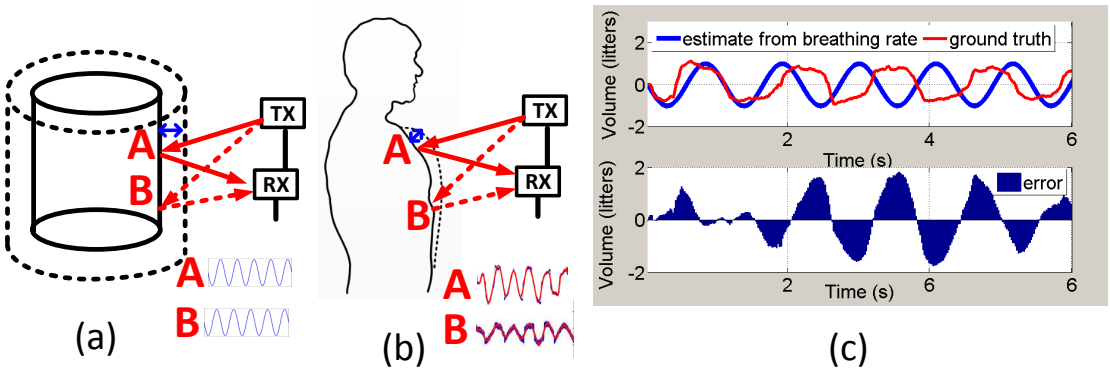


Figure 2.2: Motivation of developing WiSpiro. An illustration of the problem of approximating breathing volume using rate, and inferring breathing volume from untrained areas. Different with a cylinder as in Fig. (a), when observing the chest movement at two different areas (i.e., A and B) as in Fig. (b), the measured movements are different even though they are representing the same amount of air volume that the human breaths in and breaths out.

■ **Nonuniform movement of body areas during breathing.** Due to the non-uniform physical shape of human rib cage and upper body, the movement of different areas on human chest caused by respiratory activities are also non-uniform. Fig. 2.2 illustrates the non-uniformity of a human chest in contrast with a uniform surface of a cylinder. Given the same volume change, all points on the cylinder will move with the same distance. On the other hand, when a normal person inhales or exhales a certain volume, the xiphoid process area moves with a smaller amplitude compared to the movement of the right chest or left chest area, as shown in prior work in human anatomy [100]. This implies that the relationship between chest movement and breathing volume is non-uniform across different chest areas. Because of this property, even a minor non-respiratory movement of the body could make the antennas point to a new location which could cause significant volume estimation error. Therefore, at any given time, WiSpiro must be able to distinguish the area that it is beaming to in order to estimate breathing volume with high accuracy. To that end, we choose to adopt highly directional radar transceivers, and develop a posture detection algorithm to detect the cross section vector of human chest movement. Next, we build an autonomous motion control system which is able to direct the antennas towards a fixed anchor area (*e.g.*, heart area) to monitor

human chest movement. We present the solutions in Sec. 2.6.1.

■ **Non-linear relationship between chest movement and breathing volume.** It is seemingly possible to obtain breathing volume from the rate by assuming that the breathing volume has a form of $V = Asin\omega t$, where $V$ is the breathing volume, $A$ is the amplitude that could be obtained by calibration, and $\omega = 2\pi f$ ($f$ is the breathing rate) [6]. However, this model misses the inhaled and exhaled patterns of breathing activities. A brief experiment has been conducted to evaluate the possibility of this approach. The results (Fig. 2.2 (a)) show that the actual breathing volume does not follow a perfect sinusoidal form in each cycle. However, the imperfect curve is of interest to medical practitioners because it reflects the subject's breathing patterns. The respiration volume information is buried in the very minor phase shift of the reflected signal. This is in sharp contrast with respiration rate which only needs to extrapolate peak frequency of the respiration curve. To solve this problem, we establish a model to map WiSpiro's received signal pattern to chest movement (Sec. 2.4), and then map the movement to fine-grained breathing volume value according to a neural network model trained for different chest positions (Sec. 2.4.4).

■ **Possible blockage of radio signals.** During sleep, a subject might change her posture or move her body part (arms, legs, ..) to react to common environmental events such as random loud sound, change of temperature, humidity, and light condition, etc. These changes or body part's movements (*e.g.*, arms) might block the anchor area (*e.g.*, heart area) from the light-of-sight of the antennas. Therefore, WiSpiro needs to find an alternative area which can be seen clearly by radar. It then infers the breathing volume based on the movements captured on that area and the relationship between that movement and breathing volume learned in the one-time training process at the beginning. We present the solution to this problem in Sec. 2.6.2.

In summary, there are many challenges on designing a radar system for monitoring the breathing activity continuously, automatically, and with fine granularity. To our knowledge, WiSpiro represents the first system that can meet the challenges, and realize robust breathing volume estimation in practical sleeping environment with the presence of participant's random body movement.

## 2.3 System Overview

In this section, we discuss the overview picture of WiSpiro and briefly describe how does it overcome challenges mentioned earlier. WiSpiro is created to continuously monitor breathing volume of a subject during sleep. Figure 2.3 sketches its functional architecture, which includes three main components: *volume estimator*, *radar navigator*, and *one-time trainer*. In the following, we briefly describe these key components.

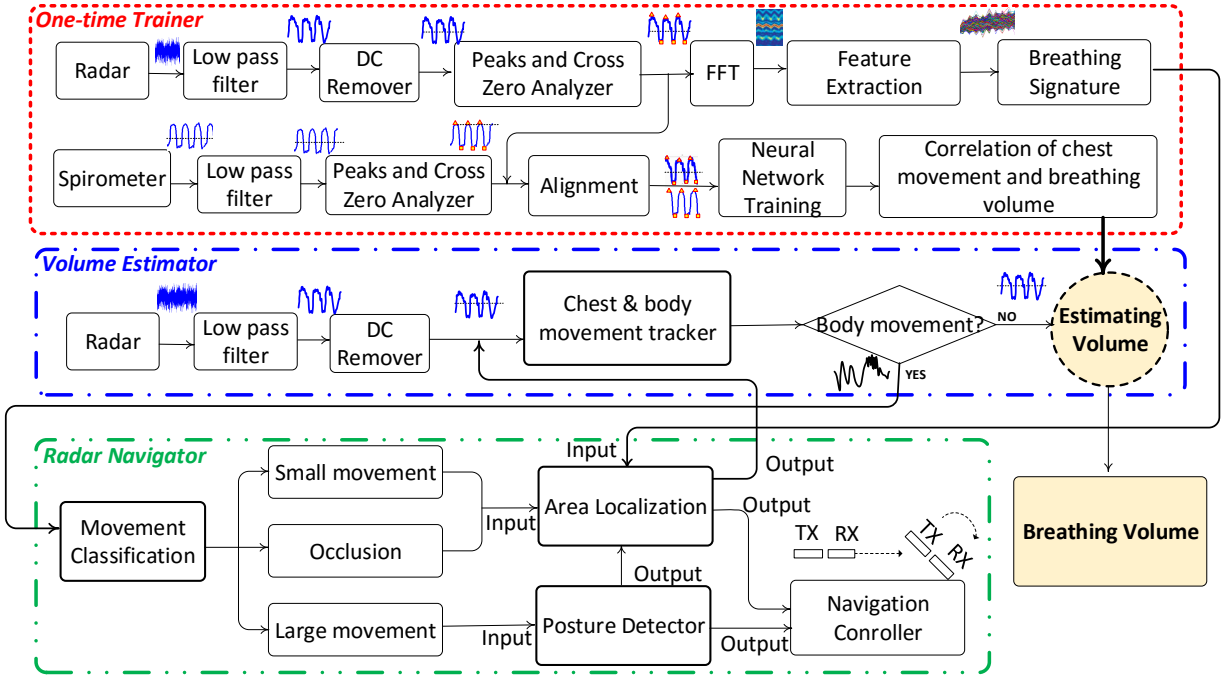


Figure 2.3: Architectural overview of WiSpiro. WiSpiro includes three main components (1) One-time trainer, (2) Volume estimator, and (3) radar navigator. One-time trainer provides a correlation between chest movement and breathing volume and the breathing patterns at each location on human chest. Volume estimator converts the chest measurements by WiSpiro to breathing volume using the correlation function obtained from one-time trainer when there is no body movement detected. When there is movement detected, Radar navigator component will control the 360 degree motor to navigate radar to proper location and direction keep track of human chest.

■ **Volume estimator.** WiSpiro builds on a decoding technique that extracts subject's frontal movement due to breathing, heart beat, and random body movement from the reflected radio signals. It continuously tracks the minute frontal body movement by analyzing the phase shift

and signal strength of the signal captured by the receiving radar. This movement information is then combined with a prior knowledge, learned through a one-time training process, to estimate fine-grained breathing volume.

■ **Radar navigator.** WiSpiro relies on this navigator to address challenges caused by subject's random movement, which could come from limbs, shoulder, other body parts, or the whole body, during sleep. Taking phase-shift and signal strength information from the previous component as inputs, the radar navigator detects large- and small-scale body movement. It **estimates the sleeping posture** of the subject and moves the antenna accordingly to redirect the radio beam to the subject's chest upon detecting body movement. Furthermore, it executes an **area localization** algorithm to identify the area on the chest to which the radio beam is pointing. This area information not only allows the navigator to fine-tune its antenna orientation to beam to the subject's heart area but also informs the volume estimator which training data should be used for calculating the volume. Note that the same breathing behavior can cause different areas to move differently. The last operation of the radar navigator is occlusion detection, *i.e.*, detecting if the heart area is in direct light-of-sight with the transmitter and the receiver. In case when occlusion occurs, it redirects the antenna beam to alternative areas (*e.g.*, lower chest, or abdominal areas) to continue the monitoring process.

■ **One-time trainer.** Firstly, a training step is required to establish the correlation between human chest movement and breathing volume because this correlation depends on chest size, age, breathing patterns, and so on. Secondly, the system needs to know exactly where it's pointing, so that it uses the correct correlation function for estimating breathing volume from the chest movement. For the first task, the trainer uses neural network to establish the relationship between body movement and beaming area with the breathing volume. Given an instance of chest movement at a known area on human chest as an input, the output of the function is a corresponding breathing volume. Lastly, the trainer provides the characteristics of the reflected signal when radar beams to different areas on the human chest. These characteristics are mapped into features. By comparing the features of the signal with those of the signals from trained areas, the system can infer the

location at which radar is pointing. We describe in detail the 3 above components in the next sections.

## 2.4 Volume Estimator with Chest Movement Reconstruction

### 2.4.1 Theoretical analysis of movement reconstruction

In this section, we describe how the reflected signal can be used to infer the chest movement. It is note that our WiSpiro includes a wireless transmitter sending out wireless beam at 2.4 GHz toward human chest and a wireless receiver to capture the reflected components of the signal. The WiSprio transmitter continuously emits a single tone signal with frequency $\omega$ using software define radio, and uses a directional antenna to beams the signal towards the subject's chest. When hitting the subject's chest, parts the signal will eventually be captured by a directional receiver radio. The single-tone continuous wave $T(t)$ is formulated as:

$$T(t) = cos(\omega t)$$

Let $d_0$ be the distance between radar and human chest, $m(t)$ be the chest movement function representing the chest position at time $t$, then $d(t) = d_0 + m(t)$ will be the effective distance between the radar and human chest at any given chest position at time $t$. The received signal, namely $R(t)$, can be written as:

$$R(t) = cos\left[\omega\left(t - \frac{2d(t)}{c}\right)\right] = cos\left[\omega\left(t - \frac{2d_0 + 2m(t - \frac{dt}{c})}{c}\right)\right]$$

In the above equation, $\frac{d(t)}{c}$ is negligible since $d(t)$ is 10 orders of magnitude smaller than the speed of light $c$. Therefore, $m(t - \frac{d(t)}{c}) \approx m(t)$ and, $R(t)$ can be rewritten as:

$$R(t) = cos\left[\omega\left(t - \frac{2d_0}{c} - \frac{2m(t)}{c}\right)\right] = cos\left(\omega t - \frac{4\pi d_0}{\lambda} - \frac{4\pi m(t)}{\lambda}\right) \tag{2.1}$$

As shown in the Eq. (2.1), the received signal $R(t)$ includes a high frequency component (*i.e.*, at transmitted frequency $\omega$) and a low frequency component caused by chest movement $m(t)$. We are interested in extrapolating the low frequency component which is pertinent to volume estimation.

To do that, we note that the radar mixes its received signal $R(t)$ with the originally transmitted one $T(t)$ using a simple mixer. In an ideal mixer, the output signal, called $B(t)$, is the multiplication of $T(t)$ with $R(t)$ which are the two inputs to the mixer. $T(t)$ is fetched into the mixer via its local oscillator (LO) port. Different frequency components of the output signal from the mixer is calculated as:

$$\begin{aligned} B(t) &= cos(\omega t) cos\left(\omega t - \frac{4\pi d_0}{\lambda} - \frac{4\pi m(t)}{\lambda}\right) \\ &= \underbrace{cos\left(\frac{4\pi d_0}{\lambda} + \frac{4\pi m(t)}{\lambda}\right)}_{\text{low freq. comp.}} + \underbrace{cos\left[\left(2\omega t - \frac{4\pi d_0}{\lambda} - \frac{4\pi m(t)}{\lambda}\right)\right]}_{\text{high freq. comp.}} \end{aligned} \tag{2.2}$$

Now that the two signal are separated after passing through the mixer, the low frequency component could be retrieved by a simple low pass filter. The filtered signal, called $F(t)$, is written as following:

$$F(t) = cos\left(\frac{\overbrace{4\pi d_0}^{\text{large-scale movement}}}{\lambda} + \frac{\overbrace{4\pi m(t)}^{\text{vital sign movement}}}{\lambda}\right) \tag{2.3}$$

Note that WiSprio estimates breathing volume only when the subject does not move. If a body movement is detected (discussed in Sec. 2.6), the radar navigator will take control to adjust the antennas to beam to a correct position before restarting the breathing volume estimation process. When the body is static, the distance between the antennas and the subject's frontal areas $d_0$ remains fixed. Therefore, from Eq. (2.3), phase change between two consecutive samples, $F(k)$ and $F(k-1)$, represents only chest movement due to vital signals including breathing and heart rate.

$$arctan\Big(F(k)\Big) - arctan\Big(F(k-1)\Big) \approx \frac{4\pi(m(k) - m(k-1))}{\lambda}$$

Let $\Delta m$ be the chest movement between the two consecutive samples, then $\Delta m = m(k) - m(k-1)$. If $F_I(t)$ and $F_Q(t)$ are the I and Q channels of $F(t)$, respectively, then the above equation can be rewritten as:

$$\begin{aligned} &\frac{4\pi\Delta m}{\lambda} \approx arctan\left(\frac{F_Q(k)}{F_I(k)}\right) - arctan\left(\frac{F_Q(k-1)}{F_I(k-1)}\right) \\ &\Leftrightarrow \Delta m \approx \frac{\lambda}{4\pi}\left(arctan\left(\frac{F_Q(k)}{F_I(k)}\right) - arctan\left(\frac{F_Q(k-1)}{F_I(k-1)}\right)\right) \end{aligned} \tag{2.4}$$

Eq. (2.4), shows how chest movement is calculated from samples of received signal. Note that the movement estimation is independent of $d_0$, which is base distance from chest to antenna.

### 2.4.2 Volume Estimation Algorithm

Based on the prior analysis, we design an algorithm to robustly demodulate fine-grained breathing volume from received signals. Several challenges need to be addressed in this process. First, the respiratory chest movement between two consecutive reflected signal samples is very small and is buried in minor phase change. Second, it is difficult to detect phase changes given the various types of noise in the system which are introduced by reflection from background objects, multipath components, and signal leakage due to TX, RX hardware imperfection. Last but not least, the nonuniform movement of different body areas during breathing makes the correlation between area movement vs. breathing volume to be dependent on the area location.

To overcome the above challenges, we exploit the regularity and quasi-periodic nature of chest area movement. In particular, an area is highly likely to move along the same direction, either inward (exhaling) or outward (inhaling), for a number of sampling cycles before the direction is changed. The intuition is that one cannot alter his or her breathing from inhale to exhale in one sampling cycle and then back. Moreover, the movement direction only changes when the subject changes from inhale to exhale, *i.e.*, finishing one half of a breathing cycle. Thus, we identify and group chest area movements within one half of a breathing cycle for breathing volume estimation for which per-sample breathing volume is inferred. In addition, we found that the noises are either reflected off rather stationary sources or from hardware leakage, and thus have either relatively low frequencies or frequencies following Gaussian distribution. Therefore, these noises can be removed with proper filtering mechanisms such as DC and band-pass filters. Lastly, a one-time neural-network-based training process is designed to mine the relationship between breathing volume and chest movement for each chest area. These area-specific relationships are later used for volume estimation. Alg. 1 summarizes our basic volume estimator which integrates these solution principles, with the following key steps.

**Algorithm 1:** Basic Volume Estimation Algorithm

**Input :** $F_I(k)$ and $F_Q(k)$ /* Received samples */
$S, areaID, L, N_c(areaID)$ /* which are number of samples, chest area ID, moving window size, and trained neural network for $areaID$, respectively/

**Output:** Estimated breathing volume vector $V^*[1:S]$

$F'_I \leftarrow$ DC filtered of $F_I$; and $F'_Q \leftarrow$ DC filtered of $F_Q$

$CZ[1:n] \leftarrow$ Find cross zero indexes of $arctan(\frac{F'_Q}{F'_I}[1:S])$,

**for** $j = 1$ **to** $n-1$ **do**

  $V[CZ(j):CZ(j+1)] \leftarrow N_c(areaID, arctan(\frac{F'_Q}{F'_I})[CZ(j):CZ(j+1)])$

$V^*[1:S] \leftarrow V[CZ(1):CZ(n)]$

*Signal preprocessing.* Assuming the signal sequence received by the receiver has $S$ samples which are in I and Q channels and acquired as described in Sec. 2.4.1. The series of $F_I(k)$ and $F_Q(k)$, $k \in [1:S]$ contains DC components caused by hardware leakage and quasi-stationary background which are removed by a moving-average DC filter. The filtered signal sequence, $F'_I(k)$ and $F'_Q(k)$, are $F'_{I,Q}(t) = F_{I,Q}(k) - \frac{1}{L}\sum_{i=0}^{L} |F_{I,Q}(k-i)|$ in which $L$ is the moving window size and $k \in [1:S]$.

*Half-cycle segmentation.* The filtered samples are then divided into $n$ segments where $n$ is the number of times that the phase of the signal, $arctan(\frac{F'_Q}{F'_I})$, crosses zero. By doing so, samples of the same breathing activity, either inhale or exhale, are grouped into the same segment. It also accommodates group with different size which mean breathing activity with different paces, such as a long inhale or short exhale.

*Per-segment volume estimation.* This step is to calculate the volume of each half-cycle segment. One important input of this step is the neural network that contains the relationship between a movement of a specific chest area and its corresponding breathing volume values. This network conducts the one-time training process that is presented in the following subsection, Sec. 2.4.3. Another key input is the ID of the chest location at which the antennas are beaming.

### 2.4.3 Training the Neural Network for Movement-to-Volume Mapping

WiSpiro is built on a physiological premise of the harmonic movement between the chest and lung expansion during breathing. That is, when the lung expanses due to inhaling, the chest is

also expanding. Likewise, the chest is collapsing during exhale. This phenomenal is the leading principle for our training algorithm. This training process quantifies the relationship between chest movement and breathing volume of individual. It needs to also take into account the non-uniformity of the movement on different chest areas given the same breathing activity.

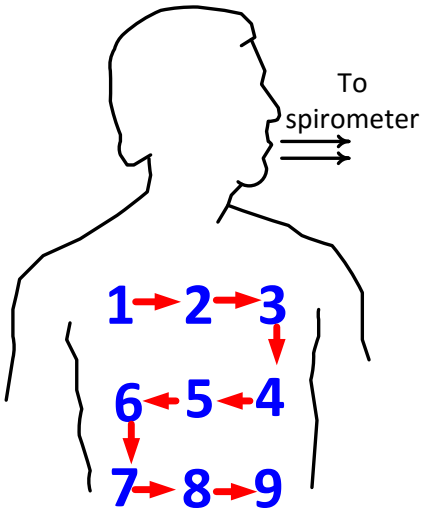


Figure 2.4: Movement-to-Volume Training. The subject chest is divided into subareas each. WiSpiro collects data from Radar and Spirometer data at the same time to build the correlation between chest movement and breathing volume. The blue text shows the ID of each location on human chest. The red arrows illustrate the direction of moving transceiver antenna during training.

The movement-to-volume training is needed only once for each subject. During this process, a subject is asked to lie down and breath normally into a spirometer. The breathing volume $V_G$ of the person is recorded. The patient's chest is spatially divided into subareas. Depending on the chest size and the beam width of the transmitting antenna, the number of areas, $gridSize$, is determined so that the antenna can beam to each area individually without overlapping to the others. Illustrated in Fig. 2.4, a chest is divided into 9 areas each of which is scanned sequentially by the antennas. For each area, $F_I$ and $F_Q$ signals are collected, along with the corresponding $V_G$. The training process is formalized in Alg. 2.

■ **Pre-processing.** The preprocessing steps remove DC components and filter out the signals that are not at frequencies of interest. This step is very important to remove the effect when radar

**Algorithm 2:** Training for Movement-to-Volume Neural Network

**Input :** $F_I(k)$ and $F_Q(k)$ /* Received samples */
$gridSize$ /* Number of chest areas */
$N$ /* Total number of samples collected per area */

**Output:** Trained neural network $N_c[i]$ for all areas with $i \in [1, gridSize]$

**for each area do**
  $V_G[1:N] \leftarrow$ Volume measured by spirometer for area $i$
  $f_L \leftarrow 0.2Hz$; $f_H \leftarrow 1.8Hz$; /* Cut-off frequencies */ $F'_I \leftarrow$ DC filtered of $F_I$; and $F'_Q \leftarrow$ DC filtered of $F_Q$
  $F^*[1:N] \leftarrow$ Band pass filter of $(arctan(\frac{F'_Q}{F'_I})[1:N])$
  Align $F^*$ with $V_G$ using peaks and cross zero points
  Resampling $F^*$ to match with $V_G$
  $[CZ_{F^*}[1:n']] \leftarrow$ Find cross zero indexes $F^*$
  Segment $< F^*, V_G >$ pairs using cross zero indexes
  Obtain $N_c(areaID)$ /* trained network for all pairs using Bayesian back-propagation neural network */
  Navigate the antennas to the next area
**return** $N_c$

is placed at different distance with the chest. It is note that the distance highly affects to the received signal strength. By doing DC removal, we could eliminate the effects of distance to the phase variation according to chest movement.

■ **Signal Alignment and Resampling.** Next, breathing volume vector $V_G$ and phase vectors $F_I$, $F_Q$ are aligned using zero crossing and peaks analysis. By doing so, the three time series have the same starting and ending points in time. The starting point of the three series is aligned based on the first peak location. The ending points correspond to the smallest last cross-zero indexes of the three series. To guarantee the same number of samples on all series, we resample the longer data series to match the size of the shorter one.

■ **Segmentation.** We divide the resulting series into multiple segments which are separated by cross-zero indexes. Each segment corresponds to an entire duration of either inhale or exhale, $CZ[i]$ with $i \in [1:n']$ and $n'$ is the number of segments. These 3-tuple segments are derived from $V_G$, $F_I$, and $F_Q$ and then fed into a neural-network that learns and quantifies the relationship between the movement and volume for each chest area. The inner-working of the neural-network is discussed below.

■ **Neural-network Construction.** We apply Bayesian back-propagation learning algorithm [101] to obtain the correlation of each chest movement cycle with its correspond breathing volume, $V_G$. The chest movement for each area is passed through the system in the first layer of the neural network. Hidden layers are expected to generate non-linear correlation function so that the breathing volume produced from the last layer is as close to the ground truth volume, $V_G$, as possible. To reduce the error between the output volume and the ground truth, the weight of each layer must be determined. In particular, the basic concept of back-propagation can be found from many well-known literature [102, 103]. We first discuss about back-propagation neural network, it has been commonly used recently due to its simplicity of implementation. Back-propagation is trained by feeding a series of examples of input and expected output. Each hidden and output unit processes its inputs by multiplying that input with its weight. The summation of the product is then analyzed using a non-linear transfer function to produce the result. The key idea of the training process is to modify the weights to reduce the errors between the actual output values and the target output values. The key limitation of this technique is that the optimal network architecture and learning parameters are usually determined by trial-error or by heuristics. A common problem of using neural network is overfitting, where the training algorithm takes the noise as a part of the data. To solve this problem, early stopping heuristics algorithm was proposed to solve the problem. To overcome most of above limitations, Bayesian probability model was used for back-propagation neural networks [101, 104].

### 2.4.4 Achievable Accuracy of Volume Estimator

We have implemented the basic volume estimating system (details in Sec. 4.5). Now we set up a simple scenario to verify the achievable accuracy of the technique and to identify possible optimization. The subject under test lies down on a bed and breaths normally for a period of 3 minutes, while his breathing volume are being monitored and estimated by both our WiSpiro and a spirometer [105]. At the beginning of the experiment, the person performs a 9-minutes-long training, following the procedure in Sec. 2.4.3.

Figure 2.5 plots the estimated volume time series. WiSpiro demonstrates a small mean error of $0.021l$, maximum error $0.052l$, and standard deviation $0.011l$ across the testing period.

We also found that the breathing volume waveform also represent unique patterns of a participant. which can contribute to clinical analysis of diagnosis and treatment. The signals (of different participants) are not only different in frequency and amplitude but also represent unique breathing form characteristics. This information is not be obtained by existing state of the art rate estimation techniques.

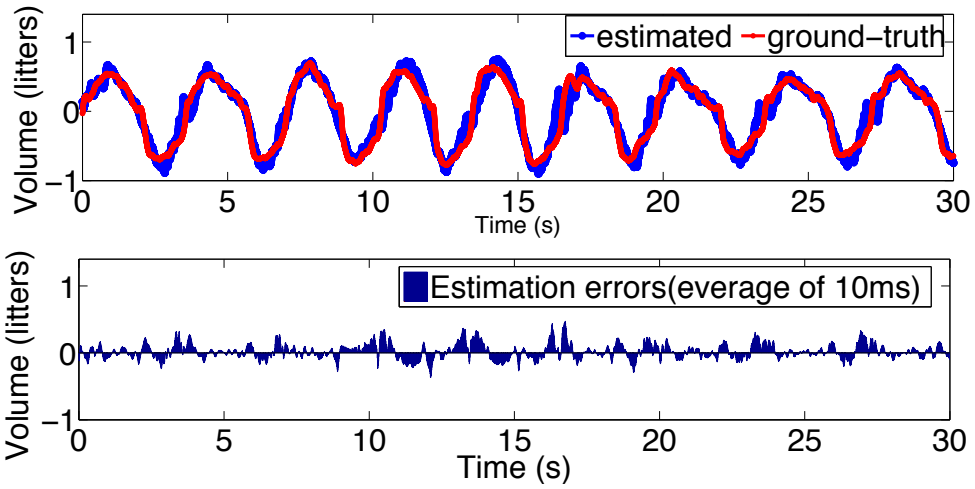


Figure 2.5: WiSpiro estimation output. The figure shows breathing volume estimated by the basic WiSpiro algorithm for a stationary person - a mean error of $0.021l$ and maximum error of $0.052l$ and a standard deviation of $0.011l$.

## 2.5 Body Movement Detection

### 2.5.1 Theoretical analysis of received signal strength and chest movement.

Given the transmitted signal as $T(t) = cos\omega(t)$ as mentioned earlier, the received signal strength, denoted as $P_r(t)$, reflecting from human chest can be modulated as:

$$P_r(t) = \theta K^2(d_0 + \hat{m(t)}), \tag{2.5}$$

where $m(t)$ is the chest movement, $\hat{m(t)} = m(t)\cos\delta$, $\delta$ is the angle between the chest movement direction and reflected direction. $d_0$ is the distance between antenna and human chest. $K(.)$ is

the gain, this is considered as 1/path loss. As the signal travels from the wireless device to the human chest and reflected off, the gain is in square form. Note that the antennas and human chest are under light-of-sight condition. So, $K(.)$ will follow traditional pass loss model such as free space. The signal scattered from the bed and other objects inside the environment is negligible. In addition, $\theta$ is the reflection capacity of the human chest.

From Eq. 2.5, $P_r(t)$ is proportional to the distance between the human chest and the receiver. The function $K(.)$ can be assumed to follow traditional path loss model (free space or log normal). Because the path loss is continuous, we use Taylor theorem to derive the received signal at the receiver [106] as following:

$$P_r(t) = \theta[K^2(d_0) + 2K'(d_0)\hat{m(t)} + ... + O(d_o)\hat{m(t)}^k], \tag{2.6}$$

where $K'$ is the first order derivative, $O(d_0)$ is Peano form of the remainder. The first value $K^2(d_0)$ is the DC offset, which depends on the distance between the radar and the human chest as well as the environment settings. The $K'(d_0)\hat{m(t)}$ contains the chest movement $m(t)$. Hence, by analyzing the received signal strength, we will obtain the movement information of the chest. In addition, by observing the change on the received signal strength change, we can infer the change between radar and human surface in order to estimate the human posture. As the received signal strength is affected much by the distance between the human chest and the radar, the chest movement $m(t)$ and DC offset $K^2(d_0)\hat{m(t)}$ are used mostly for posture estimation and area localization.

### 2.5.2 Posture change detection

To identify the new posture, the system must be detected when body movement happens first. A straightforward approach for posture change detection is to identify the threshold of the movement in terms of amplitude and variations. This technique, however, has some limitations as following: (1) The breathing behavior might be recognized as human movements when the human chest is very close to the antenna; (2) some body-part movements such as arm, would also be noticed as human movement; and (3) it is difficult to capture the duration of the posture change,

which might be important for sleep analysis.

The second possible approach for event detction is to use probabilistic model Markov-based [107]. This technique would provide a better event detection results, but it is too complicated and time consuming for real-time applications. In addition, as we sampling with a very high rate to keep the performance of our algorithm, lightweight event detection algorithm need to be implemented to maintain the responsiveness of the system. We will discuss more details regarding the computation time in Section 4.6.

Understanding those drawbacks, we apply lattice filter [108] to detect posture change event. This approach is efficient and easy to implement, which is very suitable for our real time application. In order to capture the posture change event, we calculate the Euclidean distance $d_{RSS}(n)$ in the k-parameter space of the RSS $d^2_{RSS}(n) = \sum_{i=0}^{p} \Delta k_i^2(n)$, where $k_{0:p}$ are a coefficient variables that are designed by minimization of the sum of forward and backward prediction error squared. With this implementation, the posture change is detected in order of seconds and very robust with different posture and distance from human body to the radar.

### 2.5.3 Body movement classification

After the body movement is detected, the system collects the change of wireless signal and then used it to infer the body movement type. There are three types of the movement: (a) changing posture, (b) body part movement, and (c) occlusion. We set two threshold of Eulidean distance for identifying movement type w/ and w/o changing posture. If the movement w/o changing posture, we then apply a fast algorithm to find the breathing frequency [109], which relying on analyzing DFT calculation of the input signal. More importantly, this solution is simple but yet effective. We obtained very high accuracy of posture classification. It is straightforward to classify posture change and body movement. The occlusion is obtained by analyzing frequency of the reflected signal. We refer more detail discussion in Sec. 2.6.2 and 2.6.3.

## 2.6 Radar Navigator

The above analysis and experiment have shown that the basic WiSpiro is capable of estimating fine-grain breathing volume of a static subject. In this section, we describe a set of algorithms to make WiSpiro robust to disturbance caused by body movement in practical scenarios.

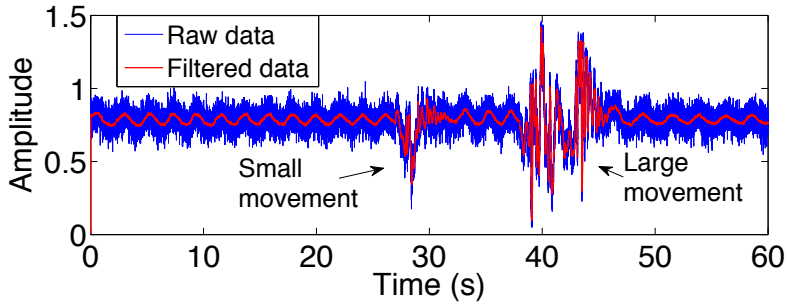


Figure 2.6: Movement event detection. Limb or body motion affects respiratory signal monitoring, causing small or large signal fluctuation. The disturbance magnitude could be used for classifying different types of movement.

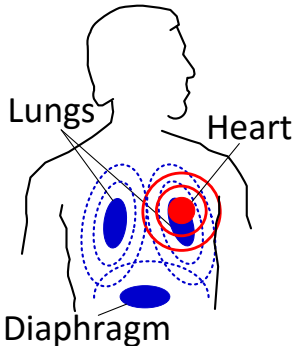


Figure 2.7: Vibration sources including lung, heart, and diaphragm forced movement.

### 2.6.1 Posture Estimation

WiSpiro's posture estimation algorithm *estimates the current posture* of the user and changes the *location* and *beam direction* of the radar to ensure the chest movements are always captured by the radar receiver.

The respiration and heartbeat information are detectable when the radar beams to user's front chest. Meanwhile, those vital signs are difficult to capture when the radar beams to user's back. Exploiting those facts, we develop a scanning algorithm which mechanically brings the radar across the bed surface to scan and search for a position that senses vital signs. During the scanning, the radar transceivers are continuously running and pointing orthogonal to the bed. Figure 2.8 shows the human posture, location of the radar and the corresponding power distribution of the measured vital signal. The posture detection algorithm relies on two main features: (1) the vital signal (heartbeat and respiration) reflected strongest when the radar is orthogonal to the human

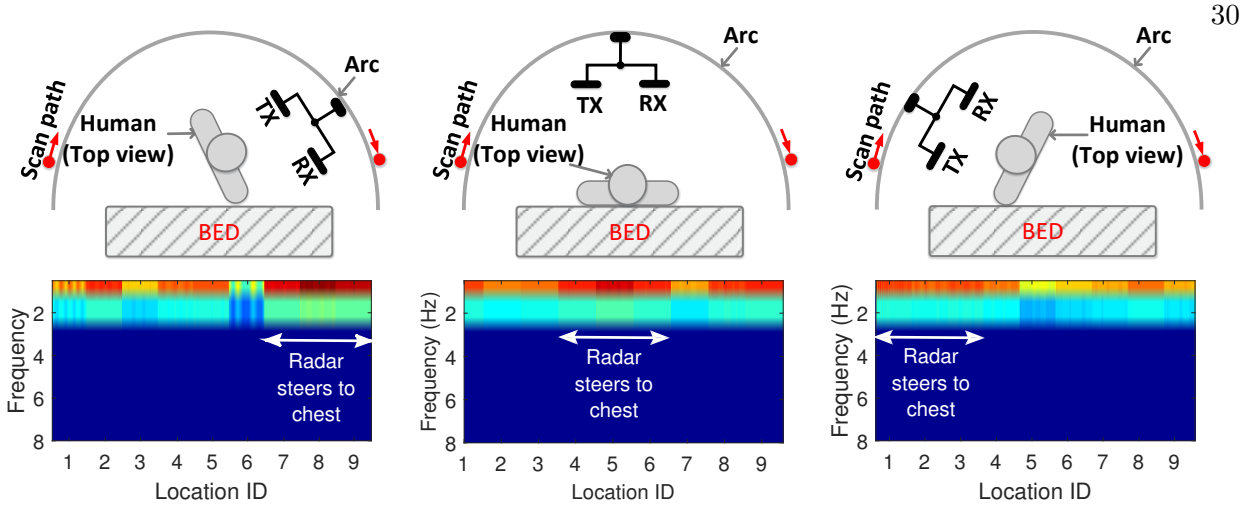


Figure 2.8: Example sleeping postures. Examples illustrating different postures of participant during sleep, location of radar together with obtained spectrogram at vital sign frequency band: (a) Human face to the right, (b) Human face up to the ceiling, and (c) Human face to the left. The direction respects to top-view perspective of human head.

chest as $\theta$ in Eq. 2.5. (2) The reflected signal from human body at vital sign frequency band is caused from LOS position. Understanding these fact, by applying Kadane's algorithm on the collected RSS, we could identify a subset of signal that content a maximum vital-sign reflected component. This algorithm bring down the resolution of detecting the angle between human back and the bed surface down to $5^o$. Details implementation is shown in Algorithm 3.

**Algorithm 3:** Posture Estimation

**input :** $f_s$ /* sampling rate */
$d_{scan}$ /* scanning distance */
$F_I(k)$ and $F_Q(k)$ /* received wireless samples */

**output:** moving radar to new location

$f_L \leftarrow \sqrt{F_Q^2(k) + F_I^2(k)}$

$f_L \leftarrow 0.2Hz$; $f_H \leftarrow 1.8Hz$; /* Cut-off frequencies */

$E[1:n] \leftarrow$ Energy($f_L$) in each of $5*fs$ samples;/* 5 seconds */

$\overline{E}[k]_{k\in[1:n]} \leftarrow$ Kadane Algorithm($E[1:n]$)

Mapping $k$ to location of antenna on the arc

Move radar to new location

Next, WiSpiro navigates the radar to search for and beam to the heart location. Heart location is selected because the corresponding signal fluctuation contains both respiration and

heartbeat information. However, it is nontrivial to automatically direct the radar from current location to the heart location. The required moving distance differs for different postures. For example, moving the radar from location 5 to 3 (Fig. 2.4) requires the radar to move its beam by 5 cm when the user is lying flat on bed (orthogonal to radar beam), but it requires only 4 cm when user body forms a 40 degree angle with the bed. In response, WiSpiro estimates the angle between the user's back and the bed to calculate the effective movement its beam would make on the chest surface given a fixed amount of movement on the radar. WiSpiro then directs the radar to different areas while capturing the signal at each moving step and stops at the location. Last, it identifies the heard area by finding the location that has the received signal that best matched with that of the heart location (Sec. 2.6.2).

### 2.6.2 Point Localization

**Algorithm 4:** Point Localization

**input :** $F_I(k)$ and $F_Q(k)$ /* Received samples */
$TF(F1[1:16] \rightarrow F_n[1:16])$ /* features of all areas */

**output:** area's ID

$f_L \leftarrow 0.2Hz$; $f_H \leftarrow 1.8Hz$; /* Cut-off frequencies */

$F'_I \leftarrow$ DC filtered of $F_I$; and $F'_Q \leftarrow$ DC filtered of $F_Q$

$F^* \leftarrow$ Band pass filter of $(arctan(\frac{F'_Q}{F'_I})[1:N])$

$F[1:16] \leftarrow$ Feature extraction$(F^*)$

Normalize $F[1:16]$ respecting $TF(F1[1:16] \rightarrow F_n[1:16])$

area's ID $\leftarrow$ K-NN classify$(F[1:16], TF)$

This section describes how WiSpiro recognizes the exact chest location the radar is beaming at. As can be seen in Figure 2.7, human chest movement comprises 3 main sources: lungs, diaphragm, and heartbeat. Different areas move differently according to the distance to vibration sources, and the structure of muscles. We divide the chest into nine areas as in Figure 2.4, named as $P1, P2, ..., P9$, respectively. This division depends on the radar beamwidth, its distance to chest, and the chest size. With a narrower beamwidth, the number of areas can be increased. On the other hand, the number of areas will be decreased if the system monitors young subjects with small

chest (*e.g.* a baby). The key idea is to make sure the beam width is small enough to isolate the signal reflected from different areas. Moreover, as only a discrete set of areas have been trained, we use *spline interpolation* technique to fill up the data for untrained areas.

■ **Training for Point Localization.** According to the characteristic of movements on different areas as mentioned above, we selected the following signal features to distinguish them:

- *Mean of interested frequency ranges.* We extract the center gravity of the power spectrum on respiration and heartbeat ranges. The interested frequency ranges are obtained from bandpass filters with $f_{L1} = 0.2$Hz, $f_{H1} = 0.5$ Hz (dedicated for obtaining breathing frequency range), and $f_{L2} = 1$Hz, $f_{H2} = 1.8$Hz (dedicated for heartbeat frequency range).

- *Mean of interested bandwidth.* We compute the spread of those frequency ranges around the mean frequencies. This information represents the distribution of dominant frequency components on each area. As an example, the closer to the heart, the smaller spread and higher peaks of the mean frequency on heartbeat range will show up.

- *Group delay.* We calculate the time-lapse between mean of central interested frequency ranges. This would help to distinguish the area according to their distance from the moving sources.

- *Total energy of interested frequency range.* This is the integration of the power on interested frequency. This feature reflects the distribution of the signals.

- *MFCC features*: With a windows size 10s, window shift 2s, pre-emphasis coefficient 0.97, the system extracts 12 mel freuquency cepstral coefficients (MFCC). We use the window of 10s to ensure a sufficient number of respiration cycles for frequency feature analysis.

Figure 2.9 shows the features of wireless signal monitored from those areas. As can be seen from the figure, the signature of each area is distinctive to each other.

■ **Point and Volume Interpolation.** As mentioned above, it is infeasible to conduct a training procedure over all areas on the human chest, and we use 9 discrete spots instead (Figure 2.7(a)). If

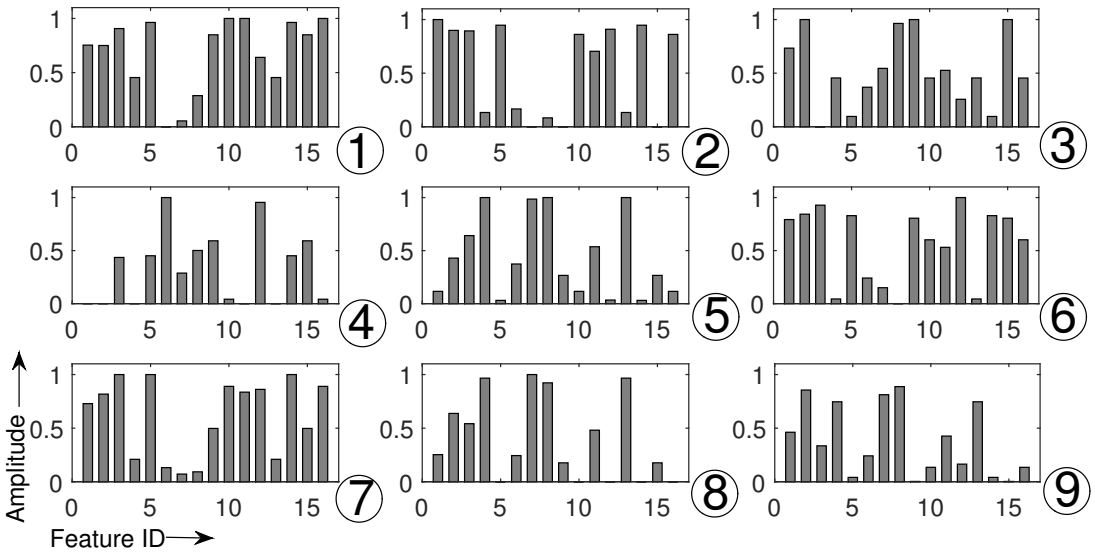


Figure 2.9: Features of 9 trained areas. WiSpiro recognizes the breathing of each chest location based on the characteristics of the obtained signal when the radar is steering to a certain chest area.

the radar beams areas in between the spots, the area estimation accuracy is decreased. To solve this problem, we used spline interpolation technique to fill up the missing knowledge. More specifically, spline interpolation is considered as polynomial interpolation because the interpolation error can be made small even when using low degree polynomials for the spline [110, 111].

### 2.6.3 Occlusion

After small human body movements, WiSpiro may detect a loss of heartbeat-frequency. The Figure 2.10 (a) and (b) show the availability of heartbeat frequency range before/after movement. When the heart-beat frequency is lost, WiSpiro reruns the scanning procedure until heartbeat signs are identified again. If the scanning fails, this is called *occlusion*. The radar now searches for two alternative areas: lower chest, and abdomen to find the alternative area. The first location that fits to one of the location in the trained database (for area recognition) would be used as an alternative area. Note that if a large movement is detected, the system will start posture detection algorithm.

In summary, taking the above mentioned issues into account, Alg. 5 summarizes how WiSpiro

integrates all presented components and algorithms.

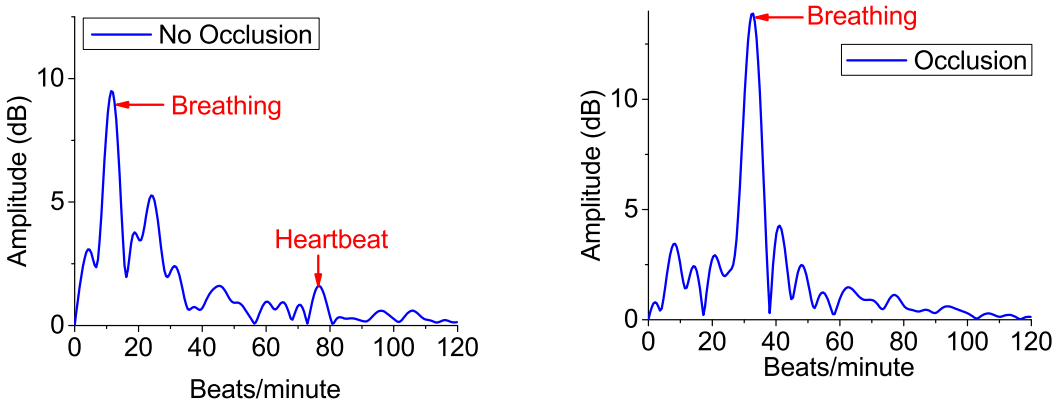


Figure 2.10: Samples of the FFT outputs of the received signals when radar beams to human heart location without and with occlusion scenario.

**Algorithm 5:** WiSpiro Breathing Volume Estimation

**input :** $data_{RD} \leftarrow$ data from radar
**output:** area's ID
$filter_{RD} \leftarrow$ Band pass filter ($data_{RD}$), $f_L$=0.2Hz, $f_H$=1.8Hz
Detecting human activities change based on $filter_{RD}$
**if no body movement is detected then**
    Run Basic Volume Estimation algorithm (Alg. 1)
**if large body movement is detected then**
    Run Posture Estimation algorithm (Alg. 3)
**if small body movement is detected then**
    Run Point Localization algorithm (Alg. 4)

## 2.7 System Implementation

In this section, we describe the WiSprio hardware and software that we implemented for evaluation purposes.

■ **Hardware.** As illustrated in Fig 2.11, the hardware setup is composed of two main components: a radio transceiver and a radar navigator. The *radio transceiver hardware* is developed from a WARP kit v3 board [112]. A transmitter sends single tone continuous wave at 2.4 GHz by the script written in Matlab. A receiver captures reflected AC-coupled signals, convert to base band,

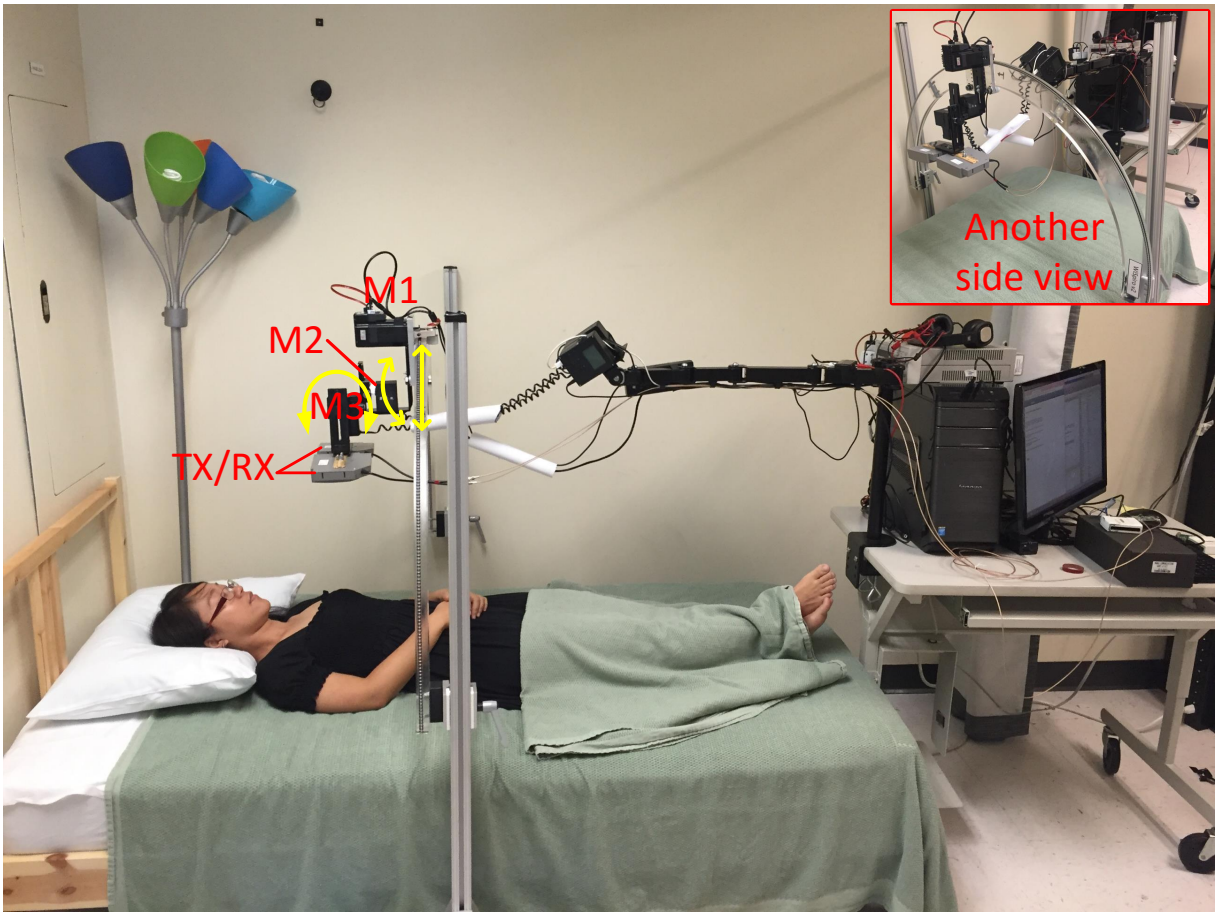


Figure 2.11: The current setup of WiSpiro. The motor M1, M2, M3 are controlled by computer. The TX/RX is controlled by a WARP board.

and output discrete I/Q samples with 100 kHz baseband sampling rate. The received I/Q signals are transferred to a PC through Ethernet cable, to which our algorithms in Sec. 2.4 and 2.6 are applied.

The radio antennas are mounted on a mechanical motion control system from Applied Motion [113] for sliding and Cinetics [114] which are steered by a PC host in real-time. The antennas are connected to WARP kit v3 board through SMA connection. The control system supports 360° pan, tilt, and the slide movement is controlled by an automated script. To navigate the radar to proper location and orientation, the motion control system is driven by our radar navigator algorithms (Sec. 2.6) which are implemented on the PC host. The whole system is mounted across

and on top of a twin-size bed on which all experiments are conducted.

Spirometer, camera, and microphone are used together to create ground-truth for various experimental verification, to be detailed in Sec. 4.6. Figure 2.11 shows WiSpiro's setup in lab environment.

■ **Software.** We implement a program in Matlab to perform the training algorithms and volume estimation algorithm described in Sec. 2.6. The radar controller software is developed and run in Matlab to realize posture estimation, point (area) localization and associated training algorithms (Sec. 2.6), and also make decisions on moving and steering antennas to proper location. We also developed a software using C++ to simultaneously trigger multiple hardware pieces at once to minimize the execution effort of the system and minimize the starting time discrepancy across the devices.

In addition, the original WARP board doesn't support real-time data forwarding with high traffice from the device to PC. We have adopted CWARP technique [115] to solve the problem. The key idea is to utilize parallelism to run the read/write operations concurrently. In addition, a high-bandwidth link is used at the host to support the combined transfer rates. We could obtain up to 3.6 GHz/s of sampling rate. However, to reduce the size of our data collection, we use the sampling rate at 100KHz.

## 2.8 Performance Evaluation

### 2.8.1 Experiment Setup

**Participants**: To evaluate the performance of WiSpiro, we recruited 6 students (5 grads, 1 middle-school), with different weight, height, and a mean age of 25. During the experiments, a subject sleeps on the WiSpiro testbed (described in Sec. 4.5) wearing their normal clothes and covered by a thin blanket in some cases.

**Ground truth**: We use a spirometer [105] as a ground-truth to evaluate WiSpiro's volume estimation accuracy and train its algorithms when necessary. A camera was used to record participants'

sleep behaviors and noise, together with a laser pointer to track the antenna's direction.

**Training**: The training process was done within 9 minutes for each participant. They were asked to breath normally to a spirometer when the radar was navigating and collecting data at all desired training areas.

**Testing**: After training, each participant was asked to sleep normally for about 60 minutes while WiSpiro is running. The spirometer was attached to the participant's mouth to collect ground-truth data.

### 2.8.2 Experiment Results and Analysis

■ **Overall accuracy of breathing volume estimation.** We group the testing results based on the ID of the area that the radar points to. Fig. 2.12 shows that, WiSpiro can estimate breathing volume with 90% to 95.4% accuracy, which mean the error is less than 10% of the total breathing volume within an average window of 10ms. The performance peaks at areas on upper part of the chest and around the heart area. The results also show that the impact of body and limb motion is small, thanks to the radar navigator algorithms.

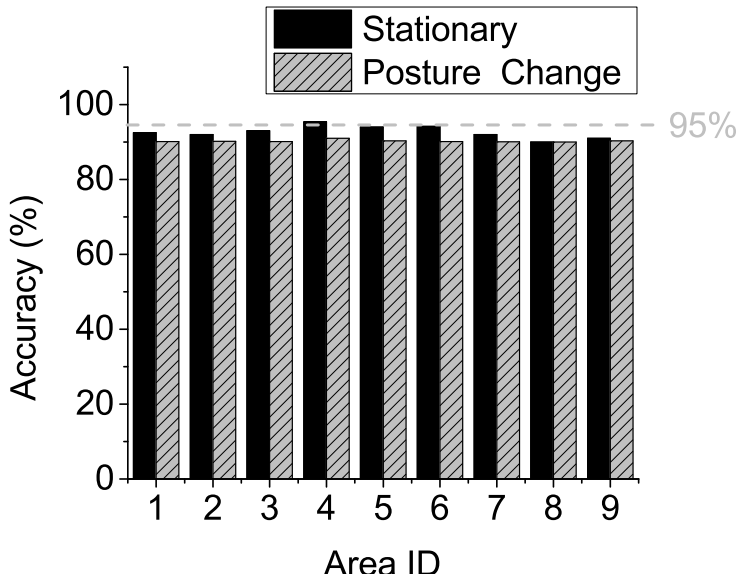


Figure 2.12: Breathing volume estimation accuracy. The mean accuracy of volume estimation in two cases: users sleep stationary on the back, and users move during sleep.

■ **Medical significance of WiSpiro.** We evaluate the medical implication and benefit from WiSpiro, focusing on a specific question: *Could WiSpiro provide meaningful information to help clinical doctor in sleep and respiratory disease diagnosis?*

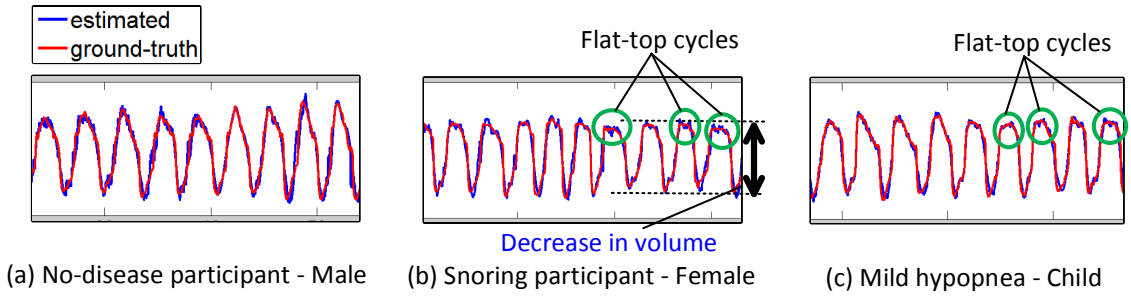


Figure 2.13: WiSpiro breathing volume signal. The example volume signal of the three participants with and without breathing and sleep diseases. Flat-top breathing cycles and the decrease in volume are features that are identified and used by clincal doctor for diagnosis.

We recruited 3 volunteers: one male middle-school intern student with known minor hypopnea, one normal male student, one female student with a known mild snoring pattern. The three subjects' breathing volume, which is monitored by both a spirometer and WiSpiro, are given to a clinical doctor, a sleep expert who directs and operates a clinical sleep analysis lab in a state hospital.

From the fine-grained breathing information, the doctor was able to map the breathing volume pattern to each person without prior knowledge about the mapping. Once the symptom is confirmed, the doctor was able to provide further analysis of breathing and sleeping issues from the volume information, part of which is presented in Fig. 2.13 (b). *"With a known snoring female, the signal shows a small inspiratory flow limitation but very little effect on her tidal volume. This is a marker of mild flow limitation that is commonly seen in premenopausal woman. It is likely a non-REM sleep because of the regular rate. The normal volume variability which can normally be seen through $CO_2$ and $O_2$ levels.",* said the doctor regarding the female subject with mild-snoring. The flat top of part of the volume measurement, marked in Fig. 2.13, is an indication of flow limitation which is, otherwise, not possible to be captured with breathing rate information.

Regarding to the middle school student's breathing volume time series, the doctor analyzed as follows: *"These three breathing cycles (the doctor was pointing to the part marked on Fig. 2.13 (c)) show a moderate inspiratory flow limitation that decreases the tidal volume of the breath. This could be clinically important because the child might get enough $O_2$ due to the air flow limitation and decreased volume. This could lead to alteration of blood gas such as $CO_2$ and $O_2$ levels. The moderate flow limitation during sleep is one form of hypopnea"*. Once again, this analysis mostly relies on the breathing volume and its variation overtime, which is not acquirable from respiration rate.

While this qualitative analysis is not statistically significant to make a conclusive answer for the aforementioned question, it shows that WiSpiro's accurate and fine-grained breathing volume information is potentially useful for medical practice.

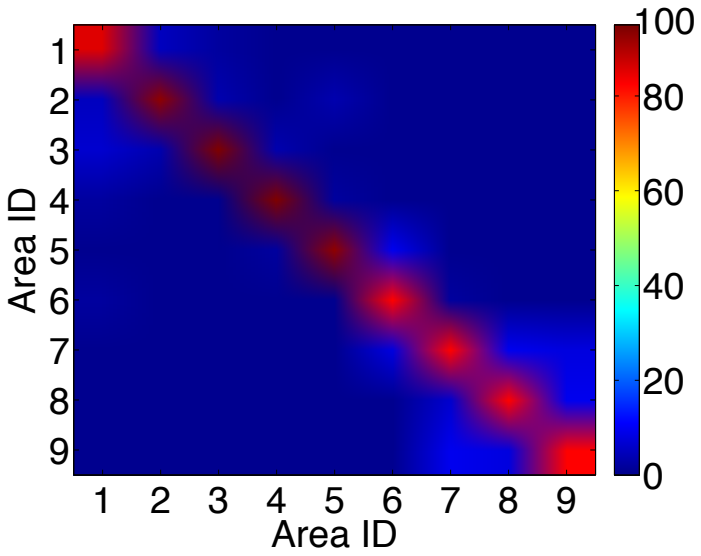


Figure 2.14: The accuracy distribution of point localization technique.

■ **Accuracy of point localization technique.** We now evaluate the accuracy of WiSpiro's point localization module and its impacts on the system's overall performance. After training, we beam the antennas to different areas on each participant. We repeat the process for 15 times at each area for all participants. The accuracy is then averaged across participants. Fig. 2.16 shows the

accuracy of the algorithm in correctly detecting the area ID. The results show that the algorithm performs better in detecting areas that are close to the heart, position 2, 3, 4, and 5, while accuracy drops near the abdominal area. This trend is intuitive since there are more vital signal affects on the former set of areas. Fig. 2.14 shows the error distribution of the localization. It shows that when an error happens, it tends to be confused with an area with its neighborhood.

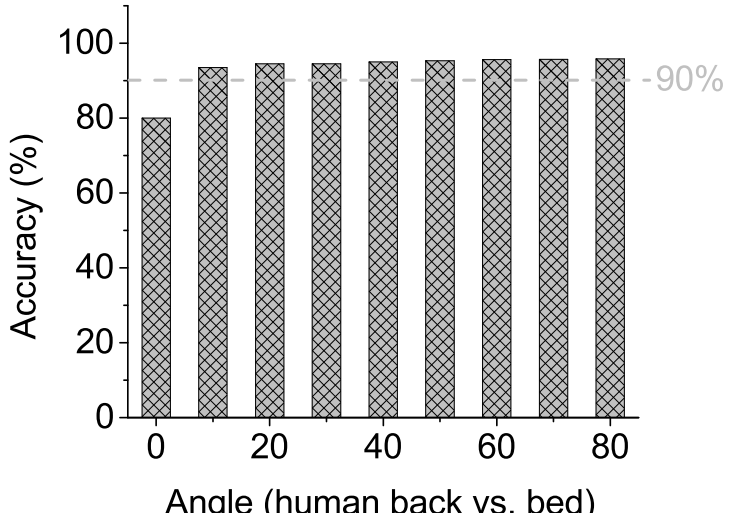


Figure 2.15: Sleeping posture estimation accuracy. Estimation accuracy of the angle between human back and the bed surface.

■ **Accuracy of posture detection.** The performance of our posture detection algorithm is presented in Fig. 2.15. A participant is asked to lie his/her body w.r.t. the bed with an angle ranging from $0^o$ to $90^o$ with step of $5^o$. The estimation is repeated 20 times at each angle. The angle is considered to be correctly estimated if the result is within 5% from the ground truth. With the new technique of posture detection, the performance of the system is significantly improved.

## 2.9 Conclusion

We have presented WiSpiro, the first autonomous radar system to monitor breathing volume of a sleeping person. WiSpiro achieves fine-grained volume estimation using a phase-motion model, combined with a neural network training that maps chest movement to breathing volume, taking

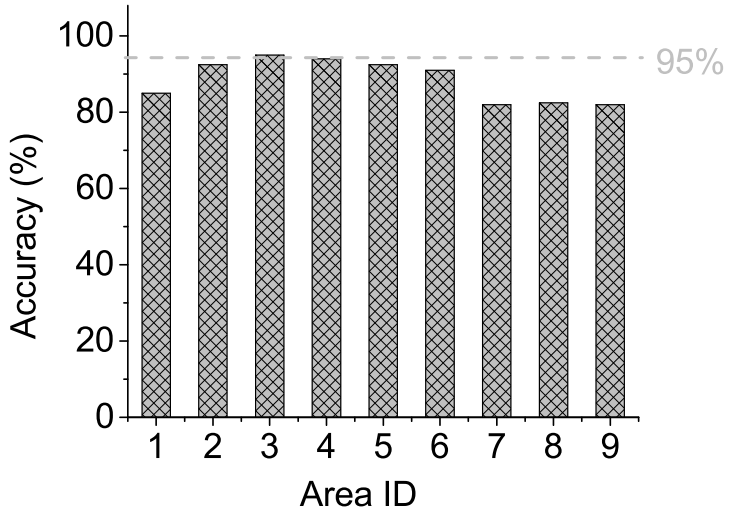


Figure 2.16: Chest area ID detection accuracy.

into account heterogeneity of frontal body areas. Further, WiSpiro handles random body movement, by redirecting the radar in real-time, using a set of navigation and area localization algorithms. Our prototype and experiments verify WiSpiro's feasibility, and its ability to track breathing volume at high accuracy. Our immediate next step of research is to optimize WiSpiro and test it in practical clinical environment.

## 2.10 Looking forward

WiSpiro relies on the correlation between breathing volume and chest movement of a human body. The system might not perform well in scenarios where that assumption does not hold. While it rarely happens, there exist a few of such cases. One example is apnea caused by blockage in the respiratory airway of the patient. Regardless of the apnea patient's effort in inhaling or exhaling, the breathing volume does not change since no air can go through the airway, while the chest and other frontal areas might still be moved by the pressure caused by the respiratory effort. One possible solution to detect this is to combine WiSpiro with a sensing system that could capture inhaling and exhaling air flow, such as $CO_2$, $O_2$ levels, or thermal camera.

WiSpiro's scanning process is currently taking several due to limitations of the mechanical motion control system and the minimum required period to obtain sufficient vital signal. The scanning will suffer further if the subject moves frequently during scanning, in which case, the scanning process need to be reset. This limitation can be overcome by using a more efficient motion control system, combined with electronically steerable phased-array antennas. However, the cost of the system would be added up.

Finally, our experimental results are performed on a small user population. More thorough testing with in-house and in-hospital setup could further validate the clinical significance of WiSpiro. We consider that as extension of this work. The improvement of WiSpiro hardware upgrading is small with current data set and number of participants. More importantly, as there are not many participants having critical issue with breathing behaviors, the sensitivity of the system has not been presented in the evaluation. We hope to deploy our system for clinical trial in the near future.

# Chapter 3

# Drone Presence Detection by Identifying Physical Signatures in the Drones RF Communication

## 3.1 Introduction

With the advent of inexpensive commercially available unmanned aerial vehicles (UAV), drones are rapidly rising in popularity as a host of a wide class of applications ranging from commercial delivery [116], environment monitoring [117], photography [118], policing [119], fire fighting [120], just to name a few. However, with the rise in drone usage, there has also been a rise in incidents involving drones, such as mid-air collisions, damage to property, and violations of privacy.

In particular, drones are increasingly flying in sensitive airspace where their presence may cause harm, such as near airports, forest fires, large crowded events, and even jails. For example, Dubai airport, the third busiest airport in the world, reported that in 2016 it had to shut down three times to avoid unauthorized drone activity [121]. In 2015, drones were used to smuggle drugs and contraband into a Maryland prison [122]. A quadcopter crashed on the White House lawn [123], raising concerns about the safety of buildings and political leaders. The presence of drones has interfered with and grounded aircraft fighting forest fires [124]. Drone crashes have also disrupted sporting events such as the US Open tennis tournament as well as a World Cup skiing race [125, 126]. In fact, based on FAA data, more than 300 drone incidents were reported in California alone between April 2014 and Jan 2016 [127], which is equivalent of 15 incidents per month on average or 1 incident every two days.

A variety of approaches have been explored to interdict drones. These include shooting nets at the drones to tamper with their propeller to bring them down [128], using lasers to shoot down drones [129], spoofing GPS to confuse a drone's localization system [130], hijacking the software of drones by hacking into them [131], using other drones to hunt down unauthorized drones [121], and even training eagles to attack and disable drones [132].

However, these interdiction strategies typically presume that the presence of the drone has already been detected. Recent work has sought to develop drone detection systems that leverage either microphone, camera, or radar to sense the presence of drones [9, 11, 16]. Each approach has its own limitations. Audio-based approaches can be confused by other sounds in noisy environments, has limited range, and cannot detect drones that employ noise canceling techniques [133]. Camera-based approaches require good lighting conditions, high quality lens, and camera with ultra-high resolution for detecting drones at long distance. Thermal and IR imaging cameras for long distance are prohibitively expensive and have limited coverage. Radio-frequency techniques based on active radar introduce RF interference. Geofencing is useful to prevent drones from flying into fixed areas known a priori as sensitive [127], but requires manufacturers to install such software and is less useful to prohibit drones from flying around temporary event venues.

In this chapter, we consider an approach to detect the presence drone by passively eavesdropping on the RF communication between a drone and its controller (Wi-Fi standard). Such communication mode often happens over standard unlicensed spectrum for which a low-cost COTS hardware can be utilized for observation. Prior work utilizing passive RF to identify drones has sought, for example, to detect the frequency of transmission, the MAC address of the drone, and the frequency of packet communication [13, 14, 15]. All these techniques suffer from various limitations, as described in the related work section, and none seek to discern whether physical signatures of the drone's motion are manifested in the drone's RF signal.

In this work, we investigate the fundamental aerodynamic and motion control mechanisms of drones to identify two key inherent types of movement of the drone's body, namely *body shifting* caused by the spinning propellers and *body vibration* due to navigation and environmental impact

corrections. We validate our hypothesis on the existence of such movements through empirical studies and then conduct a theoretical analysis on the characteristics of such movements. We also explore the feasibility of reconstructing such movement by using passive RF sensing. We then propose Matthan, a system that incorporates a number of algorithms to detect the presence of drone from both body vibration and shifting. It employs low cost software-defined radios (SDRs) to eavesdrop on Wi-Fi channels used in drone-to-controller communication. We demonstrate that this system can detect the physical signatures to uniquely identify an individual drone and effectively differentiate it from other mobile wireless devices at distances of hundreds of meters. Matthan is currently able to detect Wi-Fi embedded individual drones independently at any point in time. We are investigating detection of drones that communicate at other RF frequencies to identify multiple drones at the same time.

Our work makes the following contributions.

- We identify the relationship between the drone controller's compensation reaction and its body shifting
- We identify a second frequency component in the RF signal that we attribute to the drone's propellers
- We show that both of these on-board physical phenomena are manifested in the received RF signal
- We devise an algorithm to detect drones from their RF-based signature based on both body vibration and body shifting physical characteristics marked on the continuous data stream between drones and their controllers
- We verify that this algorithm can detect drone signatures at Wi-Fi frequencies that are uniquely differentiated from other mobile Wi-Fi devices, such as cars and walking cellphone users

- We confirm that this algorithm can operate at distances of hundreds of meters using a directional antenna with a 21 degree beamwidth
- We discover that this algorithm could be used to begin differentiating the seven different drones tested

In the following, we first describe in Section 3.2 the basics of drone flight and validate, using sensors attached to the drone, that the drone vibrates at the propeller frequency and that body shifting causes correlated disturbances in the RF signal. In Section 3.3, we develop a model to explain the influence of both types of body motion on the RF signal, and present our drone detection algorithm, which utilizes both frequency analysis to detect body vibration in the RF signal and wavelet analysis to detect shifts in the drone during flight. We provide a performance evaluation in Section 4.6 considering different types of evidence, then conduct an analysis over a variety of drones, environments, and distances. We conclude the chapter with a discussion of the current drawbacks of Matthan, related work, and a summary.

## 3.2 Fundamental Aerodynamics and Physical Signatures of Drones

Matthan relies on the unique physical signatures that persist across drones to detect and differentiate them from other moving objects. In this section, we start by providing the background on aerodynamic principles that allows drones to move towards a desired direction or remain balanced while flying. We then derive two unique physical signatures, namely *body shifting* and *body vibration*, that are present on all drones that have propellers. We empirically prove the existence of such signatures and then perform a formal analysis to show how such signature can be captured from the radio signals that are emitted from the drones for communicating with their remote controller.

### 3.2.1 Drone Movement and Control Background

Drones or micro air vehicles (MAVs) can be made from a form of helicopter, an airplane, a multirotors or even a balloon. In that, helicopter and multirotors are the most common drones due

to simplicity of manufactoring. As its name indicated, a multirotor [134] has multiple rotors with a much simpler flying control mechanism compared to that of a helicopter [135]. Instead of changing its wing's pitch and speed using a complex rotor as found in helicopters to maintain balance and maneuver, a multirotor operates by simply changing its motors' speed. Therefore, no complex mechanical parts is required. Partly due to this simplicity, multirotor-based drones are much more popular than their counterpart helicopters [136]. Since it has multiple similar rotors arranged symmetrically, a multirotor can keep its balance more easily even when it carries additional load (e.g. cameras, packages). The change in the center of mass can be tolerated by simply adjusting the rotors' speed. These advantages of multirotor become even more significant when it comes to small-sized drones since integrating sophisticated controlling mechanics as in a helicopter requires a large form factor, increasing cost and size of the drone's footprint. Therefore, most of today's commercial drones are of the multirotor type and the same trend is predicted for the near future [137]. As a result, we focus on this type of drone in this research.

■ **Drone equilibrium conditions.** The popular designs of multirotors include 4-, 6-,and 8-rotors which are naturally termed quadcopter, hexacopter and octocopter respectively. The most popular one is the quadrotor, which has four similar propellers arranged in either "$\times$" configuration or "+" configuration with equal distance from its the center of mass. The rotation direction of each propellers depends on its relative position. Let the indexes of the propellers be numbered sequentially from #1 to #4. If the propeller #1 rotates clockwise, for example, the ones #2 and #4 will rotate counter-clockwise while #3 will rotate clockwise as illustrated in Figure 3.1. To facilitate our analysis in the remaining sections of this paper, let $\omega_i$ with $i = 1..n$ be the rotation speed of each propeller. Without losing the generality, we only focus on analyzing quadrotors ($n = 4$).

Let $F_i$ with $i = 1..4$ be the forces generated by the propellers $i$ and $m$ be the mass of the quadrotors. Since the quadrotor is symmetric, if $L$ is the distance between the center of the quadrotor and each propeller, the moment generated by each propeller is calculated by $M_i = L * F_i$. In an ideal environment, in order to keep balance and remain in equilibrium state, the quadrotor

must obey these four physical conditions:

(1) $\sum_{i=1}^{4} F_i = -mg$ (Equilibrium of forces),

(2) $\sum_{i=1}^{4} F_i || g$ (Equilibrium of directions),

(3) $\sum_{i=1}^{4} M_i = 0$ (Equilibrium of moments), and

(4) $(\omega_1 + \omega_2) - (\omega_3 + \omega_4) = 0$ (Equilibrium of rotation speeds).

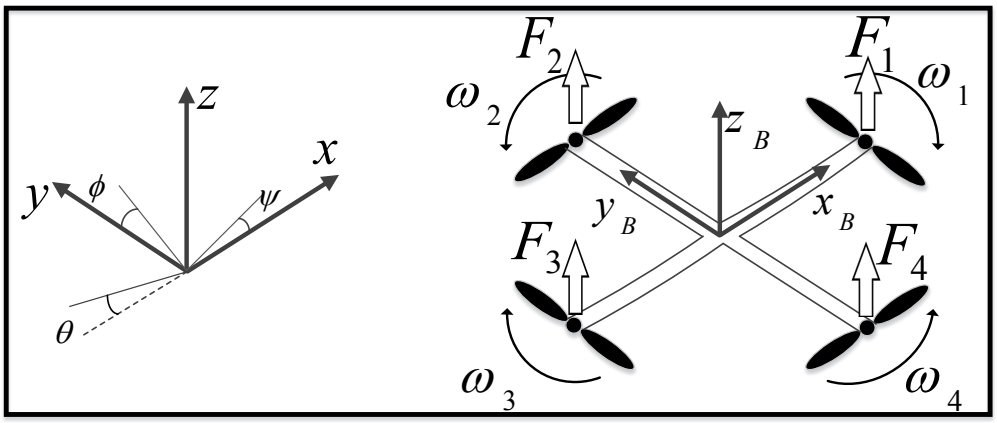


Figure 3.1: Earth and quadrotor reference systems. When a drone is moved from one place to another, different propellers will operate differently to move the make the drone move forward, backward, turn left, and turn right. However, when the drone is at equilibrium state, the physical conditions must be satisfied.

If one or more of those conditions are violated, the quadrotor will leave equilibrium state and start making movement as depicted in Figure 3.1. Two reference systems are used to represent the position and orientation of the quadrotor. The inertial reference system, i.e. the Earth frame (denoted $x$, $y$, $z$-axes) provides the absolute linear position of the quadrotor; and the quadrotor reference system, i.e. the Body frame (denoted $x_B$, $y_B$, $z_B$-axes) gives the angular position with three Euler angles. Roll angle ($\phi$), Pitch angle ($\theta$) and Yaw angle ($\psi$) determine the rotation of the quadrotor around the $x$, $y$, $z$-axes respectively.

■ **Drone maneuvering conditions.** Any movement of a quadrotor can be created by a combination of four basic movements: roll rotation, pitch rotation, yaw rotation and altitude change. Each of these movements is created by briefly violating the above equilibrium conditions by applying proper angular speeds to each propeller, $\omega_{1..4}$. For example, to create a roll rotation, $\omega_{1..4}$ must be

applied such that $(\omega_1 + \omega_4) - (\omega_2 + \omega_3) \neq 0$ . Similarly, to generate a pitch rotation, the drone needs to change the angular speeds of different rotors such that $(\omega_1 + \omega_2) - (\omega_3 + \omega_4) \neq 0$. To move the drone up and down, the rotation speeds should be changed to adjust the thrust force $F$ so that $\sum_{n=1}^{4} F_i \neq -mg$.

### 3.2.2 Body Shifting and Body Vibration as Drone's Physical Signatures

Many different controllers have been introduced in the literature following aforementioned principles, including PID [138, 139, 140, 141], back-stepping [142, 143], nonlinear H$\infty$ [144], LQR [141], and nonlinear controllers with nested saturation[145, 146], to stabilize and maneuver drones. Beside taking the desired direction as inputs, these controllers also need to take into account the impacts of the unpredictable environments, such as wind, and the inaccuracy of its sensors and actuators. Since these factors are nondeterministic and occur often, the controller needs to frequently react to and compensate for them, causing undesirable physical movement of the drone. In particular, the undesirable movements can be the result of the controller's reaction to (a) an environmental change, e.g., a gust of wind, a magnetic storm; (b) numerical errors inside control loop of the drone itself, e.g. the imperfection of converting from speed of rotation to the exact targeted pitch, roll, yaw angles [135, 147, 148]; and (c) by the vibration caused by propeller's movement [135]. We leverage these undesirable yet persistent movements as unique signatures of drones, which can be used to differentiate a drone from other moving objects. The movements of interest fall into two main categories: *the drone's body shifting* and *the drone's body vibration.*

■ **Drone body shifting.** Body shifting occurs as a sequence of discrete events. Figure 3.2 illustrates the drone's body movement caused by wind (a, b) as the result of a rebalancing effort from the drone's controlling mechanism (c, d). Beside the drifting its body does due to the effect of environmental conditions, the drone body also usually changes its body orientation and direction when it flies. The angular velocity of the rotor $i$, denoted $\omega_i$, creates force $F_i$ in the direction of the rotor's axis. The angular velocity and acceleration of the rotor also need to create torque $\tau_{M_i}$ around the rotor axis: $F_i = k\omega_i^2, \tau_{M_i} = b\omega_i^2 + I_M\omega_i^*$ in which $\omega_i$ is the rotation speed of rotor $i$, $k$

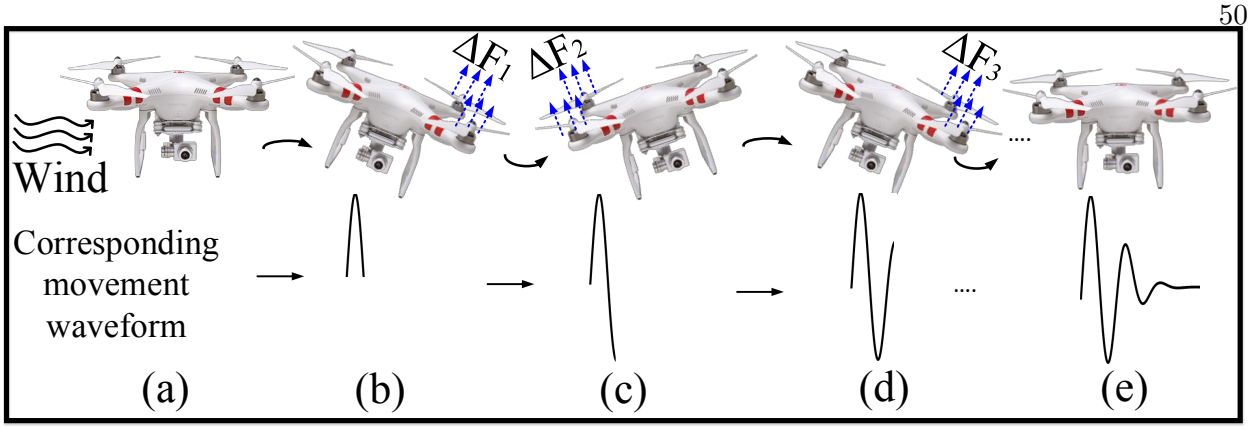


Figure 3.2: Drone body shifting. An example illustrated the drone shifts its body due to the effect from an unexpected wind. The additional force $\Delta F$ are created by speeding up corresponding propellers to balance the drone.

is the lift constant, $b$ is the drag constant, the inertial movement of the rotor is $I_M$. The impact from $\omega_i^*$ is usually small and thus it is omitted. When the wind creates an additional force that changes the balance of the drone, the drag force now becomes $\tau_{M_i} + \Delta F_1$. To make the drone return to a stable state, the propeller on the right side will speed up to create an additional force $\Delta F_2, (\Delta F_1 \approx \Delta F_2)$ against the force generated by the wind. When the drone is balanced, if the additional force $\Delta F_2$ stays longer than expected, it creates a side effect to the drone body that makes the drone unbalanced again. Next, the controlling algorithm will changes the propeller speed expecting the drone to go to the balanced state. This process will be repeated and take several iterations until the drone gets to its equilibrium. We consider this behavior to be one signature of a flying drone that can be used to distinguish it from other flying objects, e.g. birds. Because of the waveform's resemblance to a wavelet, this stimulated our interest in developing a wavelet-based detector for drone body shifting, as explained later.

■ **Drone body vibrations.** The drone body is vibrated within a certain frequency range and such vibrations are usually caused by the rotation of its propellers [135, 147]. In the literature, several works have been conducted to analyze the vibration of helicopters caused by their propeller's rotation [149, 150, 151]. The resulting vibration is the vector sum of vertical, longitudinal, and

lateral vibrations. More specifically, in forced vibration, the frequency of the vibration is close to the frequency of the force or motion applied, and the magnitude of the vibration depends on the actual mechanical system [152]. The steady-state solution of the forced vibration system with damping subjected to a sinusoidal force $F(t) = Fsin(2\pi ft)$ can be expressed as $x(t) = Xsin(2\pi ft+\phi)$, where $x(t)$ is the vibration function, $X$ is the amplitude of the vibration, $f$ is the vibration frequency, which is the same as the engine operating speed, and $\phi$ is the phase.

Thus far, we have discussed two types of drone's inherent body movements that happen when the drone is flying. However, these types of movement are unexplored in the literature. To validate our hypothesis, we conduct a set of experiment to validate the drone body shifting and body vibration signatures. We also conduct a feasibility check to confirm whether an RF-based technique can be used to detect the drone by observing its signatures.

### 3.2.3 Preliminary Validation of Drone Body Movements

This section presents a set of experiments to validate the signatures of the drone as mentioned earlier. We conduct two main experiments to explore the body movement characteristics of the drone using (1) inertial measurement units (IMUs) and (2) a wireless sensing hardware. In the first experiment, we attach external IMUs, to the drone's frame underneath each propeller to capture the drone's body movements. Secondly, we also attach firmly a 2.4 GHz wireless transmitting antenna to the drone. The RF signal from the transmitter is captured by a wireless receiver placed 2 meters apart. The goal here is to validate whether the drone body movements are observable by analyzing the received wireless samples. We present results here from experiments conducted for the Parrot Bebop [153] in an indoor environment. Similar confirmation was obtained using the DJI Phantom [154].

#### 3.2.3.1 Validating Drone Body Movements using IMUs

We inspected behaviors of the drone including taking off, hovering, and flying. The drone is augmented with 4 IMUs (MPU 9150 [155]) each of which is mounted beneath propeller. The data

from these IMUs are gathered by an Arduino Pro Mini board [156] and then are sent to a computer via Bluetooth Module HC-05 [157]. A camera was also used to record the start, the end, and the movement of the drone during testing sessions. The objectives of the experiments are to answer the following questions: *(a) Does the drone vibrate and move its body when flying as predicted in the previous analysis?, (b) What are the frequencies of such vibrations and movement patterns?, (c) When there is no wind, will the drone body shifting still persist?*

The spectrogram of the collected signal is shown in Figure 3.3. There are two dominant frequencies that are observable from the data. The low frequency (less than 10Hz) components happen at $10^{th}$(s), $20^{th}$(s), $32^{th}$(s), $40^{th}$(s), and $53^{th}$(s), which correspond to the drone's body shifting (confirmed from recorded videos). In addition, the second dominant frequency at $50^{th}$ to $70^{th}$ Hz represents the vibration frequency of the drone body caused by propellers. These results answer the first two questions we mentioned earlier, that the drone constantly vibrates and create iterative body shiftings when it flies. The observed data also shown that the body vibration and body shifting can happen at the same time at some moments.

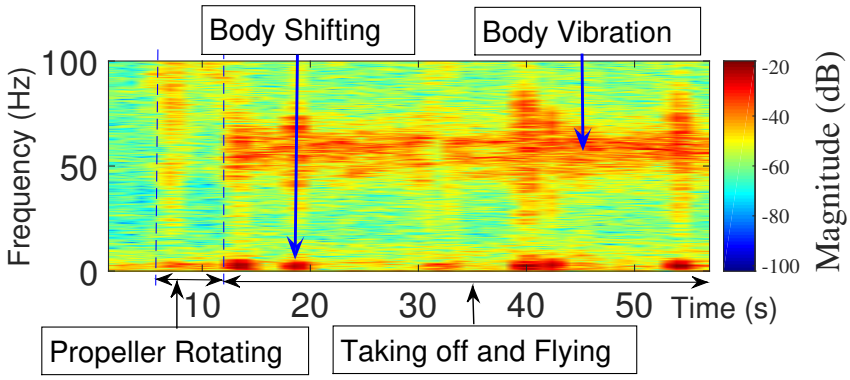


Figure 3.3: Drone body shifting captured by IMU sensors. An example illustrates the movement captured by IMUs attached to the Bebop drone.

To answer the third question, we setup a closed indoor experiment where wind is blocked to a minimal level and the drone circles within a small room. Analyzing the captured IMU data in both time and frequency domain gives us two conclusions: the drone body vibration is still present from the IMU data even without wind; and the body shifting still happens during the time

the drone tries to adjust its pitch and yaw angles to fly in a circular shape. Such drone body movements happen when the drone tries to change its pitch, roll, and yaw angles. In summary, we empirically confirmed that the drone body is shifted even in a windless environment, and the drone body continuously vibrates when it flies. In the next subsection, we will conduct another experiment to validate whether those movements can be captured using RF signals.

#### 3.2.3.2 Feasibility Check: Capturing Drone Body Movements using RF Signals

We conduct the second set of experiments to check the feasibility of capturing the drone movements using RF signals. A wireless transmission antenna is attached to the drone. A wireless receiving antenna is placed at a fixed location to capture the signal sent from the transmitter (which is attached to the drone as illustrated in Figure 3.4). We used USRP B200 mini software-defined radios (SDR) [158] to control the transmitter and receiver antennas. The antennas are connected to USRP SDRs through cables of 6m length. The transmitter antenna emits a single tone wireless signal at 2.4 GHz when the drone is flying. The key idea is to capture the change in RSSI and phase of the transmitted single tone signal to infer the drone body movements. In addition, we also attached the IMUs to the drone and collect the data as the ground truth. The objectives of this experiment are to answer the following questions: *Do received wireless samples correspond to the movements of the drone (a) for body shifting? and (b) for body vibration?*

The results showed that it is possible to capture body shifting and body vibration in the RF domain. First, in Figure 3.5, we plot the raw data obtained from accelerometer data and the phase of the received RF signal. Note that the SDR listens to a WiFi band and demodulates the signal to baseband, after which we compute the FFT. The body shifting peaks corresponding to turning are clearly identifiable and correlated on both accelerometer and RF data.

We conducted experiments to see whether the measured vibration frequency of the IMU matches what we see in the frequency domain of the RF signal. We confirmed that the peak frequency detected in the frequency domain repeatedly matches what we observed via the IMUs. Figure 3.6 illustrates the frequency distribution of RF signal captured with peaks around the 60

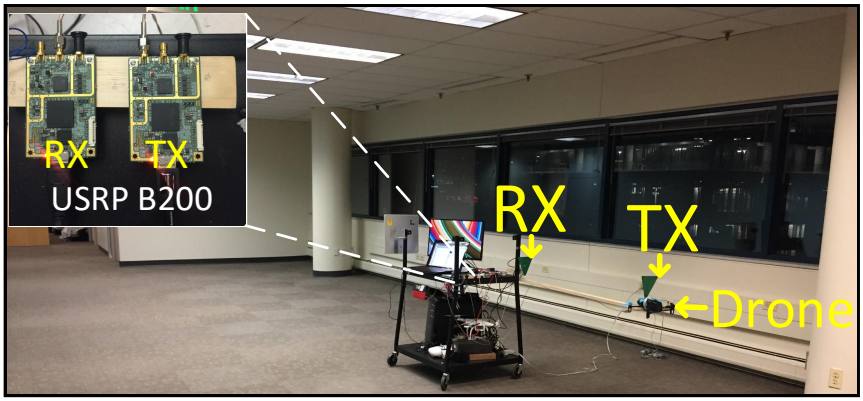


Figure 3.4: The setup for the indoor environment. A transmitting antenna is placed on the drone that continuously transmits wireless signal towards the detection station. A receiving antenna placed on the detection station captures the transmitted signals from transmitting antenna. The transceivers are implemented using USRP B200.

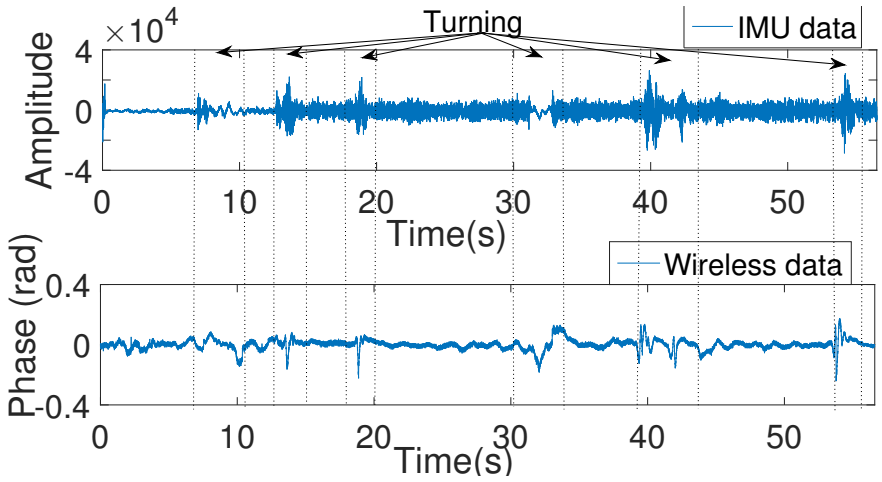


Figure 3.5: Signals captured by the IMU and from RF. Whenever the drone is turnning, there are events captured on both IMU and RF data.

Hz mark, which is similar to the peak on the IMU measurements.

## 3.3 Matthan Drone Presence Detection

We design Matthan, a system that detects the above-mentioned body movements, namely body shifting and body vibration, by passively listening on the radio channels that the drone is using to communicate with its remote controller. A number of algorithms are introduced to capture

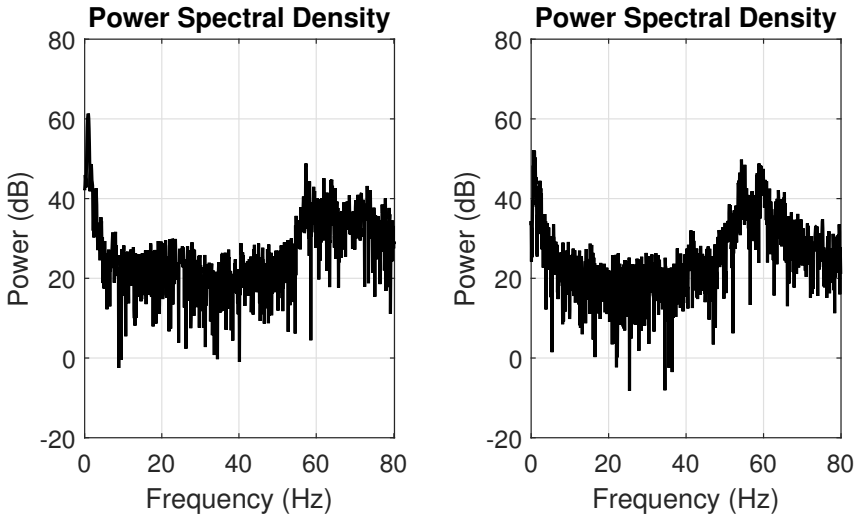


Figure 3.6: The frequency distribution of the signal from IMU (left) and RF (right). The vibration frequency is appeared on both IMU and RF data.

such miniature physical signatures and to identify if it is coming from a drone. In the following subsection, we first formally define our problem and identify challenges in realizing such a system. We then present the body vibration detection method and body shifting detection method before describing a fusion algorithm that combines the two types of movements into a single classifier.

### 3.3.1 Problem Formulation

To detect the presence of drones, Matthan listens to the channel that is used by the drones to communicate with its remote controller. Let the signal broadcast by the drone to its remote control be $\tilde{t}(t)$ at time $t$. The signal Matthan received by listening is $\tilde{r}(t)$. Since the movements of interest are at frequencies that are a few orders of magnitude lower than the carrier frequency or the data rate, $\tilde{r}(t)$ can be filtered to obtain only the low frequency components. Let $\tilde{r_f}(t)$ be the filtered signal. We then have:

$$\tilde{r_f}(t) = q(t) + \eta(t) \tag{3.1}$$

where $q(t)$ is the signal that contains the drone body shifting and body vibration, and $\eta(t)$, which is the environment noise. After removing the DC components, $\eta(t)$ becomes a signal with zero-mean and some variance. Previous experiments show that the drone body vibration happens continuously

over a specific range of frequencies when the drone is flying. In addition, we also found that the drone body shifting has a form that is close to a wavelet $\psi(t)$ due to the characteristic of its rebalancing and control loop mechanisms. Hence, the drone signal $q(t)$ can be written as:

$$q(t) = \psi(t) + Xsin(2\pi ft + \phi) \tag{3.2}$$

where $\psi(t)$ is the function represents the drone body shifting. $\psi(t)$ is the function containing different dominant single tone cosine signals that have amplitude $\hat{A}(\psi)$, frequency $\hat{f}(\psi)$, and phase $\hat{\phi}(\psi)$. And $X, \phi$, and $f$ are the amplitude, phase, and frequency of the drone body vibration. In summary, the key objectives of Matthan are to identify the drone body shifting ($\hat{A}(\psi)$, $\hat{f}(\psi)$, $\hat{\phi}(\psi)$) and the drone body vibration ($X, \phi$, $f$).

[■] **Challenges.** However, accurate and robust drone detection based on RF signals is hard due to the following challenges:

**1) Movements-RF translation.** The drone body shifting and movement information are buried in the wireless signal. This limits the maximum detection range that can be obtained from the system at different environment.

**2) The body shifting can happen at different scales**. Different drones creates different types of body shifting according to their controlling mechanism and accuracy as well as their physical characteristics (weight, structures, and etc.). The signal can be detected at different magnitudes as well as frequencies. However, the shape of the body shifting signal stays relatively constant. We propose a wavelet based technique that is resilient to the scale and magnitude of the physical body shift.

**3) Interference from static APs.** The drone may communicate at the same frequency channel with the wireless APs in the environment. The detection algorithm should be able to distinguish between the signals from the static APs and the signal from the drone. The solution for the next challenge is used to solve this problem.

**4) Interference from mobile APs.** A mobile AP carried by a human walking or an embedded AP on a moving vehicle, e.g. bus, could create similar wireless signals as the drone, which could

affect the detection results (assuming the AP operates at the same frequency with the drone's communication channel). We propose a technique that differentiates the drone from other static or mobile APs based on identifying the body vibration of the drone using RF.

**5) Environment noise**. The noisy and heterogeneous environment makes the problem much more challenging. We introduce an evidence-based classifier to make the detection more robust. The drone presence is detected based on the availability of multiple lines of evidence that uniquely identify the physical characteristics of the drone (i.e., body shifting and body vibration).

**6) Variety of drones.** Drones vary in terms of having different numbers of propellors, weights, sizes, speeds, and communication mechanisms. We present a confusion matrix showing that Matthan's detection approach is promising in terms of discriminating among the specific set of drones that we tested.

### 3.3.2 Drone Detection Algorithm

In this section, we present Matthan's detection algorithms. Since the drone body shifting happens at different scales and environments, it can be detected at different magnitudes as well as frequencies. However, the shape of the signal stays relatively constant. We propose a wavelet-based technique that is resilient to the scale and magnitude of the physical body shift. In addition, we design a Fourier analysis to detect the drone body vibration. We then design an evidence-based algorithm taking the input from wavelet and Fourier analysis to make the final decision.

#### 3.3.2.1 Drone Body Shifting Detection

We use wavelet analysis to detect the drone body shifting. A wavelet is a wave-like oscillation with an amplitude that begins at zero, increases, and then decreases back to zero. Wavelets are especially good at capturing brief oscillations. From the results of our experiment (Sec. 3.2.2), the behavior of the drone body shifting is similar to the form of a wavelet. This characteristic will result in high coefficients when multiplying the wireless signal $\tilde{r}(t)$ with scaled versions of the mother wavelet.

The wavelet, denoted by $w(t)$, maintains local information in both the time and frequency domains. It is defined as a waveform that satisfies the following condition: $\int_{-\infty}^{+\infty} w(t)dt = 0$. The Wavelet Transform [159] uses as the wavelet that satisfies the condition of dynamic scaling and shifting function, $w_{s,p}$,

$$w_{s,p}(t) = \frac{1}{\sqrt{s}} w\left(\frac{t-p}{s}\right) \tag{3.3}$$

where $w_{s,p}(t)$ are the integrated and integral transformation signal, $s$ is the scale and $p$ is the shift parameter, which can also be the central location of the wavelet in the time domain. The wavelet can be stretched and translated with flexible windows by adjusting $s$ and $p$, respectively. The wavelet transform of the wireless received samples $\tilde{r}(t)$ using transform coefficient $W(s,p)$ is calculated as following:

$$\begin{aligned} W(s,p) &= \int_{-\infty}^{+\infty} \tilde{r_f}(t)\overline{w_{s,p}}(t)dt \\ &= \frac{1}{\sqrt{s}} \int_{-\infty}^{+\infty} \tilde{r_f}(t)\overline{w_{s,p}}\big(\frac{t-p}{s}\big)dt \end{aligned} \tag{3.4}$$

where $\overline{w_{s,p}}(t)$ represents the complex conjugate of $w_{s,p}(t)$. The result of the wavelet transform gives us a correlation function of the template signal at different scales (frequency bands) in both the time and frequency domains. As in Equation 3.4, the correlation function $W(s,p)(t)$ has two main features as follows. (1) The time resolution is high with high frequencies while the frequency resolution is high with low frequency signals. When multiplying the high frequency component of the signal with the high frequency of the wavelet, the correlation result will indicate the exact location where it happens. This can be used to identify the very first body shifting event created by the drone. (2) As the wavelet has local existence in both time and frequency domain, the point of discontinuity in the signal can be detected with high sensitivity. As the discontinuity (generated by body shifting) is considered as an event and happens quickly in time, the result of correlation with high frequency wavelet will be readily captured.

Let $W_m(s,p)$, $W_{vi}(s,p)$, and $W_\eta(s,p)$ be the wavelet transform coefficients of the signal caused by the drone body shifting, drone body vibration, and the noise, respectively. The wavelet

transform coefficient of the sum of the signals is calculated as follows:

$$W_{m+vi+\eta}(s,p) = W_m(s,p) + W_{vi}(s,p) + W_\eta(s,p) \tag{3.5}$$

Because of the linearity property, the coefficients of the wavelet transform enable us to precisely identify the body shifting event in the time domain when there is a signal discontinuity. As the drone body vibration and the noise are quite constant over time, these behaviors decay quickly after different levels of scaling, leaving the body shifting component. The wavelet transform coefficients then give us two valuable pieces of information for event detection: the location and the duration of each body shifting event. Figure 3.7 (top) depicts the results of the wavelet transform at 64 scales of the received wireless samples where the drone body shifting events are correctly identified.

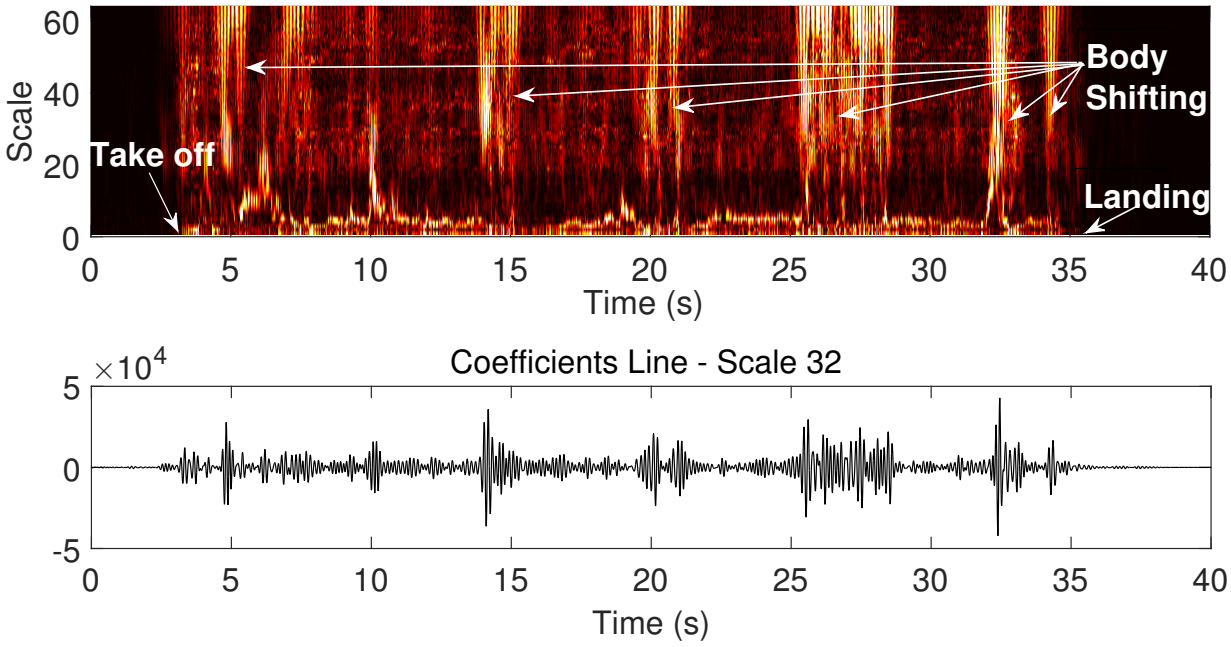


Figure 3.7: Wavelet analysis result of body shifting detection. When the drone body is shifted, the events can be captured using continuous wavelet analysis.

To identify exact time and frequency of the drone body shifting, Matthan decomposes the signal into a sequence of sub-frequency bands and approximates the energy of each frequency band.

Energy of each sub-frequency is calculated as following:

$$\xi_i = \int |f_i(t)|^2 dt = \sum_{k=1}^{n} |f_i(k)|^2 \tag{3.6}$$

where $f_i(t)$ is the signal of $i$ frequency band, $f_i(k)$ is its discrete value. The system compares the energy of each frequency band, then reconstructs the coefficient of special sub frequencies that have enough energy and contain the frequency of drone body shifting.

The center of the signal can be calculated according to the definition of the gravitational center in mechanics, namely the center of the body shifting event in time is given as:

$$t_{center} = \frac{\int t|f(t)|^2 dt}{\int |f(t)|^2 dt} \tag{3.7}$$

Then, the width of the window function of the STFT can be calculated from the central point to the point where the coefficient value $W_{s,p}$ drops down to the noise band. Hence, the above results gives us the time center and the width of the function. We then can perform STFT to analyze the frequency of the drone body movement. The peak of the frequency distribution resulting from STFT identifies the frequency of drone body shifting $\psi(t)$.

#### 3.3.2.2 Drone Body Vibration Detection

As seen earlier in Figure 3.3, the drone's vibration creates a periodic signal that is well-reflected in the FFT-based spectrogram. Conversely, a wavelet transform that is better-suited for capturing transitory phenomena such as a body shifting event is not well-suited for drone vibration detection. Consequently, we employ a frequency domain approach to identifying the presence of the drone's vibration signal. Recall that the wireless signal component that is affected by the drone body vibration has the form of $Xsin(2\pi ft + \phi)$. From the received wireless sample $\tilde{r}(t)$, an efficient approximation of the drone's vibration frequency is to identify the dominant frequency component that has maximum power spectrum density (PSD) through the STFT. Then, the approximation of the drone's vibration frequency $f_v$ is as follows:

$$f_v = \max_{[f_{min} \to f_{max}]} \left( \left| \sum_{k=1}^{N} \tilde{r_f}(t) e^{-j2\pi ftk} \right|^2 \right) \tag{3.8}$$

where $N$ is the number samples. After $f$ is estimated, it can be used to estimate the amplitudes and phases of different frequency channels using the following:

$$X = \frac{2}{N}|\sum_{k=1}^{N} \tilde{r_f}(t)e^{-j2\pi ftk}| \tag{3.9}$$

$$\phi = actan\frac{-\sum_{k=1}^{N} \tilde{r_f}(t)sin(2\pi ftk)}{\sum_{k=1}^{N} \tilde{r_f}(t)cos(2\pi ftk)} \tag{3.10}$$

In this way, the system obtains the desired quantities $[X, \phi, f]$.

#### 3.3.2.3 Evidence-Based Drone Detection Algorithm

We design an algorithm to determine if a drone is present by first gathering evidence from multiple sources that relate to drone body shifting and vibration, then combine these sources of evidence to form a binary classifier. The overview structure of Matthan is illustrated in Figure 3.8.

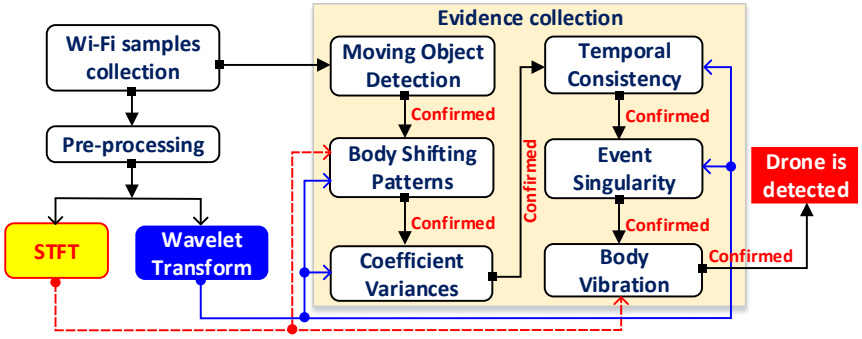


Figure 3.8: The overview architecture of Matthan. Wi-Fi samples captured from the drone is pre-processed and analyzed using Fourier Transform and Wavelet Transform. The Transformed signals are then put into an evidence collection to confirm the presence of the drone. The drone is detected when all the evidences are confirmed.

- **Evidence #1: Moving Object**. The first evidence to collect is the presence of a moving object using RF signals. This of course is not a unique indication of a drone but of any moving object such as a human walking while carrying a phone or a phone inside a car. Matthan calculates the standard deviation of the received wireless signal and compares it with the standard deviation of the environment at the time of initialization. The standar

deviation of the signal without moving objects, denoted by $\delta_0$ is an environment independent quantity [160] and it represents the received signal changes caused by electronic noise. Received signals are dominated by *quantization errors* and *electronic noise*. Therefore, the signal follows a Gaussian distribution with zero-mean after DC removal [160]. On the other hand, when the drone or other moving object is in the environment, the received signals are expected to follow the distribution of multipath fading because it dominates the other noise sources. A log-normal, Ricean, or Rayleigh distribution is expected to represent the distribution of the collected data with such multipath affects. As a result, the comparison between the standard deviation of the signal at test and $\delta_0$ can be done to confirm this evidence.

- **Evidence #2: Drone Body Shifting**. As mentioned in Section 3.3.2.1, the drone body shifting event serves as one of the main indications of drone presence detection. Since the shifting follows a certain pattern in space, it can be amplified and detected using wavelet transformation. We use Mexican hat wavelet [161] as the template of comparison because this wavelet has a similar waveform to the drone's body shifting event shown before. It is important to note that the speed (i.e how fast it shifts) and amplitude (i.e. how much it moves) of the shifting might vary from one movement to another. Therefore, our evidence confirmation method must be designed to detect a specific range of speeds (i.e. frequency) and amplitudes (i.e. wavelet scale). We propose a two-step process for confirming the body shifting by looking at the signal from both frequency and wavelet domains. In particular, we (1) acquire the frequency of the body shifting as shown in Section 3.3.2.1. We then (2) compare the waveform of the shifting with the template by calculating the coefficient between the two using the Dynamic Time Wrapping technique [162, 163]. The evidence is confirmed when the frequency is less than 5Hz and the coefficient is under a preset threshold. This threshold is determined by the practical possible range of body shifting amplitude.

- **Evidence #3: Coefficient Invariance**: This evidence is to confirm that the body shifting is a discrete event that is similar to the template. The intuition for this evidence stems from the fact that body shifting movements are unexpected and non-uniform events triggered by various environmental and electronic artifacts. As a result, two or more consecutive body shifting motions are not expected to be similar. As one of the wavelet transformation properties, coefficient invariance can be used to confirm if a template is present on a trunk of signal once and only once. In particular, the coefficients are retained and even enhanced as the transformation scale increases [164] for each body shifting event. Hence, if the signal is of the template form and non-repetitive for 4 consecutive body shifting cycles, the body shifting event is confirmed. In short, the coefficient invariance evidence is confirmed if the coefficient magnitude monotonically increases across multiple body shifting events detected by evidence #2 as the transformation scale increases.

- **Evidence #4: Temporal Consistency**: While the previous evidence (#3) can capture the discontinuity and repetitive of an event, it could also introduce false positive by counting *short* and *discrete surges* of signals caused by noises in the environment. This evidence is introduced to address this very issue. The key idea is to observe the spread of the signal at different sampling rates. As the sampling rate reduces, the coefficient of the noise (discrete surges) decays because the wireless samples that represent the surges are reduced or disappear. Let $t_1$ be the spread of the signal at sampling rate $f_{s1}$, $t_2$ be the spread of the signal at sampling rate $f_{s2}$, $f_1 > f_2$. $t_1$ and $t_2$ can be approximated from the spread of the wavelet coefficient that is over the threshold. Wavelet decomposition [165] is used to collect this evidence. If $t_1$ and $t_2$ at two consecutive levels of decomposition are close to each other, the evidence is confirmed.

- **Evidence #5: Event Singularity**: As the fluctuation of the drone is in the wavelet pattern, the direction of fluctuation is very unique. The direction of the body shifting can be obtained by the sign of extremum of the *wavelet coefficients*. The direction must be changed

between two consecutive extrema at the same frequency with that of the body shifting at different levels of decomposition. To confirm the fluctuation is from the drone body, the sign of the extremum coefficient needs to alternate while the magnitudes of coefficients remain similar. While evidence #2 shows the similarity of the signal representing body shifting and the template, evidences #3 and #4 make sure there is no false positive due to the noises in the RF domain, evidence #5 confirms that the change of body shifting behavior should cross-interleave the balance state.

- **Evidence #6: Drone Body Vibration**: As shown in subsection 3.3.2.2, the drone body vibration is observable through a short-time Fourier analysis. The evidence is obtained when maximum power distribution of the peak frequency belongs to the range of drone's body vibration. This evidence is used to identify the drone versus other interference sources such as mobile AP carrying by a walking user or the embedded AP on a moving vehicle.

The different forms of evidence are collected at each time window. The decision is made based on the number of forms of evidence that are confirmed on each window. We sort the evidence based on their uniqueness as the signature for drones. All the evidence is combined linearly for the final decision of detection. That is, Matthan concludes a drone is present only when all the forms of evidence are confirmed. In Section 4.6, we show the contribution of each form of evidence to the accuracy of Matthan.

## 3.4 Performance Evaluation

### 3.4.1 Experimental Setup

We implement Matthan using the SDR USRP B200 mini [158]. The USRP board is sampled at 100kHz to collect wireless samples from the drone's communication channel. The USRP board is configured as a receiver connecting to a 2.4GHz 20dBi gain directional antenna [166]. The wireless samples collected from USRP are sent to a laptop for data processing and filtering. The Wi-Fi channel of the drone's communication is identified by Wi-Fi Analyzer [167]. This application

provides the channel ID and frequency for listening to the drone's communication. The collected data are stored in binary files and further processed using MATLAB.

We conducted experiments in three different environments including a parking lot in the downtown of a city (*urban*), a soccer field inside our university (*campus*), and an open field (*sub-urban*) as depicted in Figure 3.9. In each environment, the data are collected when the drone is flying at different distances with respect to our receiver. We collect data at the maximum distance of 100m, 200m, and 600m in urban, campus, and sub-urban environments, respectively. The drone is controlled to *take off* and *hover* within the coverage area of the antenna receiver's beam during all experiments.

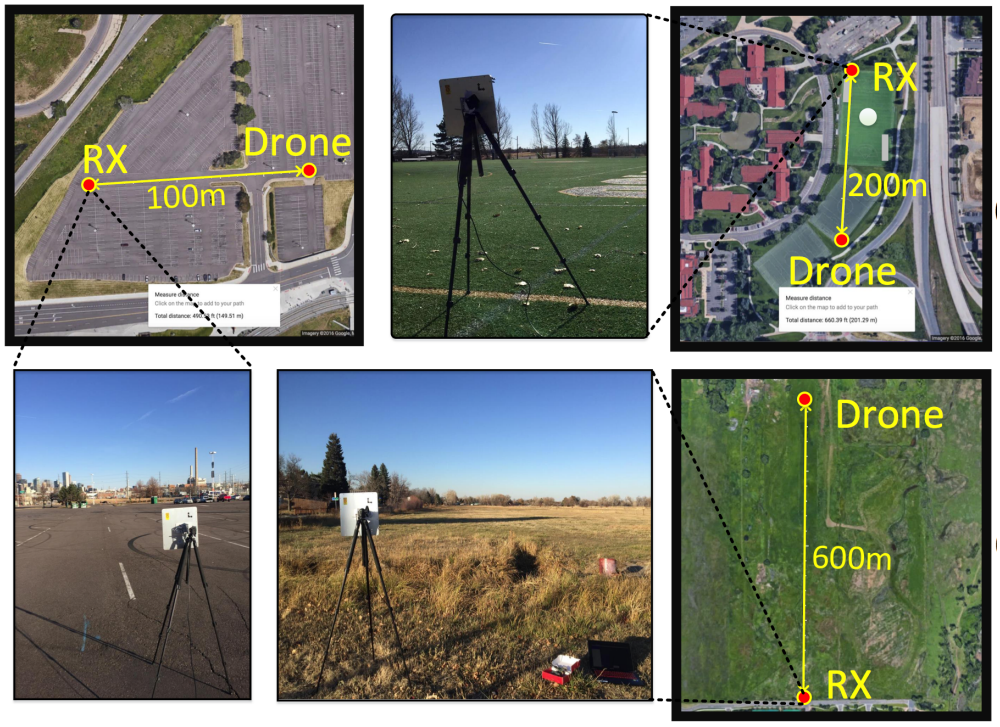


Figure 3.9: Testing locations: (a) Urban (Parking area), (b) University campus, and (c) Sub-urban

The experiment was conducted on 7 different drones of different models and manufacturers as shown in Figure 3.10, including the Parrot Bebop [153], Protocol Dronium One Special Edition [168], Sky Viper [169], Swift Stream [170], Parrot AR DRone [171], Protocol Galileo Stealth [172], and DJI Phantom [154]. The Bebop, Dronium, Skype Viper, ARDrone, and DJI

Phantom send Wi-Fi signals from the Wi-Fi card mounted on their body for either controlling the channel or streaming video. Protocol Galileo Stealth and Swift Stream emit Wi-Fi signals from the plug-n-play cameras came with the drones.

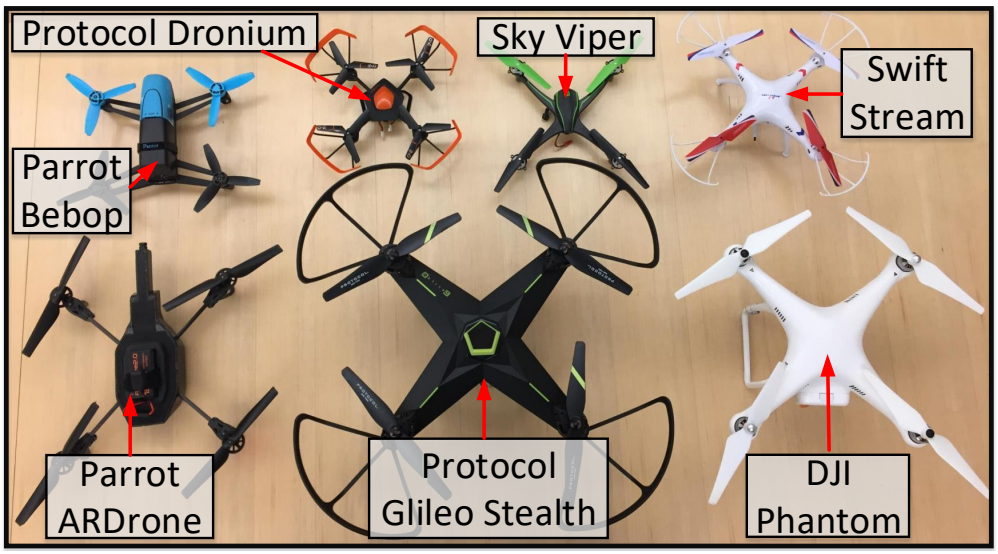


Figure 3.10: Drones used during experiments. There are 7 different types of drone used during the experiment. Bebop and ARDrone are from Parrot, Glileo Stealth and Dronium are from Protocol, and other drones are from different companies.

To test whether the drone's RF signal could be differentiated from those of other mobile wireless devices, we also evaluated two other scenarios when a mobile AP was carried inside a moving vehicle or by a walking person. First, the user configures a mobile device to create a Hotspot (mobile AP) to emit Wi-Fi signals. We use another mobile phone (client phone) to connect to the mobile AP. The client phone streams Youtube video continuously. We asked the user to carry both client and the mobile AP to walk around at a distance of 50m away from the wireless system. Secondly, the client and mobile AP are placed inside a car which moves around in the coverage area of the wireless system at a distance of 50m to 100m away. The vehicle is moving at 20 mph (32 km/h) speed. In both scenarios, the mobile AP and client are always within the coverage area of the system.

We then segmented the collected data into two main types: *drone* and *no drone*. Each segment has a length of 10 seconds. The "drone" data contains the wireless segments that correspond to the

moment where the drone is flying in the environment. Similarly, the "no drone" data contains the wireless segments that correspond to the moment at which there is no drone in the environment (the drone is completely turned off). More specifically, the "no drone" data contains types of data including "environment noises", "human carrying mobile AP", and "mobile AP augmented inside a car".

### 3.4.2 Evaluation Results

In this section, we evaluate the performance of Matthan at different distances (from 10m to 600m), with 7 different types of drones, and at different environmental setups (urban, campus, sub-urban). We use *accuracy*, *precision* and *recall* as the performance metrics for evaluation. The *accuracy*, *precision*, and *recall* are calculated from True Positive ($TP$), True Negative ($TN$), False Positive ($FP$), and False Negative ($FN$). The calculations are given as follows: $accuracy = \frac{TP+TN}{TP+FP+FN+TN}$, $precision = \frac{TP}{TP+FP}$, and $recall = \frac{TP}{TP+FN}$.

#### 3.4.2.1 Detection Performance vs. Number of Evidences

As stated in Section 3.3, Matthan makes detection decision by collecting evidences that are resulted from its analysis of the collected wireless samples.

We run the evaluation on the segmented data set of 600 segments of 10 seconds data (300 segments of drone's presence and 300 other segments from the environment, human walker carrying mobile AP, and mobile AP inside a moving car). This data is collected when the Bebop is at 50m distance from the Matthan system. The performance of detection is shown in Figure 3.11 in which the evidence IDs are corresponding to the IDs presented in Section 3.3. As can be seen, the accuracy of the system is as low as 83.7% when the system uses only the first form of evidence to detect the drone. More importantly, the system obtained a precision of detection around 78.9%. Such performance is not really usable for reliable detection. So, the first evidence only helps to detect the drone in an environment where the system receives minimal interference from other Wi-Fi sources. However, based on this evidence, Matthan cannot detect the drone within environments

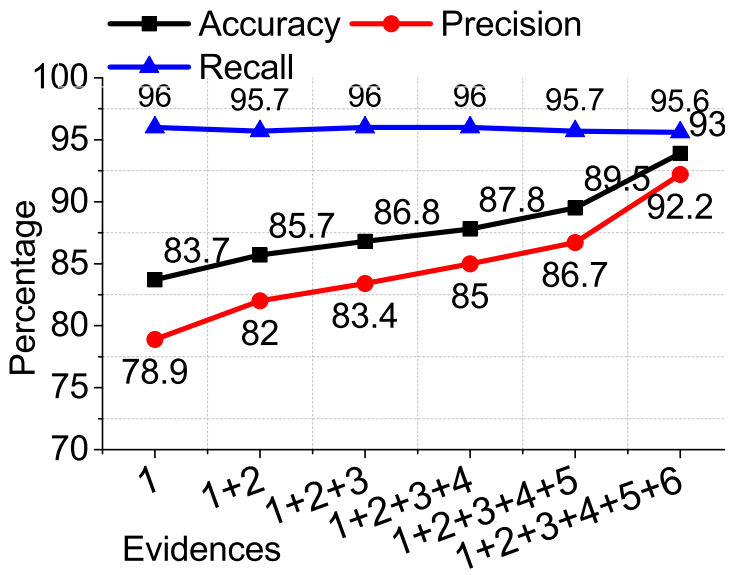


Figure 3.11: Detection accuracy with increasing forms of evidence. The accuracy improves when increasing the number of evidences. In particular, when the last signature is added (body vibration), the accuracy significantly increases from 89.5% to 93%.

that contain a large amount of interference. When more evidences are combined, the performance increases significantly. More specifically, we can observe how the false positive rate diminishes and precision correspondingly rises as more evidences are integrated. Initially, the precision of the system is as low as 78.9% with only one part of evidence and increases successively to 86.7% once the first five forms of evidence are considered. Matthan does not recognize all of the wireless samples representing a human carrying an AP or a mobile AP inside a car as drone data because the standard deviations of the wireless samples in these cases are sometime smaller than the detection threshold. From our observations, the standard deviations of the signal in these scenarios are only incorrectly identified as the signal from the drone only when the user goes toward or backward Matthan (with distance less than 5m). Finally, when the vibration detection is considered (evidence #6), the overall *precision* rises to 92.2% (corresponding with 93.9% of *accuracy* and 95.6% for *recall*). This result is obtained due to the fact that the last evidence is well-represented for the uniqueness of drone's body vibration in the environment.

#### 3.4.2.2 Impact of distance

We also analyze the impact of the distance between the detection system and the drone on Matthan's performance. The evaluation is conducted for both short and long distances. At short distances, we analyze the performance of the system when the drone is from 10m to 100m away. Bebop data from the urban environment experiment is presented for this analysis. At each location, 600 segments of data are analyzed (300 segments of drone's presence). All 6 forms of evidence are used to calculate the results of detection. The results are shown in Figure 3.12. The system obtained up to 96.5% of *accuracy*, 95.9% of *precision* and 97% of *recall* when the drone is 10m away from the detection system. When the distance increases, the performance of the detection falls to 89.4% of *accuracy*, 86.7% of *precision* and 93% of *recall* at 100m. Note that with audio-based detection techniques, the most recent report shows that the drones are correctly detected with distance less than 30m, and this technique completely fails with distance more than 50m [173]. Similarly, video techniques can be performed for detection at distances less than 50m with large drones [174, 175].

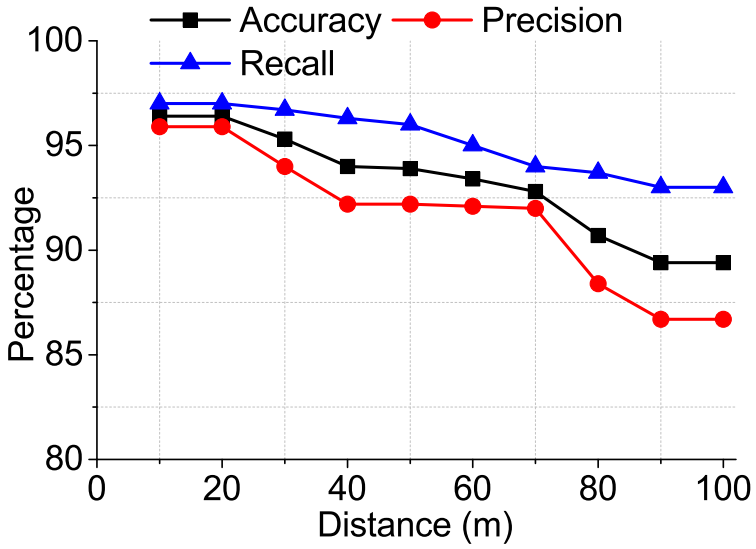


Figure 3.12: Detection accuracy at different distances. The accuracy is reduced when the distance is increased. In particular, the performance is dropped noticeable when the distance is greater than 70m

The Matthan's performance is further evaluated when the distance between the drone and

Matthan is from 200m to 600m. We used a sub-urban data set for this evaluation. We used 200 segments (100 segments with drones' presence) at each distance to evaluate the system. Figure 3.13 shows the performance of Matthan at these longer distances. The system obtained 84.9% of *accuracy*, 81.5% of *precision*, and 90.3% of *recall* at 600m distance. We were limited to 600m due to the space constraints of the testing location, but hope to find another venue with greater range.

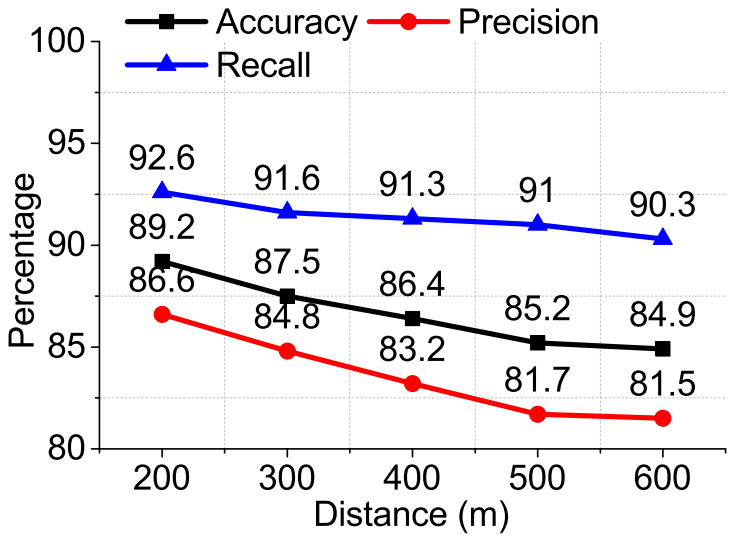


Figure 3.13: Detection accuracy at long distances. Matthan is able to detect the drone presence with distance up to 600m. We stopped the experiment at 600 m due to the limited space of the testing area.

#### 3.4.2.3 Impact of environmental setup

We also evaluate the impact of the environment noise to Matthan's performance. We use the 50m data set from the Bebop drone at three locations (urban, campus, and sub-urban) for this evaluation. The impact of mobile APs is also taken into account. One half of the data set are from the drone, another half includes the data from the environmental noises and human carrying a mobile AP. The data from mobile APs inside the campus environment is not available because we cannot drive a car inside the campus. The results of drone detection are shown in Figure 3.14. We use 600 segments of data and 300 segments from the drone's presence. The system obtained the best

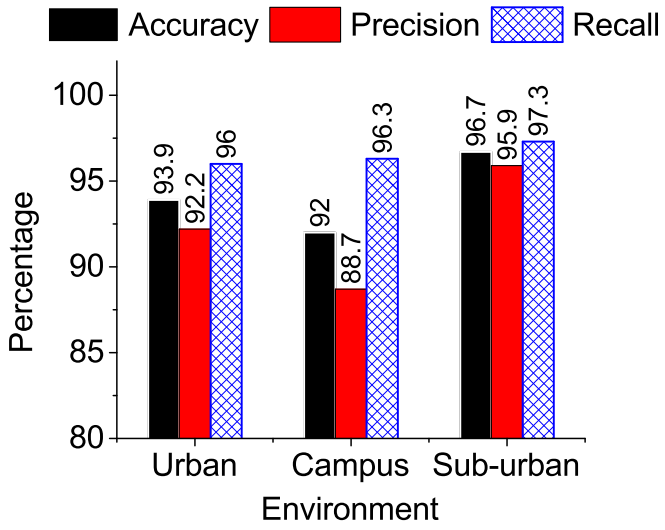


Figure 3.14: Detection accuracy in different environments. Matthan is validated at three main environment, the system obtains great performance in all of these scenarios.

performance in the sub-urban environment as this area has little effect from environmental noise as well as multi-path reflection. The system can achieve up to 96.7% of *accuracy*, 95.9% and 97.3% of *precision* and *recall*, respectively. The campus environment has a number of wireless access points operating over different Wi-Fi channels, and hence it is found that the drone communication channel usually interferes with other static APs in the campus environment. At the time of the experiment, there were 16 Wi-Fi APs in the same vicinity using Wi-Fi Analyzer app [167]. Therefore, the system creates more false alarms (false positive) in the campus environment compared with urban and sub-urban environments. However, Matthan still performs 92% of *accuracy*, 88.7% of *precision* and 96.3% of *recall* in the most interfering environment (campus).

#### 3.4.2.4 Impact of time budget

Detecting the drone is also challenging due to the limited time budget within which the drone flies across the detection system. We are interested in analyzing the detection accuracy of Matthan with different time budgets for detection. The key motivation is to understand the performance when the drone stays longer inside the coverage area. We use the data set from the Bebop drone at 50m distance in an urban environment for this evaluation. We use 600 segments of data with 300

segments from the drone's presence. We increase the duration of each measurement (segment) from 10s to 60s, and a decision is made for each segment. Figure 3.15 shows the performance obtained for different time budgets. Matthan obtains up to 95.5% of accuracy with 60s budget of detection. The *accuracy* and *recall* increase as we give more time for Matthan to make a decision, unlike the *precision*.

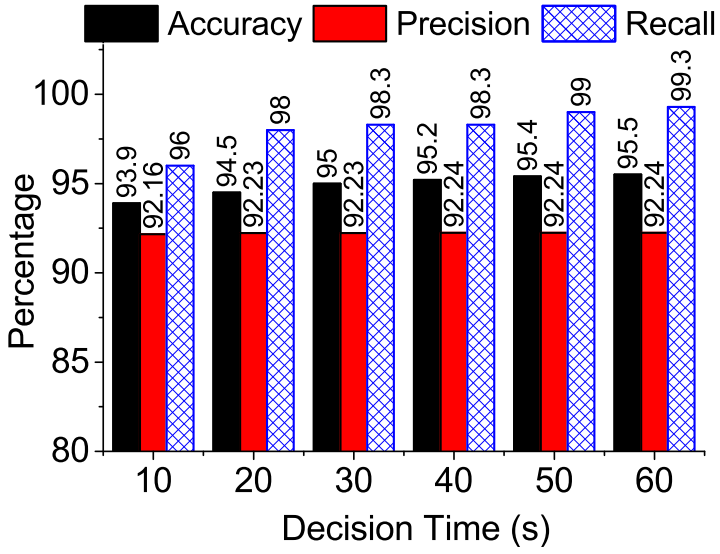


Figure 3.15: Detection accuracy with different decision times. Matthan detection algorithm obtains good performance with the more than 10 seconds of data samples with minimum accuracy of 93.9%.

#### 3.4.2.5 Performance across different drones

We evaluate the performance of Matthan for different types of drones including Parrot Bebop [153], Protocol Dronium One Special Edition [168], Sky Viper [169], Swift Stream [170], Parrot AR DRone [171], Protocol Galileo Stealth [172], and DJI Phantom [154]. Galileo Stealth and Swift Stream and some small drones in the market are usually configured at a specific frequency that does not belong to any Wi-Fi's channel. These drones are very light-weight and cannot carry much weight. They usually utilize a Wi-Fi camera for video streaming and navigation. As the camera is attached to the drone, the wireless signal emitted by the Wi-Fi camera would be very similar to the controlling signal from the drones if there is no shock absorbing mechanism is in-place for

the camera. We found that it is the case in the drone of our procession in this experiment. Figure 3.16 shows the accuracy of detecting different drones using Matthan. Matthan performs with the highest detection results for heavy drones such as Bebop, DJI, Galileo Stealth, and ARDrone. We found that those four drones generate similar signatures in body shifting as well as vibration frequency range. The Dronium and Swift Stream drones are more light-weight. We observed that there was less vibration generated in the light-weight drones than the heavier ones, which explains the improved results for the heavier drones.

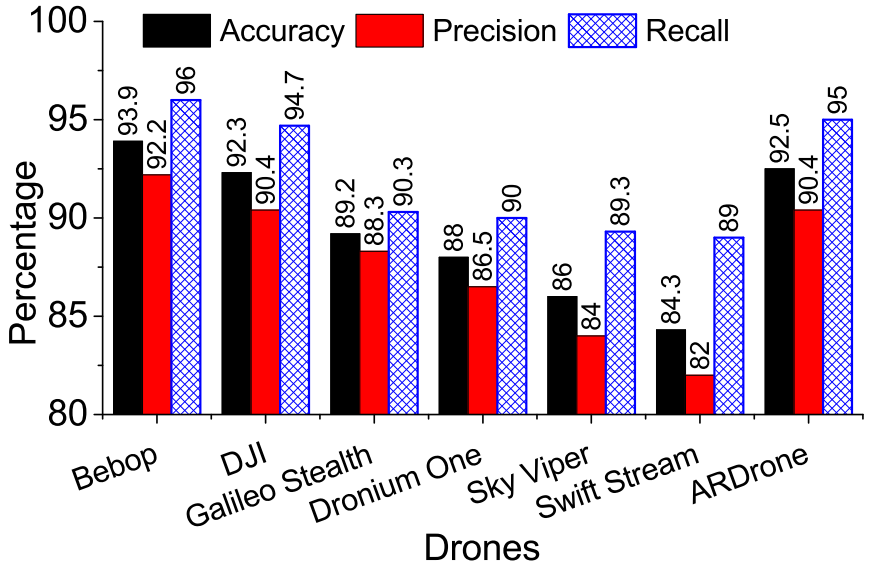


Figure 3.16: Performance across different drones. Matthan is evaluated using 7 different types of all. The results are compared when the distance from the drones to Matthan antenna is 50m.

#### 3.4.2.6 Drone classification

It is also important to identify which drone is flying in the coverage area after detecting its presence. Though it is not the focus of this work, we want to explore if it is even possible with Matthan. We conducted a classifier based on the physical characteristics of the drones to detect them. The key idea is to identify the frequency of vibration of each drone to detect/classify it. Drones are often uniquely designed in weight, structure, materials, propellers' size and so on.

. Those characteristics affect the forces generated by the propellers and therefore also affect the vibration frequency of the drones. We employed a similar experimental setup as in section 3.2.3.1. We attached the IMUs to different drones to collect the motion data. The motion data is then analyzed to determine the central and the dominant frequencies of vibration. According to this central frequency, we approximate the vibration frequency windows as following: Bebop drone (60 Hz), DJI (100 Hz), Galieo (140 Hz), Dronium (35 Hz), SKy Viper (50 Hz), Swift Stream (20 Hz), and AR Drone (70 Hz).

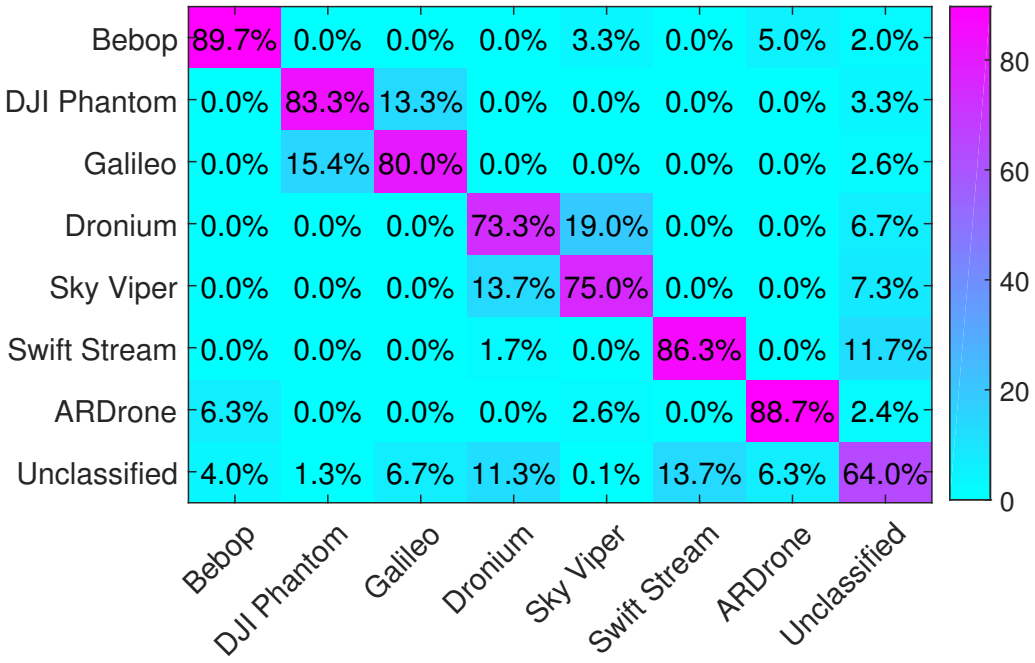


Figure 3.17: Drone classification. Confusion matrix from drone classification based on FFT analysis. Matthan is also able to classify 7 different type of drones based on the central frequencies of their vibrations. However, the current accuracy is limited, we reserve the improvement of this method for future work.

## 3.5 Discussion

Our system has focused on detecting the presence of drones through their unique inherent physical movement signatures on WiFi domain. We wish to expand our experiments to consider a wider variety of drones and greater distances. Our system should be expanded to incorporate

automated channel sensing [176, 177, 178, 179], as the current experiments fix the eavesdropping to a specific communication channel. Such an approach should improve our ability to detect diverse drones that operate with different protocols over the same unlicensed Wi-Fi frequency bands, or that communicate on non-Wi-Fi frequency bands. Our system should also be enhanced to integrate automated antenna steering/ beamforming, as our current experiments fix the direction of the antenna. Note that the directional antenna is only used for improving the gain of detection at a certain direction, omi-directional antenna can also be used to detect the presence of the drone. Localizing the position of the drones is the next logical step, but this consideration is outside the scope of the current research scope.

We would like to conduct experiments that test non-line-of-sight RF detection in the presence of occlusions such as buildings. We intend to pursue further the extent to which Matthan can distinguish between individual drones as well as different types of drones. We also desire to conduct a more detailed examination of fusion algorithms such as boosting and bagging for combining multiple weak detectors into a stronger fused detector. In addition, we wish to detect other aspects of the drone beyond merely its presence, such as its location, speed and direction. Also in the future we hope to address the fact that our system is not currently capable of detecting multiple drones in the same vicinity at the same time. Moreover, we would like to evaluate the impact of the environment, e.g. windy condition, to the accuracy of detection. Finally, while reactive control [148] is considered as one solutions to reduce a number of body-shifting events, Matthan's algorithm can be slightly modified to update the weight of each evidence to focus more on the impact of the drone's body vibration in detection.

## 3.6 Conclusion

This chapter introduced Matthan, a system for detecting the presence of drones by identifying unique signatures of a drone's body vibration and body shifting in the Wi-Fi signal transmitted by a drone. The joint detector integrates evidence from both a frequency-based detector that looks for the maximum frequency peak to be in the range of 50-220 Hz to indicate drone body vibration as

well as a wavelet-based detector that captures the sudden shifts of the drone's body by computing wavelets at different scales from the temporal RF signal. Matthan was prototyped and evaluated using SDR radios in three different real-world environments. When given a mix of data containing both drone and non-drone cases (Wi-Fi-equipped car, walking user with a smartphone on, and no drone scenarios), we showed that Matthan is capable of differentiating drone signals from other mobile wireless devices by achieving high accuracy, precision and recall, all above 90 percent at 50 meters. We also showed how Matthan's accuracy, precision and recall varies with distance, dropping to 90 percent accuracy and 80-85 percent precision and recall at a distance of 600 meters. Matthan's performance was studied across seven different drones, where the performance varied only moderately, and was tested across three different environments, again varying only moderately in performance. We also present how Matthan's performance improves as it is allowed more time to accumulate data. Finally, a confusion matrix illustrates Matthan's potential to identify specific drones from among seven different drones.

## 3.7 Looking forward

We found that that drone privacy and security research could include two main stages of development, i.e. single and multiple drone detection and characterization. While Matthan has contributed to the first milestone on detecting the presence of single drone, the challenges in detecting and characterizing multiple drones at the same time remains unsolved. In particular, these challenges focus on how to characterize the drone more precisely as well as how to detect multiple drones at the same time. First, given the high speed of drone movement, characterizing a drone at a greater details such as cargo load, number of propellers, manufacturers features, and etc. is difficult. In addition, when multiple drones appear in a monitored airspace, this challenge becomes even more challenging. A network of wireless sensing stations are needed to overcome these issues. Second, we are also investigate on how to realize single or multiple drones localization and tracking. Such system requires a novel solution in coordinating multiple sensing stations to accurately identify the location of the drone and continuously track them in real-time. At last, we also need to

find a solution to synchronize all the sensing station in the network. The drone physical signature must be exchanged across the nodes in the drone-defense network to gather sufficient for detection and characterization. A proper wireless network protocol must be designed to collaborate and coordinate multiple wireless sensing stations to detect, analyze, and track the drones when they fly at high speed. In addition, a novel network synchronization technique is required to overcome MHz-level operation of state-of-the-art software-defined-radio platform for gathering the data at multiple wireless sensing stations properly.

# Chapter 4

## Exploring a Novel Way for Indoor Localization Using GPS Signals

### 4.1 Introduction

Until now, GPS-enabled devices cannot accurately localize their locations when they are indoor since GPS signal becomes very weak and even unavailable. Therefore, critical safety application such as localizing 911 caller still has to rely on localization services which have poor accuracy such as E911 [180]; E911 currently provides the service with 50m of accuracy using existing LTE-based positioning technique [181, 182, 183]. As another critical application, tracking fire-fighters during rescuing operations often fails due to the complex structure of buildings [184, 185].

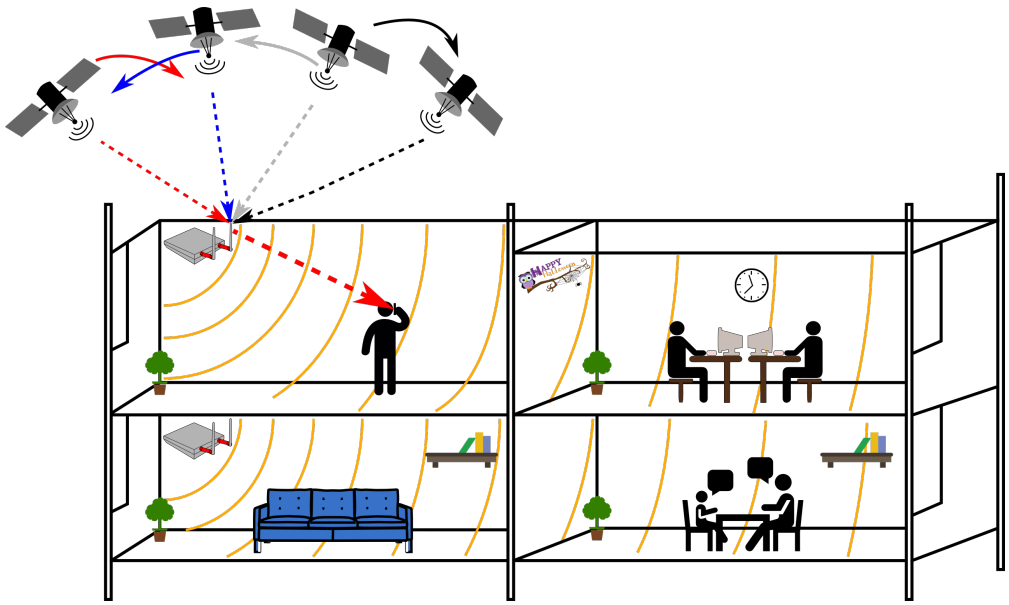

Figure 4.1: The proposed system receives live GPS signal from outdoor and re-radiate it to indoor. When GPS signal is available indoor, GPS receiver runs *WiGPS* algorithm to accurately localize its own location.

Most of the existing indoor localization techniques rely on either fingerprint-based approaches [186, 59, 187, 63, 83, 188, 189] or Wi-Fi RF signals that require infrastructure modification (e.g., Wi-Fi APs and clients must be equipped with multiple antenna-array) [73, 74, 75, 85, 77, 78, 190]. While these techniques could deliver very high accuracy (up to a few decimeters), they either require significant effort in building and maintaining a fingerprint database, require explicit packet transmission between the device to be localized and APs, or require sophisticated and dedicated infrastructure. These approaches are unlikely applicable to the aforementioned applications due to these requirements.

There is a recent effort in making GPS receiver to work indoor called COIN-GPS [45]. COIN-GPS has successfully received weak GPS signal in an indoor environment at the cost of building a sophisticated receiver with a directional antenna array. While is a promising concept, the technique does not work with off-the-shelf receivers such as COST smart-phone and cannot be used where GPS signals are unreachable including underground parking, multi-story building, or even basement at the residential area.

In this work, we aim to provide a global in-door positioning system utilizing the ubiquity of Wi-Fi APs to establish the missing links between satellites and COST GPS receivers due to building occlusions. Doing so will allow user devices to use its GPS receiver to continuously localize and track its own location.

To that end, we are exploring a feasibility of designing a system which can make GPS signals available to indoor environments by relaying them via the existing Wi-Fi APs. Our goal is to make the Wi-Fi AP work as a GPS relayer and the user device localizes itself without performing any communication with the APs. Although there are several types of indoor devices such as light-bulb and smoke detector in practice, the proposed system is designed to be attached onto Wi-Fi APs because it provides: (i) high possibility to receive GPS signal directly from outdoors, (ii) high deployment density to cover almost the whole area inside a building, and (iii) high RF transmission gain from their external antennas. Piggybacking on the existing WiFi APs for localization benefits from the facts that they (1) are ubiquitous, (2) high deployment density to cover almost the whole

area inside buildings, (3) are not power-constrained since they are powered by the external power sources. However, realizing such idea is difficult due to the following challenges:

- *Wi-Fi AP does not support GPS frequency.* Wi-Fi operates at 2.4GHz/5GHz frequency while GPS operates at L band frequencies (L1: 1575.42 MHz, L2C: 1227.60 MHz, and L5: 1176.45 MHz).
- *Difficult to modify hardware or software on the APs.* It is challenging to make the relayed GPS signal decodeable by the GPS receiver without modifying the signal itself. This modification however needs to be done at the relayer (i.e. the APs) if any. However, to make the solution practical, deployable and scalable at low cost, no modification is allowed on existing Wi-Fi AP hardware and software.
- *Inherent low localization accuracy of GPS signal.* GPS signals undergo several types of impairments that introduce errors in position estimation, especially on the pseudorange measurement. It is even more so after being relayed by the APs.
- *Impact of multipath reflections.* In contrast with signal found in the outdoor scenarios where GPS receiver often estimates its location using the GPS signal coming from the direct path, the proposed system has to deal with multipath signals in the indoor environment.

To the best of our knowledge, if successful, our proposed system will be the first system that makes GPS signals available indoor using WiFi APs and allows COST GPS receivers to obtain its own location. Specifically, our work has the following research contributions:

- We design a system to relay GPS signal to indoor using COTS Wi-Fi APs. It does not require any modification to existing Wi-Fi's circuit and firmware, and introduce no impact on the AP's communication performance on Wi-Fi domain.
- We present a set of localization algorithms to make GPS receiver localize itself by calculating forwarding distance and angles from relaying hardware to GPS receiver with high accuracy.
- We prototype the proposed hardware in the form of an add-on using OTS RF components (e.g., mixer and diplexer) and SDR implementation.
- We show that the proposed system can localize with an average error of 1.038m in 3D space

and confirm that the proposed system works across different indoor environments.

## 4.2 Proposed System Overview

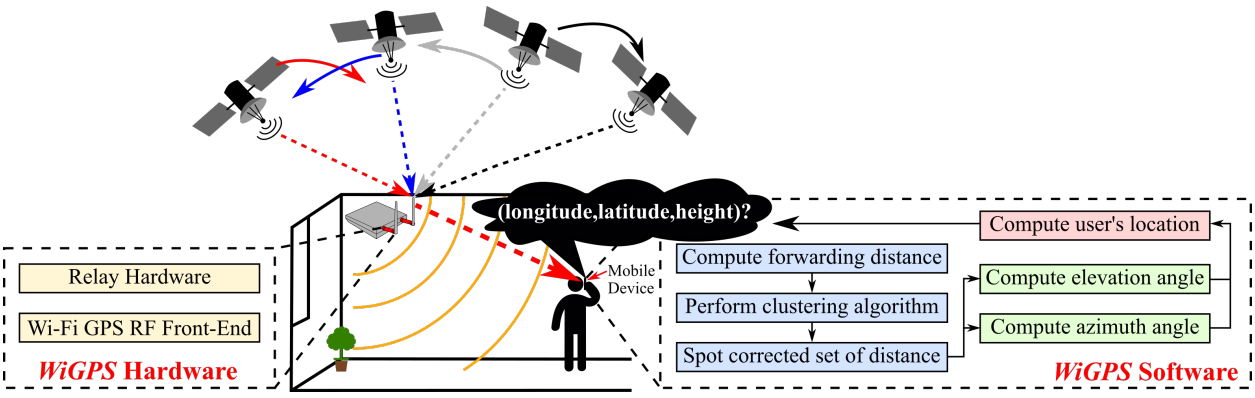


Figure 4.2: Proposed system overview.

The proposed system relies on the fact that Wi-Fi APs are ubiquitous today. Further, it takes advantage of the geographical diversity of these APs, many of which are close to the edge of a building while others are deep inside the building or under the ground. Indeed, it is recommended by Cisco that the Wi-Fi AP should be placed at the edge of buildings to enhance coverage [191, 192]. Let us call these Wi-Fi APs the "*edge APs*". In this system, every *edge AP* receives live GPS signals from the satellites, then amplifies and re-radiates them to its vicinity as illustrated in Fig. 4.1. This new functionality of the Wi-Fi AP is realized by a plug-n-play add-on attached to the AP's antennas. The proposed system makes GPS signals available in indoor environments and leads to the coexistence of GPS and Wi-Fi signals. Once the relayed GPS signals are available indoor, GPS receivers (e.g., mobile phones, tablets, smartwatches, etc.) then perform a sophisicated localization algorithms (§4.4) to localize their location with high accuracy.

The proposed system consists of two main components: (i) a Wi-Fi AP add-on hardware and firmware for controlling the relaying operation and (ii) a set of localization algorithms running on the GPS receiver as illustrated in Fig. 4.2. Attaching the relay add-on hardware into the Wi-Fi AP is very simple as removing the Wi-Fi antennas off the Wi-Fi AP, connecting the relay add-on to

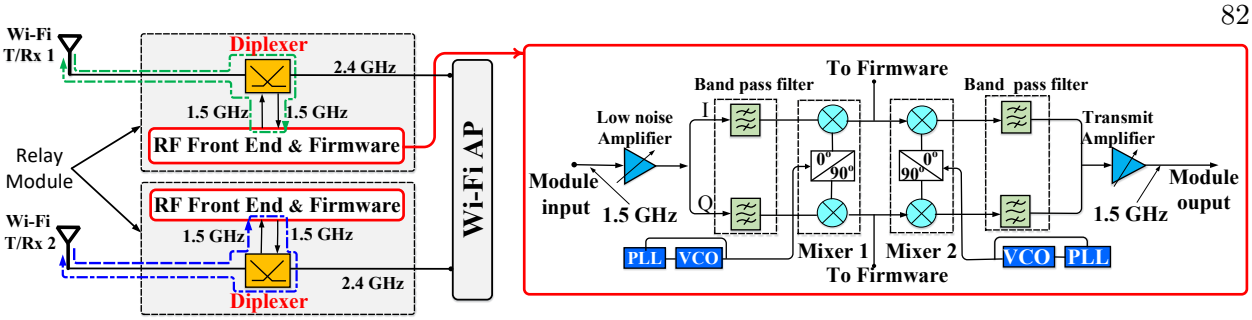


Figure 4.3: The proposed modularized architecture. The proposed relay is co-exist with Wi-Fi AP and does not impact to Wi-Fi communication.

the AP, and re-attaching the antennas to another side of the add-on. The add-on hardware can be powered from a USB port which is available on most of APs these days as a servicing interface. The software running on the receiver contains a set of algorithms to approximate its correct location given the error due to the forwarding delay between the AP and GPS receiver and azimuth and elevation angles from the relay add-on of the AP to the GPS receiver.

## 4.3 The Proposed Add-on Hardware

To realize proposed system, the first step is to design a relay add-on that is able to relay the GPS signals from outdoor to inside the building. The proposed hardware system is designed to operate as a stand-alone device, there is no modification needed on Wi-Fi AP chipset and Wi-Fi AP circuit. The hardware is under plug-n-play form. In addition, we utilize existing RF components (i.e., diplexer) in modern multiband Wi-Fi AP to allow the device to support multiple frequencies the same time with Wi-Fi AP without any interference. The proposed system can be used with most of existing Wi-Fi AP because it requires a small number of antennas to work (2 antennas). We also design the system using modularized architecture so that the add-on can be easily attached or removed from Wi-Fi AP.

■ **No hardware/firmware modification on Wi-Fi AP.** The key observation leading to the ability to make Wi-Fi AP capable of receiving and relaying GPS signals, which is at a completely different frequency, comes from the architectural design of the modern APs. This design is inspired

from a dual-band Wi-Fi design, where the diplexer has been used in the APs to allow that 2.4 GHz and 5 GHz frequency Wi-Fi components are operated at the same time using a single Wi-Fi antenna. We design a *modularized architecture* of relay add-on as follows. Each add-on per antenna contains two or more *Relay module* as shown in Fig. 4.3. The *Relay module* includes a diplexer which is a passive device that implements frequency-domain multiplexing so that it allows the Wi-Fi AP to operate at Wi-Fi and GPS frequencies simultaneously. In particular, we use a COTS diplexer that supports Wi-Fi frequency (2.4/5 GHz) and GPS frequency (L-band frequencies). In addition, a switch controller is used to control whether the Relay module is receiving or forwarding the signal[1] .

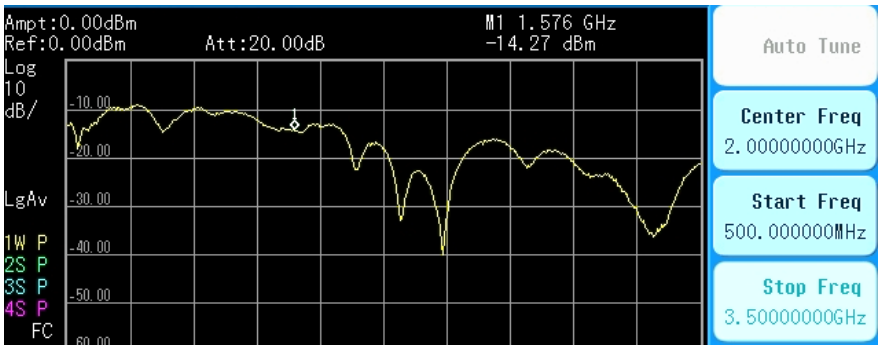


Figure 4.4: Insertion loss of Wi-Fi antenna at GPS frequency.

■ **Utilize Wi-Fi antenna for non Wi-Fi Frequency.** Instead of using a wide-band antenna, we discover that Wi-Fi antenna can also be used to receive and re-radiate a GPS signal due to the high performance of GPS localization algorithm. Note that the GPS signal is desired in a special way so that the GPS receiver still localize its own location even when the GPS signal is under the noise floor level [194]. Therefore, high-gain antenna such as from Wi-Fi AP can be utilized to operate at GPS frequency. To confirm this, we conduct a measurement on multiple Wi-Fi antennas in the lab to observe its behavior. We conduct two step experiments for this study. First of all, we measure the insertion loss of the Wi-Fi AP. We use Agilent N9344C Hand-held Spectrum Analyzer and Altelix 6dB directional coupler for this measurement to identify the insertion loss of the Wi-Fi antennas

[1] Conducting research at GPS frequency may require to obtain experimental license. We obtained an experiment license from FCC as guided in [193].

at GPS frequency (e.g., 1575.42 MHz). We do frequency sweeping in the range from 500MHz to 3.5GHz with 0 dB signal. Fig. 4.4 illustrates the measurement results. We found that the antenna has 14.17 dB insertion loss at GPS frequency. Secondly, we conduct another experiment using software defined radio. Two USRP are used as GPS simulator and GPS receiver. The Wi-Fi AP is attached to these two USRP for validation. From our experiment, we confirm the GPS receiver can capture the signals and decode GPS message at distance up to 50m distance from GPS simulator.

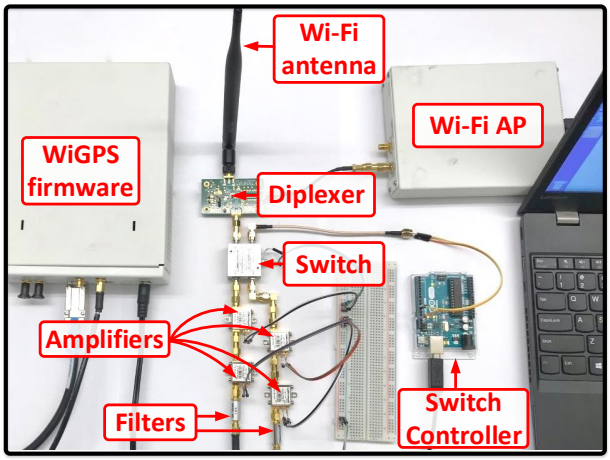


Figure 4.5: The relay add-on prototype which is currently implemented using OTS components. The size will be reduced significantly using PCB fabrication or ASIC design.

■ **The Add-on Architecture.** The detailed architecture of the *Relay module* other than the diplexer is shown in Fig. 4.3 (right). Each relay module is capable of receiving the weak GPS signal captured by Wi-Fi antenna and re-radiating them to an indoor environment after amplification. In particular, the system front-end module receives GPS signals as its input and then those signals are amplified by a Low-noise amplifier. The amplified signal is, in turn, passed through a Band-pass filter to eliminate the environmental noises as well as the Wi-Fi signal at 2.4/5 GHz frequencies. The filtered signals are then down-converted using a mixer and stored into a buffer located in the firmware. After 300 ms, the stored signals can go through up-conversion, another Band-pass filter, and amplification by a power amplifier (PA) for radiating out to the environment. During data collection, the pseudorange is calculated from the time differences between satellites instead of the

absolute value of time difference between satellites and receiver (§9 in [194]). These time difference are obtained from the decoded GPS message (Subframe 1). Therefore, the switching delay between turn on/off does not affect to the pseudorange calculation at *WiGPS* receiver.

■ **The Add-on Prototype.** We chose 2450DM40 A1575E Diplexer from Johanson Technology [195] for our design. This is a low cost diplexer (approx. 1.6 USD) operating at two different frequency bands of 1.574-1.576 GHz and 2.4-2.5 GHz. We used ZX60-V82-S+[196] as Low Noise Amplifier and Power Amplifier at input and output sides of the module. We also used VBF-1575+ Band-pass filter which operates between 1530 MHz and 1620 MHz from Mini-Circuits for both input and output sides. We utilized USRP N210's mixer for down-conversion and up-conversion purposes. The firmware is written in Python and C++ on USRP's platform. The firmware stores recorded GPS signals and send them back to RF front-end before radiating them to the environment. A switch is also controlled by this firmware to alternating the transmit and receive modes. The system prototype is shown in Fig. 4.5. A switch is used to control the transmit-receive behavior of the prototype. The Wi-Fi antenna VERT2450 from Ettus Research is used during our experiments. Note that the size of the proposed system can be minimized to be much smaller than the PCB using ASIC design. Last but not least, the components described above can be adopted depending on the type of Wi-Fi AP, Wi-Fi antennas and supported connectors.

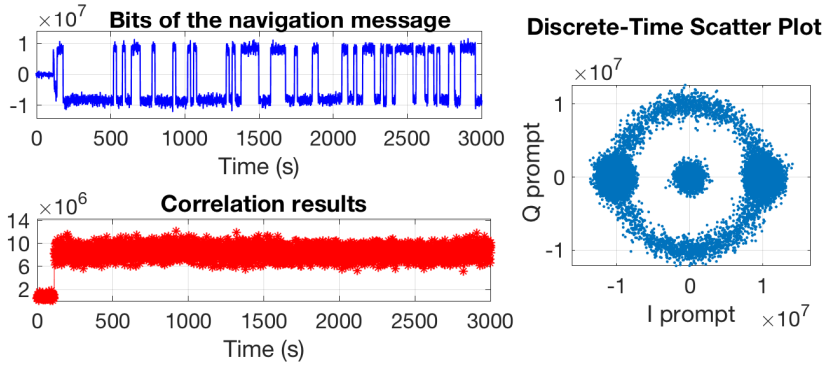


Figure 4.6: Example decoded binary message, correlation results of satellite acquisition, and BPSK constellation of obtained GPS signal.

We then conducted a quick experiment to validate the feasibility and efficiency of our pro-

totype design. For this, we observe the received GPS signal forwarded by the prototype. Fig. 4.6 (left) depicts the decoded GPS message under binary bit sequence and the correlation results of tracking mechanism, while Fig. 4.6 (right) shows the BPSK constellation of the received GPS signal obtained at indoor environment. We confirm that the the proposed design is valid and works properly under the basic test. In §4.6, we will thoroughly evaluate other metrics of the system.

■ **Potential Risks and Solutions.** We are aware that there would be concerns related to the impact on the existing system that use live GPS signal for synchronization. In the scenario where live GPS signal is not available such as underground parking, the devices usually synchronize each other through the internet by associating their clocks with an accurate GPS-based synchronization server to maintain their precise clocks. The forwarded signal will not have impact in this case. In some other settings, the forwarded signal from indoor relay might affects GPS-devices are located outdoor. Thus, we propose the following solutions to overcome problem for this scenario.

1) Shifting the forwarding signal to non-GPS frequency. We propose to shift the frequency of the forwarded signal to make sure that the traditional GPS receiver cannot capture the forwarded GPS signal. In particular, the first direction is to shift to Wi-Fi signal to allow mobile device to listen and decode GPS message at Wi-Fi frequency. The second direction is to create a small shifting in frequency (around 10 MHz). As the forwarded GPS signal frequency is not at the exact GPS frequencies, traditional GPS devices cannot capture and decode forwarded GPS signal. Therefore, there will be no impact to the operation of devices that require live GPS signal for synchronization.

2) The receiver only captures the forwarded signal if it has the software installed. This software on the device will control the central reception frequency to capture the forwarded signal. Without this software, the receiver cannot capture the forwarded GPS signal and cannot perform indoor location sensing. We conducted an experiment of capturing the GPS signal and replay at Wi-Fi frequencies using software defined radio, there are no different when we transmit data at two frequencies. To validate the feasibility of this idea, we conducted an experiment where the relay forwards GPS data to a receiver using Wi-Fi frequencies using software defined radio. We found that there are no significant impact when we forward GPS data at Wi-Fi frequency. We

also conduct other experiments where the carrier frequency is changed to 900 MHz, 1565.42 MHz, 1585.42 MHz, 2000 MHz, 2412 MHz, and 5200 MHz. The receiver is able to capture the GPS data at these frequency without significant reduction in performance. This result is understandable because the proposed localization technique is based on the GPS data (pseudo-range calculation) but not the carrier frequency by which the GPS data is delivered.

We desire the implementation of above solutions to the future investigation. In the experimental validation, we use GPS frequency for validation. Moreover, note that using Wi-Fi infrastructure to relay GPS data to the indoor environment is one of the potential directions to solve indoor localization, other infrastructures can be also utilized to relay the GPS signals to outdoor to indoor. This chapter focuses on the algorithm part of the solution. This algorithm is needed for any relaying hardware (either utilizing Wi-Fi infrastructure or other infrastructure) that relay GPS signals to outdoor to indoor.

## 4.4 The Localization Algorithms

Once GPS signal becomes available indoor by the aforementioned system module, the remaining task is for GPS receiver to localize its position so that the receiver can know its own location, not the AP's. As illustrated in Fig. 4.7, localizing the GPS receiver requires the following: (1) the AP's location, (2) the distance between the AP and receiver, called a "*forwarding distance*" ($\Delta d$), and (3) the difference in horizontal and vertical directions of user's location with respect to the AP, called an "*azimuth angle*" ($\theta$) and "*elevation angle*" ($\beta$), respectively. In the proposed system, localizing the user location is to identify the triple of (longitude, latitude, and height) corresponding to the user's location based on its distance ($\Delta d$) and angles ($\theta$ and $\beta$) from the AP's location.

■ **Localization challenges.** However, our localization task is difficult due to the following limitations:

- *Insufficient number of antennas*: if we have only two RF antennas and an environment where there are more than two significant propagation paths, the MUSIC algorithm [197] cannot calculate either AoA or AoD accurately. Some work on AoA estimation utilizes subcarrier-level

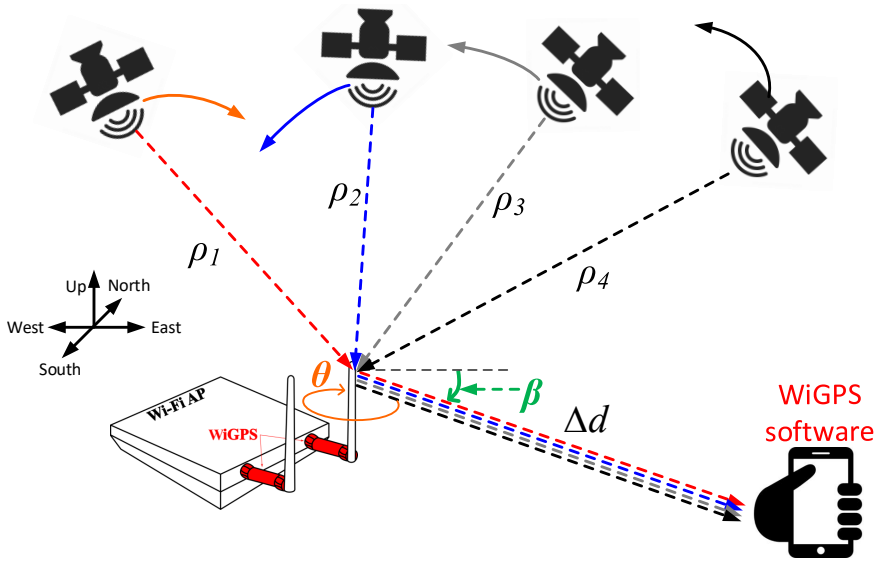


Figure 4.7: The proposed system overview. In order to calculate exact location, the GPS receiver has to calculate WiGPS's location, the forwarding distance, and the angle respecting to the relay's location.

information, e.g. SpotFi [73], which cannot be applied to the GPS signal as it doesn't use OFDM like Wi-Fi.

- *Limited bandwidth of GPS frequency*: the bandwidth of L1 frequency is about 15 MHz. This means that the signal is sampled once every 67 ns, during which it travels 20 m. As such, we can't rely on ToF-based distance calculation. Further, the number of GPS frequency band is limited with one, so we can't apply a frequency hopping technique to emulate wide bandwidth as in ToneTrack [74].
- *Impact by multipath reflections*: GPS signals forwarded from the Wi-Fi AP usually reach the user devices in multiple directions due to reflections. The delay spread generated by multiple paths varies widely. Such a noisy value significantly affects the accuracy of user's localization.
- *No information about Wi-Fi AP's positioning*: when the user device receives the GPS signal from the relaying AP, it needs to calculate its own location without knowing the location of the APs. Most of the existing work assumes that the location of multiple APs is known in advance.
- *No modification of GPS signals allowed*: the user device cannot distinguish whether received

GPS signal is transmitted directly from satellites or relayed by Wi-Fi AP.

■ **Our approach.** Our localization algorithm works in three steps: First, we present a new method that is adapted from traditional GPS localization technique to calculate the Wi-Fi AP's location and the forwarding distance ($\Delta d$) (§4.4.1). Second, we use two relay modules attached to AP's antennas and develop an algorithm that utilizes the signals from these modules for calculating the azimuth angle and refining the forwarding distance calculation (§4.4.2). Third, we form a constrained optimization problem based on the above obtained information (i.e., Wi-Fi AP's location, $\Delta d$, $\theta$) to calculate the elevation angle ($\beta$) as described in (§4.4.3). In addition, we develop the solution for GPS receiver to distinguish the best forwarder in presence of multiple APs equipped with relaying add-ons. (§4.4.4). Finally, we describe algorithms together in §4.4.5.

### 4.4.1 Pseudorange restraint optimization to calculate the forwarding distance

■ **Calculating GPS receiver location from pseudoranges.** The additional forwarding path from the Wi-Fi AP to the user's GPS receiver leads to the inaccurate calculation of user's location. We first review the basic process of traditional GPS calculation to understand why such forwarding path affects the localization performance. The GPS calculation is to identify an unknown location of the user $\mathbf{X}_u = [x_u, y_u, z_u]$ using (at least) four known locations of the satellites $\mathbf{X}_i = [x_i, y_i, z_i]$, where $i = 1:4$.

Every satellite sends its own GPS signal at a certain time $t_{si}$. The receiver will receive the signal at a later time $t_u (t_u > t_{si})$. The distance between the user and the satellite is $\rho_i = c(t_u - t_{si})$, where $c = 2.99 \times 10^8$m/s. If we consider the effect due to clock drift, we have $t'_{si} = t_{si} + \Delta b_i$ where $t'_{si}$ is the actual clock time and $\Delta b_i$ is the satellite clock error, and $t'_u = t_u + b_u$ where $t'_u$ is the actual clock time at user and $b_u$ is the clock bias error of the user device, respectively. The measured distance (i.e., pseudorange) between each satellite and the user, denoted by $\rho_{i=1:4}$, can be derived as $\rho_i = \|\mathbf{X}_i - \mathbf{X}_u\|_2 + b_u, i = 1:4$, since other intrinsic errors can be corrected [194]. For better notation, we also use the $L_k$-norm, which is defined as $\|\mathbf{X}\|_k = (\sum_{i=1}^{n} x_i^k)^{\frac{1}{k}}$ with $k = 1, 2$.

The pseudorange $\rho_i$ needs to be solved simultaneously, and for ease of computation, one of

the solving technique is to linearize them [194]. Here, $\mathbf{X}_u$ are unknown, while $\rho_i, \mathbf{X}_i$ are known. When we perform the differential of the above equation, the result is as follows:

$$\delta\rho_i = \frac{(\mathbf{X}_i - \mathbf{X}_u)\delta\mathbf{X}_u}{\|\mathbf{X}_i - \mathbf{X}_u\|_2} + \delta b_u = \frac{(\mathbf{X}_i - \mathbf{X}_u)\delta\mathbf{X}_u}{\rho_i - b_u} + \delta b_u. \tag{4.1}$$

In the equation, $\delta\mathbf{X}_u = [\delta x_u, \delta y_u, \delta z_u], \delta b_u$ are treated as the only unknown, but $\mathbf{X}_u, b_u$ are treated as known values, because one can assume some initial value for these quantities. From the initial values, a new set of $\delta\mathbf{X}_u, \delta b_u$ can be calculated. Then, these values can be used to modify the original $\mathbf{X}_u$ and $b_u$ values to find another set of solution. The new set of $\mathbf{X}_u, b_u$ now becomes known quantities. This updating process continues until the absolute value of $\delta\mathbf{X}_u, \delta b_u$ becomes very small and is bounded within a predetermined threshold.

More specifically, with $\delta\mathbf{X}_u$ and $\delta b_u$ as unknowns, the above equation becomes a set of linear equations. This equation is referred as linearization.

$$\delta\mathbf{P} = \begin{bmatrix} \mathbf{a}_1 & \mathbf{a}_2 & \mathbf{a}_3 & \mathbb{1} \end{bmatrix} \begin{bmatrix} \delta\ \mathbf{X}_u & \delta b_u \end{bmatrix}^T \tag{4.2}$$

where $\delta\mathbf{P} = [\delta\rho_i]_{n\times 1}$, $\mathbb{1} = [1]_{n\times 1}$, $\mathbf{a}_j = [\alpha_{ij}]_{n\times 1}$ with $\alpha_{i1} = \frac{x_i - x_u}{\rho_i - b_u}; \alpha_{i2} = \frac{y_i - y_u}{\rho_i - b_u}; \alpha_{i3} = \frac{z_i - z_u}{\rho_i - b_u}$, and $n$ is the number of observed satellites. The above equation can be written in a simplified form as: $\delta\mathbf{P} = \mathbf{A}\begin{bmatrix} \delta\mathbf{X}_u & \delta b_u \end{bmatrix}^T$. Since $\mathbf{A}$ is not a square matrix, it cannot be inverted directly. As the above equation is a linear equation, least-squares approach can be used to find the solutions when the number of equations are more than unknowns. Note that from our measurement, we can gather the data from at least more than four satellites. The solution is $\begin{bmatrix} \delta\mathbf{X}_u & \delta b_u \end{bmatrix}^T = [\mathbf{A}^T\mathbf{A}]^{-1}\mathbf{A}^T\delta\mathbf{P}$. In GPS calculation, a quantity is used to determine whether the desired result is reached and this quantity can be defined as: $\varepsilon = \| \begin{bmatrix} \delta\mathbf{X}_u & \delta b_u \end{bmatrix} \|_2$. The iteration will stop either when this value is less than a certain predetermined threshold or when the maximum iteration is reached.

■ **Calculating location and forwarding distance.** In the proposed system, upon receiving the forwarded GPS signals from the relay modules, a GPS receiver performs the following steps to calculate the relay's location and the forwarding distance. Let's assume the obtained pseudorange are $\rho'_{i=1:n}$ ($\rho'_{i=1:n} = \rho_{i=1:n} + \Delta d$) as illustrated in Fig. 4.8 (left). Applying $\rho'_{i=1:n}$ as pseudorange

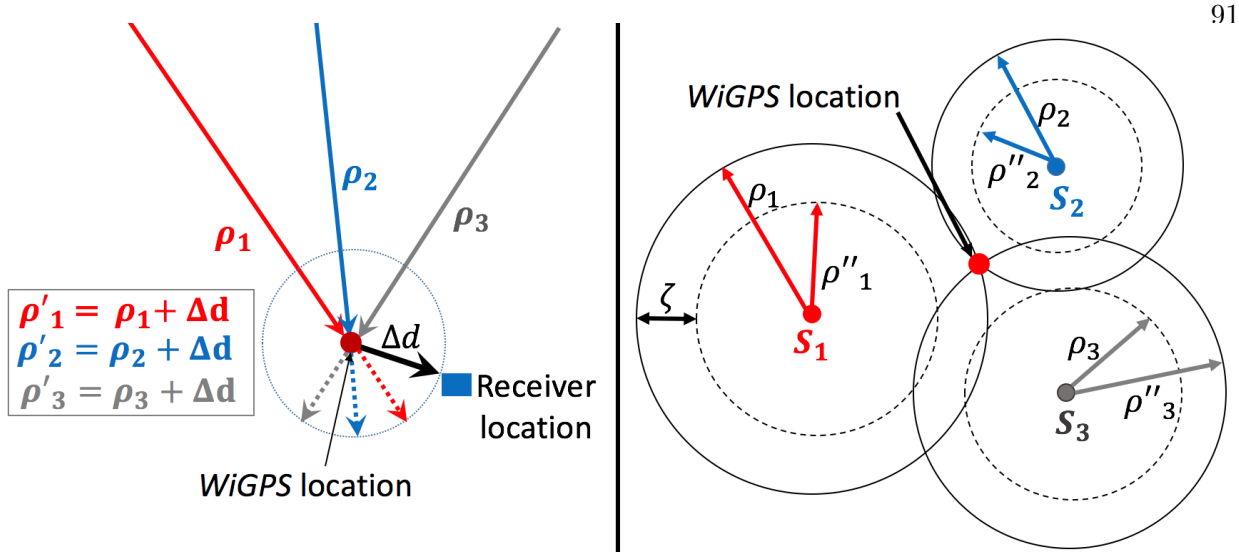


Figure 4.8: Illustration of process of obtaining Wi-Fi AP's location and forwarding distance $\Delta d$.

for (4.2), the condition of $\varepsilon <$ threshold is not satisfied and the calculation is stopped when the maximum number of iteration is reached. After the iteration is stopped, we can call these calculated pseudoranges are "ranges" because of its high accuracy level (i.e., error is at meters). Fortunately, when the calculation is stopped, the calculated pseudorange are representing the distance from satellites $\rightarrow$ Relay $\rightarrow$ GPS receiver. The fixed location would be located on a sphere centered at relay's location. To identify the relay's location, the following procedures are applied. The calculated pseudorange $\rho''_{i=1:n}$ is shorten by a predefined amount ($\zeta$) (i.e., $\rho'' = \rho' - \zeta$). Then, by subsequently applying $\rho''_{i=1:n}$ to (4.2) while reducing $\zeta$, the location fixed condition ($\varepsilon <$ threshold) is obtained when $\rho''_{i=1:n} = \rho_{i=1:n}$ (Fig. 4.8 (right)).

To calculate the forwarding distance, the GPS receiver measures the mean difference between $\rho'$ and $\rho$ from the above steps. The difference represents the length of forwarding distance as illustrated in Fig. 4.8 (left). Hence, the forwarding distance can be obtained from: $\Delta d = \frac{\sum_{i=1}^{n}(\rho'_i - \rho_i)}{n}$. This calculation results in up to 5m of errors. It is challenging to identify the location of the GPS receiver given the errors of measurement from user's location to both antennas of Wi-Fi AP. Next, we will describe our method to reduce the measurement error to around 1m and how to identify

the azimuth angle.

### 4.4.2 Prominence of intersection frequency for uncovering the azimuth angle

Approximating azimuth is impossible with single forwarding antenna due to the lack of direction information. At the receiver location, assuming that the receiver can capture 4 pseudo-ranges from 4 satellites as in Fig. 4.9 (left). Let's assume that the elevation angle is equal to zero, the user location is located at a circle centered at the Wi-Fi AP location with radius $\Delta d$. Finding the azimuth angle is to approximating the horizontal direction of the forwarding signal respecting the two antennas' direction. Such angle can be approximated using angle of arrival or angle of departure [73, 198, 75, 78]. However, these approaches do not apply to this case due to the requirement of multiple antennas and large bandwidth, which are not supported by GPS communication. The receiver observes the signals from two relay add-on, and identifies the azimuth angle based on the distance measured from the two relay add-on. The azimuth angle, named as $\theta$, is calculated based on the difference between distance from two antennas to the user's location. Fig. 4.9 (right) illustrates the relationship between distance different and the angle of arrival from two antennas. Let's assume the distances between receiver's location to antennas 1 and 2 are $d_1$ and $d_2$, respectively.

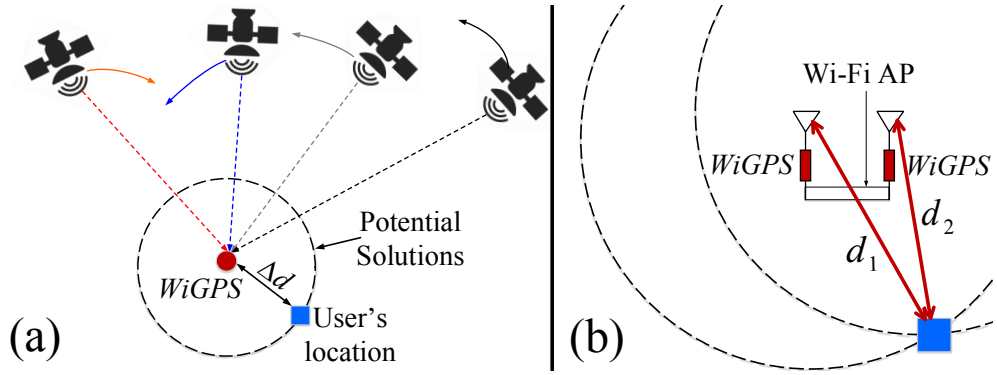


Figure 4.9: Error of approximating azimuth angle using single antenna (a) and Azimuth angle detection approach (b).

■ **Detecting the azimuth angle from the distribution of the Wi-Fi AP intersection fields.** Theoretically, the correct measurements from the two antennas will create two circles

which intersect each other at the user's location. However, it is a non-trivial problem to detect the angle under the noisy measurements. Recall that the error of distance measurement is much larger than the antenna gap needed to estimate the position precisely. Therefore, we deeply explore the distribution of the intersection fields of the two Wi-Fi APs and derive location based on the optimal frequency point. For simplicity, let's assume the transmitter and receiver have the same height, so the elevation angle $\beta$ is equal to zero. The location of Wi-Fi AP antennas are $\mathbf{X}_1^a = [x_1^a, y_1^a, z_1^a]$ and $\mathbf{X}_2^a = [x_2^a, y_2^a, z_2^a]$, respectively, and the user's location is $\mathbf{X}_u = [x_u, y_u, z_u]$, where $z_1^a = z_2^a = 0$. The possible coordination of the receiver can be approximated as the intersection of two circles $\mathfrak{C}_1$ and $\mathfrak{C}_2$ (centered at $\mathbf{X}_1^a$ and $\mathbf{X}_2^a$, and have radius $d_1$, $d_2$). For simplicity, let's omit $z$ in the following derivation. Now, the receiver builds 2D arrays obtained from the above measurements. The corrected measurements should be located at the intersection of two circles $\mathfrak{C}_1$, $\mathfrak{C}_2$. Thus, we have

$$\|\mathbf{X}_u - \mathbf{X}_1^a\|_2^2 = d_1^2, \tag{4.3}$$

$$\|\mathbf{X}_u - \mathbf{X}_2^a\|_2^2 = d_2^2. \tag{4.4}$$

Subtracting (4.4) from (4.3) yields

$$-2(\mathbf{X}_1^a - \mathbf{X}_2^a)\mathbf{X}_u^T = d_1^2 - d_2^2. \tag{4.5}$$

If $x_1^a \neq x_2^a$, then from (4.5), we get

$$x_u = -y_u \frac{2(y_1^a - y_2^a) - (d_1^2 - d_2^2)}{2(x_1^a - x_2^a)}. \tag{4.6}$$

Substituting (4.6) into (4.3) yields

$$sy_u^2 + py_u + q = 0, \tag{4.7}$$

where

$$\begin{aligned}
s &= (x_1^a - x_2^a)^2 + (y_1^a - y_2^a)^2, \\
p &= 2(y_1^a - y_2^a)\left[\frac{(d_1^2 - d_2^2)}{2} + x_1^a(x_1^a - x_2^a)\right] - 2y_1^a(x_1^a - x_2^a)^2, \\
q &= \left[\frac{d_1^2 - d_2^2}{2} + x_1^a(x_1^a - x_2^a)\right]^2 + [(y_1^a)^2 - d_1^2](x_1^a - x_2^a)^2.
\end{aligned}$$

Solving (4.7) for $y_u$, we obtain: $y_u = \frac{-p \pm \sqrt{p^2 - 4sq}}{2s}$. Substituting $y_u$ into (4.6) yields $x_u$. Similarly if $x_1^a = x_2^a$, we solve (4.6) for $y_u$ and substitute $y_u$ into (4.3) or (4.4) to find $x_u$.

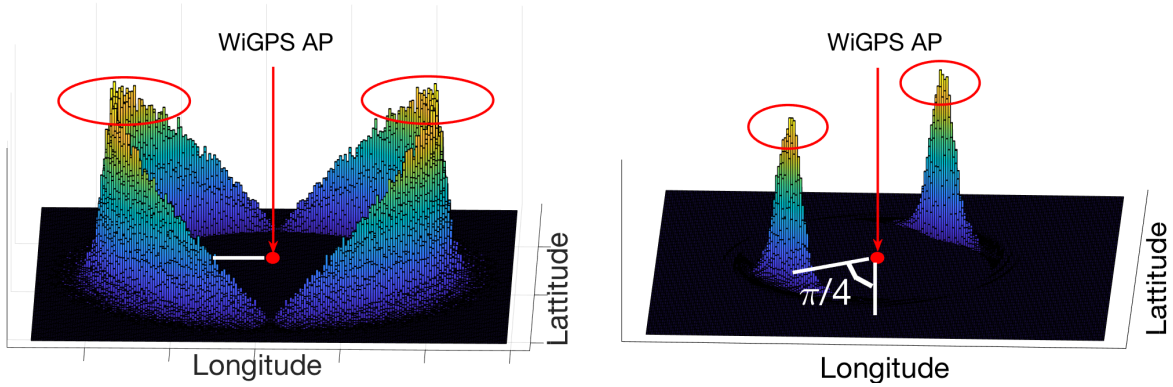


Figure 4.10: Example results for estimating the azimuth angle in case of 0 and $\pi/4$.

The measurement of $d_1$ and $d_2$ is subject to noise with errors in the range of 1.5-5m. In our experiments, $d_1 \gg d_{12}$ and $d_2 \gg d_{12}$ where $d_{12}$ is the distance between the two transmitters. Valid real solutions of (4.3) and (4.4) exist if $d_1$, $d_2$, and $d_{12}$ satisfy the triangle inequality: $|d_2 - d_1| \leq d_{12}$. Any pair of ($d_1$, $d_2$) which fails to meet this inequality is eliminated from our data set. The solutions of (4.3) and (4.4) are rounded to three decimal places. Since $d_1$ and $d_2$ experience a range of measurement noise, the solutions ($x_u$, $y_u$) varies in a large number. We chose a solution which has the highest frequency of presence and considered it our final position of the receiver. Fig. 4.10 illustrates the density distribution of the cross section points for the 0 and $\pi/4$ azimuth angle. The highest peak, corresponding to where the interactions most likely occur, reveals the true position of the receiver. The angle calculation with a two linear antenna array may lead to symmetric ambiguity between 0-$\pi$ and $\pi$-$2\pi$ radians. To resolve the ambiguity, we check the geometric condition between satellites, Wi-Fi AP and GPS receiver: By projecting the coordinate of the observed satellites onto the 2D plane of the AP, we can identify which region most of the satellites are located in from the two regions. Then we can restrict the possible range for the receiver by choosing the other region.

### 4.4.3 Squeezing optimization for computing elevation angle and location

In order to calculate the elevation angle, we exploit the height of each floor (e.g., 3m) in a building. From this information, we can restrict the maximum vertical difference between the Wi-Fi AP and GPS receiver. Further, we can compare this value with the height output from the GPS calculation and choose the minimum as our feasibility set. Then, we formulate a quadratic optimization problem with the output from §4.4.2 and refined height information to search the accurate elevation angle of the GPS receiver with respect to the AP.

Now we describe the above intuition mathematically. Suppose that we have the location of two antennas in Wi-Fi AP ($\mathbf{X}_i^a = [x_i^a, y_i^a, z_i^a], i = 1, 2$) and the distance between each of antenna of the Wi-Fi AP and GPS receiver ($d_{iu}, i = 1, 2$) and the azimuth angle $\theta$ from the Wi-Fi AP to the GPS receiver as calculated in §4.4.2. But, we don't know the 3D location of the GPS receiver $\mathbf{X}_u$ yet. Our objective is to derive the elevation angle $\beta$ from the Wi-Fi AP to the GPS receiver with respect to the horizontal line of the AP[2] as well as the 3D position of the GPS receiver. Since edge Wi-Fi APs are usually deployed at the ceiling inside the building for better coverage, we can assume that the elevation angle $\beta$ ranges between 0 and $\pi$. Further, based on the azimuth angle $\theta$, we can localize the range of the elevation angle: if $0 < \theta < \pi/2$, $0 < \beta < \pi/2$; if $\pi/2 < \theta < \pi$, $\pi/2 < \beta < \pi$. Figure 4.11 illustrates the deployment of Wi-Fi AP equipped with two antennas and GPS receiver. As shown in the figure, we have the following trigonometry relations: $|x_i^a - x_u| = d_{iu} \cos\beta \cos\theta$, $|y_i^a - y_u| = d_{iu} \cos\beta \sin\theta$, and $|z_i^a - z_u| = d_{iu} \sin\beta, i = 1, 2$ and further $z_1^a = z_2^a$. In addition, we can impose the maximum bound on the vertical difference between them by $h$ and the actual vertical difference from both antennas of the AP to the receiver is exactly the same.

Finally, we formulate the following constrained optimization problem to find the elevation angle of the GPS receiver from the Wi-Fi AP. Our objective is to minimize the error for the

[2] Both antennas of the Wi-Fi AP have the same elevation angle toward the GPS receiver.

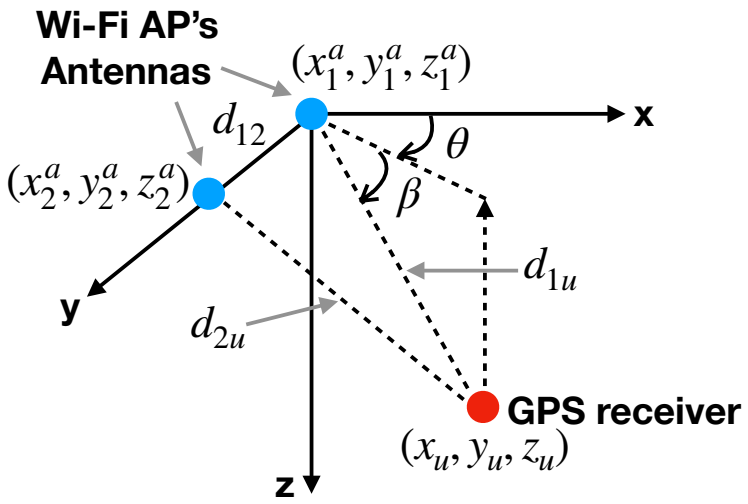


Figure 4.11: Relationship in 3D location between Wi-Fi AP and GPS receiver.

estimated position of the GPS receiver $X_u$ as follows:

$$\begin{aligned}
\min_{\epsilon>0} \quad & \epsilon, \\
\text{s.t.} \quad & \| |\mathbf{X}_i^a - \mathbf{X}_u| - d_{iu}\Gamma \|_1 < \epsilon, \\
& \text{where} \quad \Gamma = [\cos\beta\cos\theta, \cos\beta\sin\theta, \sin\beta], \\
& \|\mathbf{X}_i^a - \mathbf{X}_u\|_2 = d_{iu}, i = 1, 2, \\
& \|\mathbf{X}_1^a - \mathbf{X}_2^a\|_2 = d_{12}, \\
& |z_1^a - z_u| = |z_2^a - z_u| < h, 0 < \beta < \pi.
\end{aligned} \tag{4.8}$$

From the above formulation, we optimize for the position of the GPS receiver while maintaining the relative distance relationship between each antenna of Wi-Fi AP and GPS receiver and the trigonometric relationship between Wi-Fi AP and GPS receiver. We write this problem as a quadratic-constrained optimization in Matlab and use the fmincon function to find the optimal solution. We evaluate its computational complexity in §4.6.

### 4.4.4 Receiving signals from multiple forwarding add-on

■ **Mitigating the relay signal outliers.** In practice, WiGPS receiver often receives signals from the unknown number of WiGPS relay modules. To handle the case, we apply a clustering algorithm

associated with a predefined number of centroids. The number is based on the measurement distribution in order to group the measured forwarding distances into multiple clusters. We then use the cluster that includes the shortest forwarding distance for localization. Specifically, these distances are used to approximate the azimuth and elevation angles from the forwarding AP using the algorithm mentioned in §4.4.2 and §4.4.3, respectively. This is one of the key advantages in using GPS signal to localize the user location.

Suppose that there are $k$ Wi-Fi APs placed at different ranges toward the receiver. Note that the calculation of forwarding distance still results in quite a few errors. This leads to a lot of false detection in detecting the proper pairs of forwarding distances. Thus, to eliminate the outliers, we apply the k-means clustering [199], which is one of the representative clustering algorithms, into the distance cluster. However, the value of $k$ associated with the number of interfered Wi-Fi APs is unknown. Therefore, we are unable to run the algorithm due to the missing value of $k$. Fortunately, according to the kernel density estimation, the data distribution exposes some local maxima corresponding to our forwarding distances. Hence, we can determine the number of clusters among these local maximum points, except the locations where the data frequency is extremely small ($< 0.1\%$ of the total data). However, the k-means clustering randomly initializes the centroids, which results in the uncertainty of clustered data. To tackle this problem, we adopt the centroids detected from the kernel density to initialize the k-centres in the clustering algorithm.

### 4.4.5 Putting together

Algorithm 6 shows how the proposed localization algorithm works. Specifically, when RSSI of GPS signal is under noise floor level, the GPS receiver cannot recognize any forwarding relaying signal so that it performs traditional GPS calculation to localize its location. Otherwise, the forwarding signal can be detected when the received RSSI is over the noise floor (-100 dB). Note that as satellites are 21,000 km away from the earth surface, their signal is always lower than the noise floor level (e.g., -111dBm) [194]. Next, when there is single forwarding signal obtained, the proposed algorithm will compute the forwarding distance and the azimuth and elevation angles

before computing its location. On the other hand, when the GPS receiver captures the signal from multiple relaying APs, it first computes and clusters the forwarding distances into multiple subsets and then selects the set that has the smallest value. Finally, it uses them to compute both angles for localization.

**Algorithm 6:** *WiGPS*'s localization algorithm

**input :** $RSSI$/* Received GPS signal strength */
$G_m$ /* Decoded GPS message */
$\gamma$ /* Forwarding signal detection threshold */
$\eta$ /* Multi-AP signal detection threshold */
**output:** $U(lat, lon, height)$ /* User's location */

**if** $(RSSI < \gamma)$ **then**
  Compute $U(lat, lon, height)$ based on $G_m$
**else if** $(\gamma < RSSI)\&(Std[RSSI] < \eta)$ **then**
  /* Received signal from single *WiGPS* AP */
  Compute $\Delta d$ (Forwarding distance), $\theta$ (azimuth angle),
  and $\beta$ (elevation angle)
  Compute $U(lat, lon, height)$
**else if** $(\gamma < RSSI)\&(Std[RSSI] > \eta)$ **then**
  /* Received signal from multiple *WiGPS* APs */
  Compute $\Delta d$
  Perform clustering algorithm and spot corrected set of $\Delta d$
  Compute $\theta$ (azimuth angle), and $\beta$ (elevation angle)
  Compute $U(lat, lon, height)$
**return** $U(lat, lon, height)$

## 4.5 Software Implementation

The software receiver is implemented on USRP N210 [200]. The calculation of pseudorange and forwarding distance is adopted from GNSS-SDR implementation [201] whose implementation is done with Python and C++. The receiver is sampled at 20 MHz and capture the GPS signal at L1 frequency (1575.42 MHz). As explained in [202], we set to search up to 10 channels (i.e., 10 satellites) at the same time, which is a common setting in today's smartphones. We collected the following information from the received GPS signals: (1) The raw I and Q signals after down-conversion to baseband, (2) The tracking quality of observable satellites, (3) the pseudorange measurements, and (4) the observed Navigation RINEX files. Note that the Receiver Independent Exchange Format is

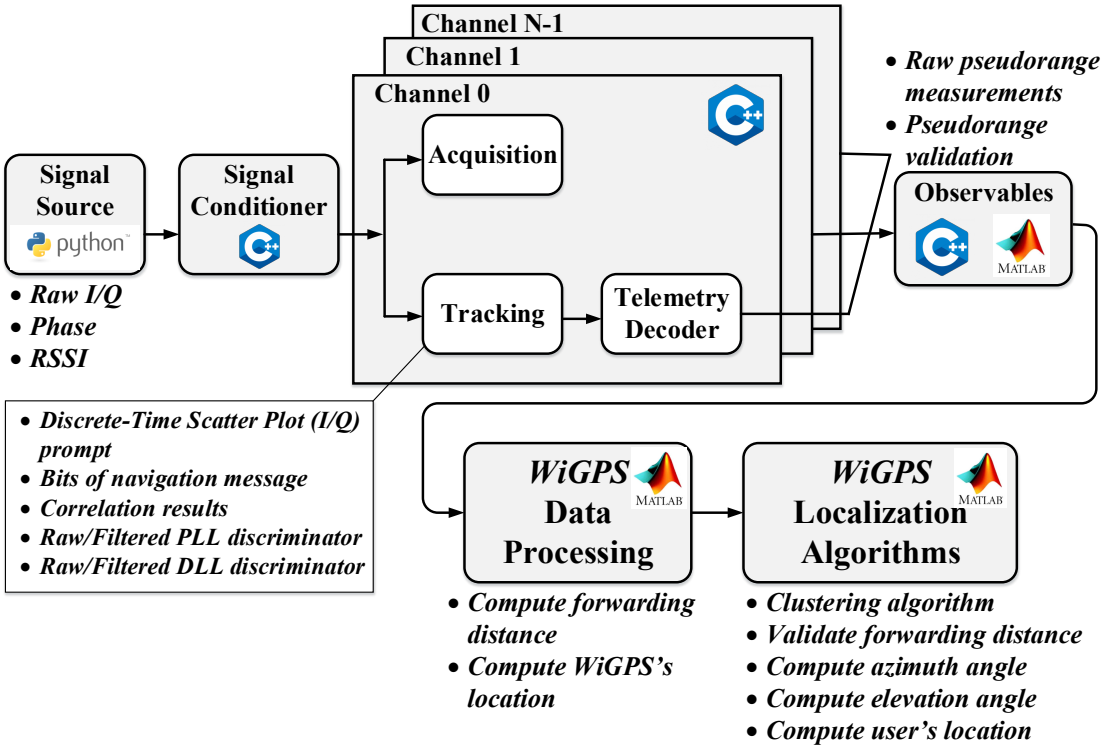


Figure 4.12: Software calculation flows. GPS receiver is currently implemented using python, C++, and Matlab.

a standard data format for raw satellite navigation system containing position, speed of satellites. The I and Q signals are used to validate the phase and RSS of the obtained forwarded GPS signals. In particular, the tracking component provides (a) Discrete-Time Scatter Plot (I/Q prompt), (b) Bits of navigation message, (c) Correlation results, (d) Raw/Filtered PLL discriminator, and (e) Raw/Filtered DLL discriminator. The pseudorange measurements provide a real-time calculation of the distance from the satellite to the receiver. Last but not least, the observed Navigation RINEX in .geojson files includes calculated the relay location and forwarding distance to GPS receiver. The aforementioned collected output is fed into Matlab for further processing of calculating forwarding distance as well as obtaining forwarding angles. The whole system is implemented on a laptop with a 2.0 GHz i7 CPU and 8 GB memory.

## 4.6 Performance Validation

We prototyped our system to evaluate the feasibility and performance of WiGPS, and also measure the performance overhead that WiGPS could cause to legacy Wi-Fi APs. In particular, we conduct implementation and evaluation to answer the following questions: (1) *How accurate is the proposed system in indoor localization*? (2) *How does the proposed system impact legacy Wi-Fi communication*? (3) *What are the accuracies of calculating forwarding distance, azimuth, and elevation angle*? (4) *What are the impacts of different environments on localization accuracy?* (5) *What is the accuracy of localization when the proposed receiver receives signals from multiple relays?* The following subsections provides the answers for each question above.

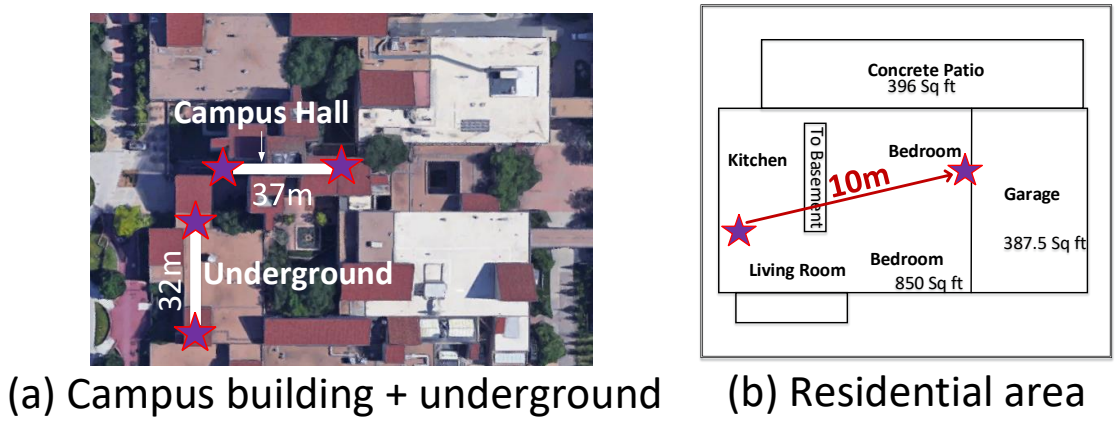


Figure 4.13: Locations where experiments were conducted.

### 4.6.1 Experimental Methodology

For ground-truth, we use Google Maps [203] to obtain geographic longitude, latitude for Wi-Fi AP and GPS receiver. Instead of using Google Maps, one can record the outdoor location using live GPS and then measure from that point to the testing location inside the building. However, This method cannot be realized in the underground scenario. Also, the GPS receiver will have less accuracy when it is close to the building due to multipath reflections [204]. To obtain the correct distance and angle between the forwarding AP and receiver, we use the BOSCH GLM 80 laser distance measurer [205] to accurately find the distance and angle from the forwarding AP to

user's location. We validate the performance of the proposed system at three main environments including campus hall, underground, and residential areas.

### 4.6.2 Priliminarty Results

■ **Localization Accuracy.** We first validate localization accuracy when GPS receiver is 10m, 20m, and 30m away from *WiGPS* add-on on a horizontal direction (0° elevation), at 0, 45, 90° azimuth, and at 0, 10, 20, 30° elevation at our campus hall, underground, and residential areas. Note that the coverage by a single AP is usually less than 30m [206, 73, 85] and further, the area beyond 30m can be covered by another AP especially in the large area of a building [191]. Therefore, we select 30m as a maximum distance for testing the proposed system.

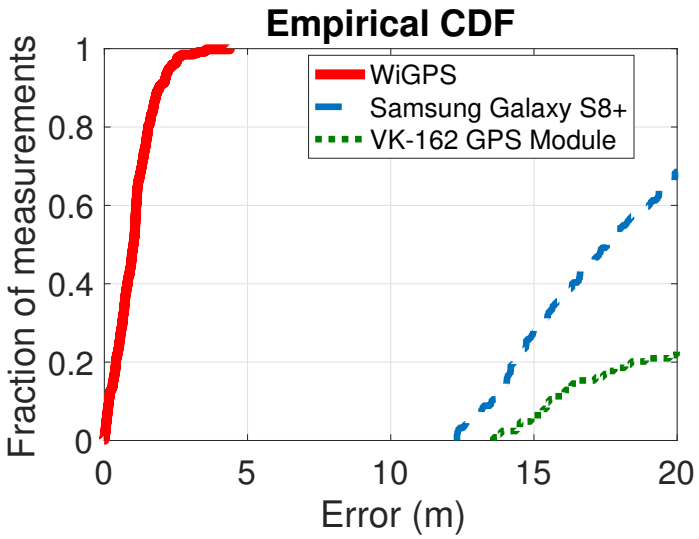


Figure 4.14: 3D Localization Accuracy

For comparison with the proposed system, we use Samsung Galaxy S8+ (GPS Logger App [207]) and VK-162 GPS Module, which uses Ulox UBX-G7020 series chipset [208]. Fig. 4.14 shows the CDF of the accuracy of localization using the proposed technique. The proposed system obtains a median error of 1.038 m. To calculate the forwarding distance, the azimuth angle, and elevation angle, 1000 data samples from two antennas to receiver are used in our localization algorithm. As the GPS receiver can see an enough number of channels (i.e., satellites) via the

relay add-ons, it can localize their locations with high accuracy. The performance gap between the proposed system and others is mainly due to the number of observable satellites: the former can decode an enough number of channels (more than seven satellites during the whole experimentation), while the latter only sees a small number of channels (quite often less than four). In addition, our statistic-based localization technique contributes the accuracy improvement. Note that the GPS receiver without relaying support shows similar performance with VK-162 GPS Module.

■ **Interference to Wi-Fi communications.** We validate the impact of the proposed system to Wi-Fi communication by observing the Wi-Fi throughput with and without attaching the proposed system hardware to NUC platform (Wi-Fi AP mode). In particular, we set up one NUC platform as a Wi-Fi AP using hostapd [209] and connect a Samsung Galaxy S5 phone as a Wi-Fi client to the AP. For Wi-Fi, we choose 2412 MHz to minimize interference from other Wi-Fi transmissions and use a TCP flow by running iperf [210], while for the proposed system, the add-on device is connected in between the AP and Wi-Fi antenna through Multilayer Diplexer, which operates at 1572-1578 MHz and 2400-2500 MHz[3]

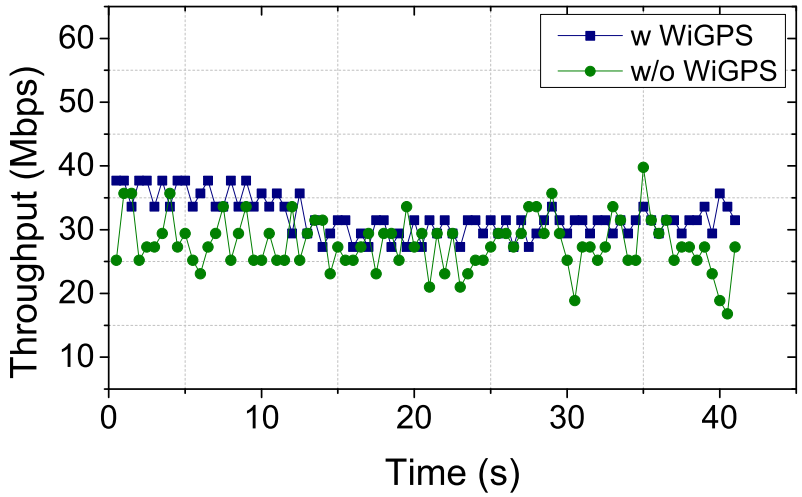


Figure 4.15: Impact to Wi-Fi

Then, we measure the instantaneous throughput achieved by the TCP flow with and without

[3] This was conducted on 2.4 GHz due to limitation of our diplexer. However, a similar experiment can be conducted with other Wi-Fi frequency, e.g., 5 GHz, by selecting other diplexers which support that frequency.

GPS signal relaying. As shown in Fig. 4.15, we observe that the proposed system does not impose any interference on Wi-Fi communications. In fact, we found that the system throughput is more stable when attaching the proposed system. We believe that this is due to the effect of the current wide-band amplifier used (ZX60-V82-S+). As it is a high dynamic range amplifier supporting the whole bandwidth between 20 MHz and 6 GHz, the proposed system leads to the increasing power of Wi-Fi signal at 2.4 GHz. However, this phenomenon can be totally removed by selecting a narrower band amplifier in the future.

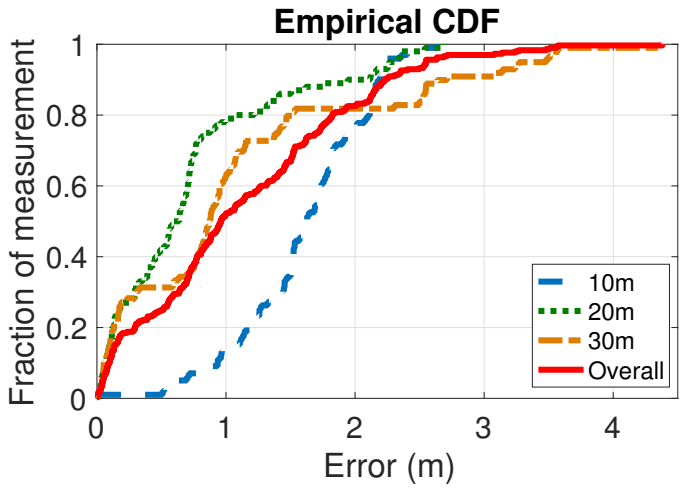


Figure 4.16: Distance Calculation Accuracy

■ **Accuracy of calculating forwarding distance.** We collected about 450 minute-long data of received forwarded GPS signals when the distance from the relay to GPS receiver is 10m, 20m, and 30m. The distance between the relay and GPS receiver is obtained from BOSCH GLM laser device. Our experiment is conducted at the campus hall inside our university. Fig. 4.16 shows the CDF of estimation error obtained by the proposed system. The proposed technique obtains a median of 1.6m error at 10m distance, 0.6m error at 20m distance, and 0.8m error at 30m distance. The system obtains a median of 1.1m of error overall. We found that the performance of localizing at 10m is lower than 30m. We believe that this is due to multipath effects. At the shorter distance, the reflected signal is strong enough to affect the performance. But, as the the distance is further, the RSS from some reflected paths will be reduced and some paths experiencing severe attenuation

(< 20dB) will not affect the GPS receiver [211].

■ **Accuracy of calculating azimuth angle.** For evaluation of azimuth angle detection, we conducted another experiment where the relay is 20m away from the GPS receiver, and the angle created by two antennas AP and the receiver creates an angle of 0, 45°, and 90°. We collected 450 minutes of data for each angle. Fig. 4.17 shows the accuracy of estimating the azimuth angle using the proposed technique. The proposed system obtains 2°, 6.9°, and 7.8° error when azimuth angle is 45°, 90°, and 0°, respectively.

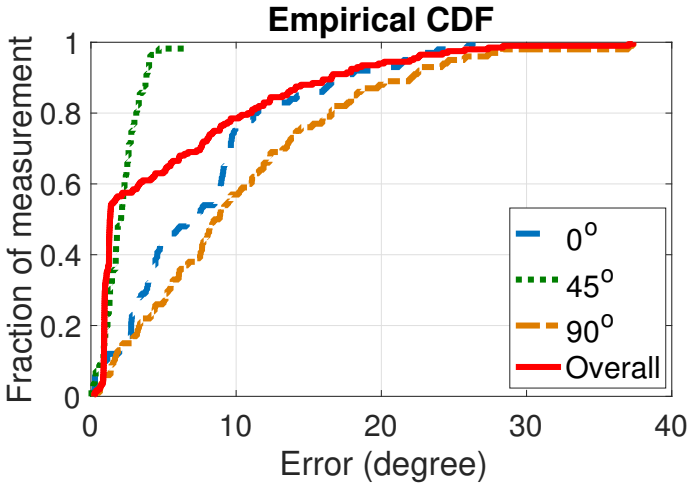


Figure 4.17: Azimuth Angle Calculation Accuracy

Overall, the system obtains less than a median of 2.9° in azimuth angle calculation. We believe the proposed system achieves the best performance when the azimuth angle is 45° due to the impact of environment architecture. In addition, as data from different angles are collected at different times, the satellites will also impact the result. Hence, more investigation is needed to understand the scenario.

■ **Accuracy of calculating elevation angle.** To evaluate the performance of *WiGPS* on detecting the elevation angle, we conducted an experiment in the first floor of a multi-story building at our campus. In this experiment, the *WiGPS* AP is hanged on the ceiling on a 1-floor building, we change the angle $\beta$ from 10° to 30°. As the standard ceiling height is only around 2.5m, we do not conduct the experiment with an angle larger than 40° because the longitude and latitude

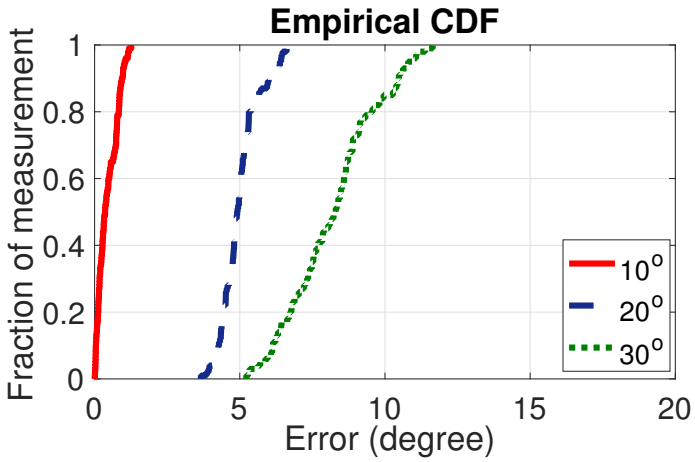


Figure 4.18: Elevation Angle Calculation Accuracy

different between *WiGPS* and GPS receiver is very small. We collected 100 minutes of data in total for this experiments. Fig. 4.18 shows the CDF of elevation detection accuracy of *WiGPS*. The system obtains very accurate calculation with less than 1° error. *WiGPS* obtains less than 0.5° in calculating elevation angle when the GPS receiver is 10° respecting the ceiling. When the elevation angle is 20° and 30°, *WiGPS* obtains 4.9° error and 8° error in calculation, respectively. When elevation angle is bigger, the distance to *WiGPS* is shorter, and multipath effect is stronger, the localization accuracy reduced.

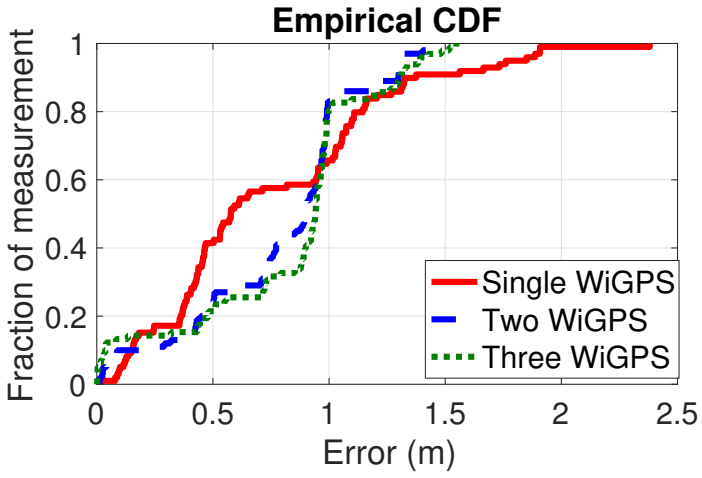


Figure 4.19: Impact of Multiple *WiGPS*

■ **Receiving signal from multiple *WiGPS*.** We evaluated the scenario where GPS receiver

receives signals from multiple *WiGPS* APs at the same time. The GPS receiver is 10m, 20m, and 30m away from three *WiGPS*. WiGPS algorithm will allow the GPS receiver to identify the correct set of forwarding distance and therefore calculate its location. Fig. 4.19 shows the performance of *WiGPS* when GPS receiver received multiple signals. As can be seen from the Figure, when using single *WiGPS*, the average accuracy is higher than when there are multiple *WiGPS* in the environment because the outlier of distance measurement are partially refined during clustering process. Also, the maximum error obtained from multiple *WiGPS* scenarios is lower than with single *WiGPS*. The reason is that the clustering algorithm actually helps to remove a lot of outliers during forwarding and angles calculations.

■ **Computational Delay.** For cost analysis, we validate the computation time taken by *WiGPS* software. Even though the existing algorithm is developed in Matlab, the results presented here can be used for future developers to understand the computation cost needed to run WiGPS. However, we believe that this high computation delay can be solved using by offloading the algorithm to the cloud. As the delay of computation depends on the number of measurements that the receiver used to find its location and angle, we calculate the delay of computation with different data sizes of the measurements. The results are shown in Fig. 4.20. When including the time that the system needs to have to calculate the Wi-Fi AP's location, the total time is less than 4 minutes (Fig. 4.21). It is noticeable that the system requires less than 5 minutes to calculate the calculation. With a better receiver, we believe that the computational cost is significantly reduced.

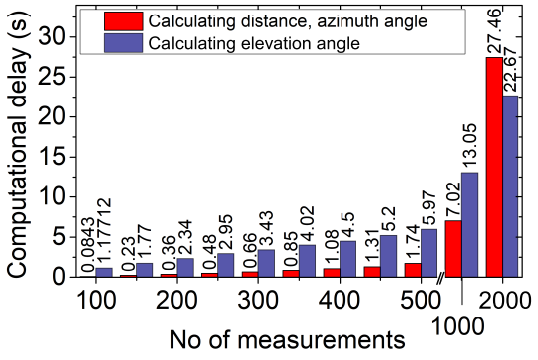


Figure 4.20: Computation delay

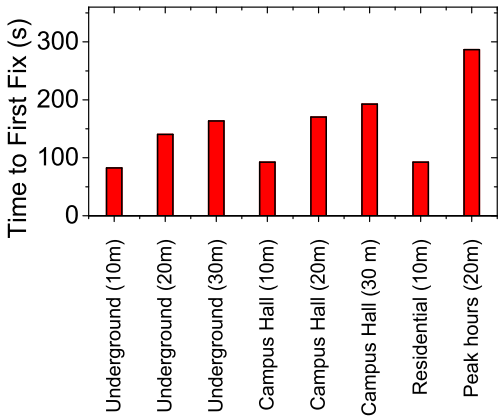


Figure 4.21: Time to first fix

### 4.6.3 Sensitivity Analysis

■ **Impact of Environments**. As mentioned earlier, we also evaluated the system at the underground environment and residential area. Our intention is to validate the system performance at different environment setups to validate where WiGPS works at different architecture and materials. At underground environment, the WiGPS and GPS receiver is 10m, 20m, and 30m away from each other. Comparing to WiGPS performance at the campus hall, WiGPS obtains better performance at underground area due to the reduction of live GPS signal to its computation. At residential area, the experiment is collected at a concrete wall single house 1700 sq ft, the GPS receiver is 10m away from WiGPS and separated by a drywall. As illustrated in Figs. 4.22 and 4.23, *WiGPS* obtains reasonable localization error at both of these environments.

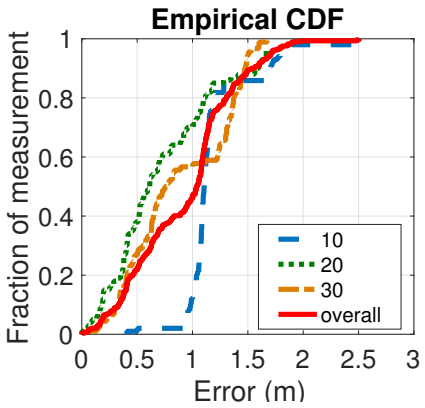


Figure 4.22: Localization accuracy at underground area

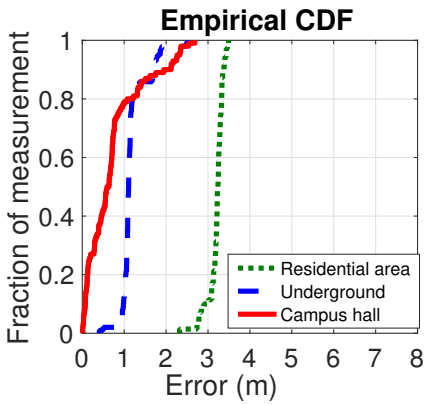


Figure 4.23: Localization accuracy at residential area

■ **Impact of Human Movement.** Human movement has a large impact in time-to-first-fix (TTFF) as illustrated in Fig. 4.21 because the distortion caused by human movement will reduce the efficiency of decoding correct GPS message for localization. We conducted an experiment during peak hours (school breaking time between classes) to validate the efficiency of *WiGPS* performance. We collected 60-minute data throughout this experiment. Fig. 4.24 illustrate the performance of *WiGPS* during these peak hours compared with off-peak hours (e.g., night times). *WiGPS* obtains around 1.3 m error in localization even in peak hours.

■ **Impact of Number of Measurements.** We validate the impact of number of measurements for estimating the forwarding distance and angles. Fig. 4.25 shows the accuracy trend by varying the number of measurements used for calculation. We found that *WiGPS* can achieve good performance when the number of measurements are greater than 500. In other words, with this number of data samples, our azimuth angle detection algorithm can provide high accuracy.

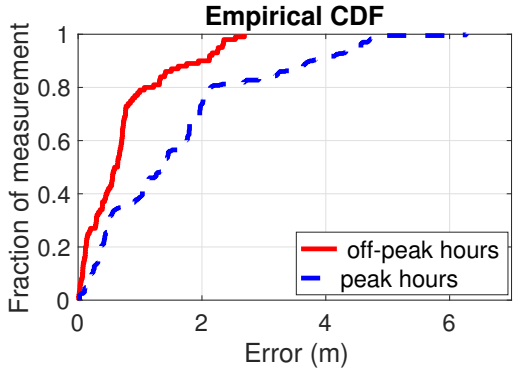


Figure 4.24: Impact of human movement to localization accuracy

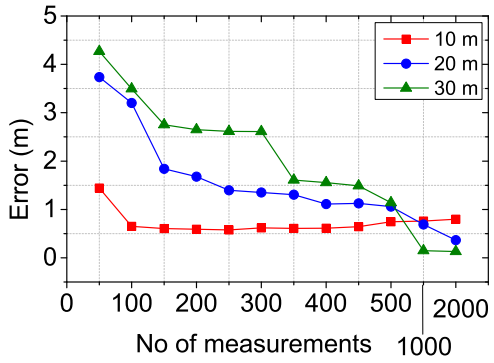


Figure 4.25: Impact of number of measurements

## 4.7 Conclusion

In this chapter, we have presented a novel system to relay GPS signals via Wi-Fi APs from outdoor to indoor for GPS-based indoor localization. For verification, we implemented the proposed system's prototype using OTS RF components and SDR implementation. Through extensive experiments, we confirmed that the proposed technique provides 1.038m of 3D localization accuracy and does not impact existing Wi-Fi communications. We also demonstrated that the proposed technique works across multiple indoor environments including university campus, underground, and residential areas. Through there are many more aspects of the proposed technique warranting further investigations, we hope to this work will trailblaze a new path towards solving the indoor localization problem by bring GPS signals to indoor environments using existing Wi-Fi APs.

## 4.8 Looking forward

Our system has focused on how to make the GPS signal available indoor and enable GPS receiver to accurately localize its own location. This paper may be viewed as a first step toward this goal. Several extensions and enhancements remain open for future work. First of all, we wish to explore a new method to improve the accuracy of receiver to reduce the localization error and time to first fix. Second, our work utilizes on the relative height between the Wi-Fi AP and receiver for 3D localization. Even though the GPS can offer the altitude value, the inaccuracy is still a bit high compared to the longitude and latitude. However, we expect that as the accuracy of GPS will be improved in the near future [212], the proposed technique can provide geographic coordinate values in 3D very accurately. Third, we would like to miniaturize the current hardware by revising PCB design and then designing ASIC circuit. Fourth, while system is currently implemented on SDR, we wish to implement it on a smartphones as done in [204]. Given raw GNSS measurement that is currently supported by Android [213], we can utilize this API to override the positioning result obtained from the proposed algorithms. Any location-based applications can easily incorporate this library to obtain high accuracy of the proposed technique. Fifth, our current prototype is quite expensive, but its PCB prototype will cost less than 30 USD. We believe that if the system is mass produced, the price should be significantly reduced. Last but not least, we also wish to investigate multihop scenarios in the future.

# Chapter 5

# Conclusions

## 5.1 Concluding Remarks

RF signals and devices are not only used for communication, but can also be used to monitor human, objects, and location for monitoring user's health condition, and enhancing user privacy and safety protections. This dissertation introduces new algorithms and cyber-physical systems that use RF signals to extend their usability in multiple directions. The presented technologies demonstrate that we can build many novel applications utilizing RF signals to sense human breathing volume, the drone body shifting and vibration. I also describe the feasibility of using RF signal to sense the global locations at indoor environments.

**Summary of Contributions:** The contributions of our research can be summarized as following. In contrast to traditional approaches which required instrumenting the human body with sensors, our research does not require any physical contact with the human body. We present a closed loop sensing system for health-care monitoring which can highly adapt to the dynamic of human sensing scenario. The mechanical scanning component navigates and directs the Wi-Fi beam to steer to the human chest and keep track of its movements. We also present a technique to extract the chest movements and use it to infer the breathing volume. Such correlation is unknown earlier. We evaluate the system on real patients and validate that the system obtaining high accuracy in monitoring. We propose a technique to passively and cost-effectively detect the presence of the drone. As the number of incidents involving drone such as drone collisions, damage to properties, and violations of privacy are increased, the proposed system help to reduce such unexpected scenarios.

We evaluated the system at different distances, environments using different drones. The system obtains high performance at all tested scenarios. In addition, we present a feasibility of sensing the user's location at the indoor environment. If successfully, the proposed technique can also be used for a wide range of global-location-based services and applications. From the preliminary study, the system obtains high performance at distance up to 30 m.

## 5.2 Future Works

We have only presented some small set of possible applications that could leverage RF signals. While this dissertation has taken a first step in making the implemented systems practical, the presented designs and implementation include some limitation which would be interesting to explore in the future. In this section, we would like to discuss some future research that can be enabled from the developed systems.

■ **Sensing human breathing volume using RF signals.** First, we need to improve the user experiences in using the radar system by removing the noises created by the mechanical components of the system. Although the previous implementation of the system does not require the user to wear any extra device, it still generates some noises that effect to human sleep during experiments. We are going to build a bed dome and deploying 30 antennas to remove the need for mechanical scanning procedure. The 30 antennas are distributed around the bed dome to keep track different area of the chest regardless of current human posture. The system has control on each antenna to decide which antenna acts as a transmitter which antenna acts as a receiver. Second, we are developing techniques to detect sleep apnea events. As the antennas are placed across different areas on the bed dome, each of them monitors a certain area on the human body continuously, we can analyze the breathing behaviors at different areas at the same time to detect the sleep apnea events. There are two kinds of sleep apnea that we are investigating including (a) central apnea and (b) obstructive apnea. The synchronization in the phase of the breathing patterns captured at the chest and abdominal areas are used to detect sleep apnea. Third, we are developing an RF imaging algorithm to detect human posture and to remove the need for training in posture

detection in the occlusion condition. This step is important for maintaining the high performance of the breathing volume estimation. Note that we have been investigated on multiple vision and thermal based techniques to overcome this challenge, but these techniques can only recognize a fixed set of trained postures. We are developing an imaging technique based on Radar Polarimetry to accurately identifying the human posture, therefore adjusting the transmitter and receiver to a proper location and direction.

We continue to work on both RF and camera technologies for improving the accuracy of the breathing volume estimation as well as reduce the side-effects (unexpected acoustic noises) of the system to human sleep quality. The new design makes the system operations are completely silent because there is no mechanical component needed. To monitor the chest movement accurately, a high resolution in controlling the transmitted and received signal is required. We are developing a system of 30 wireless transceivers. Each of the antennae can be a transmitter or receiver. Using this approach, we are a free-doom in monitoring the movements of the human chest in different areas at the same time regardless of the human posture. Even though the system is still under development, the control mechanism of switching between the transmitter to the receiver is quite challenging. We are still seeking for the best deployment and controlling mechanism to obtain the maximum accuracy in breathing volume estimation, sleep apnea detection, and human posture detection.

We will utilize the dome bed design with multiple antenna transceiver arrays to detect sleep apnea problem. The key idea is to use antenna array to track different areas on the human chest surface (e.g., upper chest area and abdominal area) at the same time. The chest movements obtained from the two set antennas would help to detect sleep obstructive apnea problem where the movements in different areas are not synchronized with each other. In addition, we continue to optimize our vision techniques to improve the breathing volume monitoring algorithm and posture estimation using depth and thermal cameras. The breathing volume monitoring algorithm will corporate with the new antenna array to detect sleep apnea. We are analyzing the correlation between the actual inhale/exhale air captured by the camera and the movement of the human

chest and abdominal area captured by the antenna array. The abnormal events observed from camera and antenna array will be used as a signature (biomarkers) to detect sleep apnea event. Next, to reduce the cost of expensive CO2 and thermal camera, we are investigating on a novel and efficient computational vision technique by placing a cheap material in front of the human face (e.g. paper) to allow the low-cost camera to detect the inhale and exhale airs.

We will also develop an RF imaging algorithm to detect the human posture using purely wireless signals. The key idea is to differentiate the signal reflected from the human body and the bed to build the 3D image of the human body. This is very challenging due to the unpredictable reflection characteristics of different materials (i.e., human, bed, floor, etc.). To overcome this challenge, we are using at Radar Polarimetry approach to differentiate different materials based on the characteristics of the received signals. Radar Polarimetry is a well-known technique in radar imaging technology. RADAR systems use synthetic aperture radar polarimetry for topography imaging. Aircraft and satellites can even use polarization of received RADAR signals to measure soil moisture of farmland. By measuring the polarization and power of the received waves, we can distinguish objects based on texture and material (metallic or otherwise). We place a metal piece underneath the bed. The signal transmitted by the transmitter will traverse the medium, hit the human and the metal pieces and reflected off. The reflected signals are then captured by our RF receivers. The key idea here is to amplify the difference in reflection signals caused by the human body and the metal pieces to identify the human posture.

■ **Sensing drones presence by identifying their signatures from RF signals.** We have demonstrated the feasibility of sensing objects (i.e., drone) using Wi-Fi signal emitted from the devices. We are investigating the following research directions.

We have focused on detecting the presence of drones through their unique inherent physical movement signatures on Wi-Fi domain. This system can be expanded to consider a wider variety of drones, at greater distances, and on non-Wi-Fi frequency bands. The robust system should also incorporate an automated channel sensing technique, as the current experiments fix the eaves-dropping to a specific communication channel. Non-line-of-sight RF detection experiment should

be carefully studied and analyzed in the presence of occlusions such as buildings. Future drone detection system could identify other aspects of the drone beyond merely its presence, such as its weight, number of propellers, location, speed, and direction. Moreover, an evaluation of the impact of the environment on the accuracy of detection should be investigated.

Drone-defense would not only detect one or multiple drones at the same time but also characterize the drones in detail such as cargo load, number of propellers, manufacturers features, and so on. As mentioned earlier, this research direction would be very interesting to RF sensing researcher where the unique characteristics among drones are studied and analyzed to detect unauthorized drones.

Localizing and tracking drones using multiple passive radio stations and optimizing the station coordination are challenging yet important topics in order to provide a geographical fencing system. Proper wireless network protocol must be designed to collaborate and coordinate multiple wireless sensing stations to detect and analyze the drone when it flies at high speed. Novel synchronization technique is required to overcome MHz-level operation of state-of-the-art SDR platform for gathering the data at multiple wireless sensing stations properly.

Also, in the future, we hope to address the fact that our system is not currently capable of detecting multiple drones in the same vicinity at the same time. We believe that a network of the sensing system is needed to properly detect and characterize multiple drones at the same time. Multimodality approach of combining RF-based, acoustic-based, and video-based solution in a cost-effective manner may become a neat solution to make the system ready for massive deployment.

Using similar approach of drone detection, we believe researchers can develop a new class of applications ranging from sensing the status of different machines in a smart house environment including washing machine, dryer machine, coffee maker, etc. The signals emitted from these devices, which is traditionally used to communicate cloud through Wi-Fi access points, can be used to specify the status of these machines. There would be multiple levels of sensing can be applied in these cases. The first level of sensitivity is to sense whether these machines are on or off. The

second level would be what is the stage of the machine (e.g., 30%, 70% of the process). The other level of sense is to combine the sensing data from multiple objects status and infer the environment information more clearly and accurately.

■ **Continue exploring the feasibility of sensing indoor location leveraging forwarded GPS signal.** The shifting frequencies mechanism is currently the best solution to overcome the impact of the forwarded signal to live GPS-based devices. We will investigate more to see the better solution to overcome this challenges. Next, our existing solutions only utilizes the relative height between the Wi-Fi AP and receiver for 3D localization. Even though the GPS can offer the altitude value, the inaccuracy is still a bit high compared to the longitude and latitude. However, we expect that as the accuracy of GPS will be improved in the near future [212], the proposed system can provide geographic coordinate values in 3D very accurately. We would like to miniaturize the prototype by revising PCB design and then designing ASIC circuit. The hardware prototype acts as a record and replay component, which is a little bit expensive. We believe that if the system is mass produced, the price should be significantly reduced. While the current system is implemented on SDR, we wish to implement it on a smart-phones as done in [204]. Given raw GPS measurement that is currently supported by Android [213], we can utilize this API to override the positioning result obtained from receiver algorithms. Any location-based applications can easily incorporate this library to obtain high accuracy of the proposed technique. In addition, in an office building, the APs signal from outside can be forwarded to deep inner areas using multi-hop. This scenario is very complicated due to the unknown location of the APs, the angle of antennas in each AP, as well as the arrangement of AP respective to each other.

## Bibliography


[1] Wansuree Massagram, Victor M. Lubecke, and Olga Boric-Lubecke. Microwave non-invasive sensing of respiratory tidal volume. EEE Engineering in Medicine and Biology Society., 2009:4832–4835, 2009.

[2] Fadel Adib, Zachary Kabelac, Dina Katabi, and Robert C. Miller. 3d Tracking via Body Radio Reflections. In Proceedings of the 11th USENIX Conference on Networked Systems Design and Implementation, NSDI'14, pages 317–329, Berkeley, CA, USA, 2014. USENIX Association.

[3] N. Patwari, L. Brewer, Q. Tate, O. Kaltiokallio, and M. Bocca. Breathfinding: A Wireless Network That Monitors and Locates Breathing in a Home. IEEE Journal of Selected Topics in Signal Processing, 8(1):30–42, February 2014.

[4] Byung-Jun Jang Yong-Jun An. Detection of Human Vital Signs and Estimation of Direction of Arrival Using Multiple Doppler Radars. Journal of electromagnetic engineering and science, 10(4), 2010.

[5] A.D. Droitcour, O. Boric-Lubecke, V.M. Lubecke, Jenshan Lin, and G.T.A. Kovacs. Range correlation and I/Q performance benefits in single-chip silicon Doppler radars for noncontact cardiopulmonary monitoring. IEEE Transactions on Microwave Theory and Techniques, 52(3):838–848, March 2004.

[6] Li Lu, Changzhan Gu, Changzhi Li, and Jenshan Lin. Doppler Radar Noncontact Vital Sign Monitoring. In Zhi Yang, editor, Neural Computation, Neural Devices, and Neural Prosthesis, pages 41–62. Springer New York, 2014. DOI: 10.1007/978-1-4614-8151-5_3.

[7] Fadel Adib, Hongzi Mao, Zachary Kabelac, Dina Katabi, and Robert C. Miller. Smart Homes That Monitor Breathing and Heart Rate. In Proceedings of the 33rd Annual ACM Conference on Human Factors in Computing Systems, CHI '15, pages 837–846, New York, NY, USA, 2015. ACM.

[8] W. Massagram, N. Hafner, V. Lubecke, and O. Boric-Lubecke. Tidal Volume Measurement Through Non-Contact Doppler Radar With DC Reconstruction. IEEE Sensors Journal, 13(9):3397–3404, September 2013.

[9] DroneShield. Drone detection. https://goo.gl/y5ZuMm, 2016. [Online; accessed Nov 01, 2016].

[10] Newshub. Big noise for kiwis' quiet drone. https://goo.gl/ioa6hj, April 25, 2016.

[11] DeDrone. Drone tracker. http://www.dedrone.com/en/, 2016. [Online; accessed Nov 01, 2016].

[12] IEC. IEC infrared systems: Banshee. https://goo.gl/TLDjFb, 2016. [Online; accessed Nov 01, 2016].

[13] DDC-LLC. Domestic drone countermeasures. https://goo.gl/ZAju6O.

[14] Matthew Peacock and Michael N Johnstone. Towards detection and control of civilian unmanned aerial vehicles. 2013.

[15] Phuc Nguyen, Mahesh Ravindranatha, Anh Nguyen, Richard Han, and Tam Vu. Investigating cost-effective rf-based detection of drones. In ACM MobiSys Dronet, pages 17–22, 2016.

[16] Ron Abileah, Phillip A Fox, and Joseph W Maresca Jr. Detection of low observable objects in clutter using non-coherent radars, February 23 2016. US Patent 9,268,008.

[17] Nicholas J Willis and Hugh D Griffiths. Advances in bistatic radar. SciTech Publishing, 2007.

[18] J Brown, K Woodbridge, A Stove, and S Watts. Air target detection using airborne passive bistatic radar. Electronics letters, pages 1396–1397, 2010.

[19] P. Nguyen, Xinyu Zhang, Ann Halbower, and Tam Vu. Continuous and fine-grained breathing volume monitoring from afar using wireless signals. In IEEE INFOCOM 2016, pages 1–9, 2016.

[20] P. Nguyen, Shane Transue, Min-Hyung Choi, Ann C. Halbower, and Tam Vu. WiKiSpiro: Non-contact Respiration Volume Monitoring During Sleep. In ACM S3 2016, pages 27–29, 2016.

[21] P. Nguyen, Xinyu Zhang, Ann C. Halbower, and Tam Vu. Continuous and Fine-grained Respiration Volume Monitoring Using Continuous Wave Radar. In ACM MobiCom, pages 266–268. ACM, 2015.

[22] Fabiola Colone et al. A multistage processing algorithm for disturbance removal and target detection in passive bistatic radar. IEEE Transactions on Aerospace and Electronic Systems, pages 698–722, 2009.

[23] Berger et al. Signal processing for passive radar using ofdm waveforms. IEEE Journal of Selected Topics in Signal Processing, pages 226–238, 2010.

[24] Buonanno et al. Wifi-based passive bistatic radar by using moving target indicator and least square adaptive filtering. In IEEE International Symposium on Phased Array Systems & Technology, pages 174–179, 2013.

[25] Patrick Maechler et al. Compressive sensing for wifi-based passive bistatic radar. In EUSIPCO, pages 1444–1448, 2012.

[26] Ernesto Conte et al. Multistatic radar detection: synthesis and comparison of optimum and suboptimum receivers. Communications, Radar and Signal Processing, IEE Proceedings F, pages 484–494, 1983.

[27] S KALANTARI Laleh et al. Detection, identification and tracking of flying objects in three dimensions using multistatic radars. Int'l J. of Communications, Network and System Sciences, 2009.

[28] Cranenbroeck J.V.-Rizos C. Pahwa A. Politi N. Barnes, J. Long term performance analysis of a new ground-transceiver positioning network (locatanet) for structural deformation. In FIG Working Week, 2007.

[29] A. Jovancevic, N. Bhatia, J. Noronha, B. Sirpatil, M. Kirchner, and D. Saxena. Tests of a Flexible Pseudolite-Based Navigation System. GPS World, March, 1, 2007.

[30] Chris Rizos. Pseudolite augmentation of GPS. Sydney, NSW, 2052, 2005.

[31] Y. Chen and X. He. Pseudolite-augmented GPS survey technique for deformation monitoring: analysis and experimental study, 3rd IAG. In 12th FIG Symposium, pages 22–24, 2006.

[32] Gorana Novakovi, Almin DJapo, and Dijana Kodi. Pseudolite applications in positioning and navigation. In 10th International Multidisciplinary Scientific Geo-Conference & EXPO SGEM 2010, 2010.

[33] Haruhiko Niwa, Kenri Kodaka, Yoshihiro Sakamoto, Masaumi Otake, Seiji Kawaguchi, Kenjirou Fujii, Yuki Kanemori, and S. Sugano. Gps-based indoor positioning system with multichannel pseudolite. In 2008 IEEE International Conference on Robotics and Automation, pages 905–910, May 2008.

[34] A. Rusu-Casandra, I. Marghescu, and E. S. Lohan. Estimators of the indoor channel for gps-based pseudolite signal. In 2010 9th International Symposium on Electronics and Telecommunications, pages 233–236, Nov 2010.

[35] N. Jardak and N. Samama. Indoor positioning based on gps-repeaters: Performance enhancement using an open code loop architecture. IEEE Transactions on Aerospace and Electronic Systems, 45(1):347–359, Jan 2009.

[36] Alexandre Vervisch-Picois and Nel Samama. Interference mitigation in a repeater and pseudolite indoor positioning system. IEEE Journal of Selected Topics in Signal Processing, 3(5):810–820, 2009.

[37] Alexandre Vervisch-Picois and Nel Samama. Systemic interference mitigation with a combined repeater/pseudolite approach for indoor positioning. In ITM'09: The 2009 International Technical Meeting of the Institute of Navigation, pages 157–166, 2009.

[38] A. Vervisch-Picois, I. Selmi, Y. Gottesman, and N. Samama. Current status of the repealite based approach: A sub-meter indoor positioning system. In 2010 5th ESA Workshop on Satellite Navigation Technologies and European Workshop on GNSS Signals and Signal Processing (NAVITEC), pages 1–6, Dec 2010.

[39] A. Vervisch-Picois and N. Samama. First experimental performances of the repealite based indoor positioning system. In 2012 International Symposium on Wireless Communication Systems (ISWCS), pages 636–640, Aug 2012.

[40] I. Selmi, A. Vervisch-Picois, Y. Gottesman, and N. Samama. Experimental positioning results of the repealite based indoor positioning system. In International Conference on Indoor Positioning and Indoor Navigation (IPIN), 2012.

[41] Ikhlas Selmi, Alexandre Vervisch-Picois, Yaneck Gottesman, and Nel Samama. Optical and radio calibration of the repealite based indoor positioning system. In Indoor Positioning and Indoor Navigation (IPIN), 2012 International Conference on, pages 1–8. IEEE, 2012.

[42] Alexandre Vervisch-Picois, Ikhlas Selmi, Francois Delavault, Yaneck Gottesman, and Nel Samama. Experimental positioning results of the repealite based indoor positioning system: preliminary 2d results. In IPIN'12: International Conference on Indoor Positioning and Indoor Navigation, 2012.

[43] Ikhlas Selmi and Nel Samama. Indoor positioning with gps and glonass-like signals use of new codes and a repealite-based infrastructure in a typical museum building. annals of telecommunications - annales des télécommunications, 69(11):641–655, Dec 2014.

[44] Chen W.-Xu Y. Ji S. Xu, R. A new indoor positioning system architecture. Sensors, (5):10074–10087, 2015.

[45] Shahriar Nirjon, Jie Liu, Gerald DeJean, Bodhi Priyantha, Yuzhe Jin, and Ted Hart. COIN-GPS: Indoor Localization from Direct GPS Receiving. In Proceedings of the 12th Annual International Conference on Mobile Systems, Applications, and Services, pages 301–314. ACM, 2014.

[46] Jie Liu, Bodhi Priyantha, Ted Hart, Heitor S. Ramos, Antonio A. F. Loureiro, and Qiang Wang. Energy Efficient GPS Sensing with Cloud Offloading. In Proceedings of the 10th ACM Conference on Embedded Network Sensor Systems, pages 85–98. ACM, 2012.

[47] Manuel Eichelberger, Kevin Luchsinger, Simon Tanner, and Roger Wattenhofer. Indoor localization with aircraft signals. In ACM SenSys'17, SenSys '17, 2017.

[48] Anthony LaMarca, Yatin Chawathe, Sunny Consolvo, Jeffrey Hightower, Ian Smith, James Scott, Timothy Sohn, James Howard, Jeff Hughes, Fred Potter, Jason Tabert, Pauline Powledge, Gaetano Borriello, and Bill Schilit. Place lab: Device positioning using radio beacons in the wild. In Pervasive Computing, pages 116–133, 2005.

[49] Veljo Otsason. Accurate indoor localization using wide GSM fingerprinting. PhD Thesis, 2005.

[50] BD SHASHIKA Lakmali and Dileeka Dias. Database correlation for GSM location in outdoor & indoor environments. In Information and Automation for Sustainability, 2008. ICIAFS 2008. 4th International Conference on, pages 42–47. IEEE, 2008.

[51] Bruce Denby, Yacine Oussar, Iness Ahriz, and Grard Dreyfus. High-performance indoor localization with full-band GSM fingerprints. In Communications Workshops, 2009. ICC Workshops 2009. IEEE International Conference on, pages 1–5. IEEE, 2009.

[52] Paul A. Zandbergen. Accuracy of iPhone locations: A comparison of assisted GPS, WiFi and cellular positioning. Transactions in GIS, 13(s1):5–25, 2009.

[53] Iness Ahriz, Yacine Oussar, Bruce Denby, and Grard Dreyfus. Full-band GSM fingerprints for indoor localization using a machine learning approach. International Journal of Navigation and Observation, 2010, 2010.

[54] Eladio Martin, Oriol Vinyals, Gerald Friedland, and Ruzena Bajcsy. Precise indoor localization using smart phones. In Proceedings of the 18th ACM international conference on Multimedia, pages 787–790. ACM, 2010.

[55] H. Buyruk, A. K. Keskin, . endil, H. elebi, H. P. Partal, . leri, E. Zeydan, and S. Ergt. Rf fingerprinting based gsm indoor localization. In 2013 21st Signal Processing and Communications Applications Conference (SIU), pages 1–4, 2013.

[56] K. Qiu, F. Zhang, and M. Liu. Visible light communication-based indoor localization using gaussian process. In 2015 IEEE/RSJ International Conference on Intelligent Robots and Systems (IROS), pages 3125–3130, Sept 2015.

[57] Galile0. Bluetooth GPS Spoofing. https://goo.gl/UwzDnc, 2018. [Online; accessed Sep 19, 2018].

[58] Aleksandar Matic, Andrei Papliatseyeu, Venet Osmani, and Oscar Mayora-Ibarra. Tuning to your position: FM radio based indoor localization with spontaneous recalibration. In Pervasive Computing and Communications (PerCom), 2010 IEEE International Conference on, pages 153–161. IEEE, 2010.

[59] Stephen P. Tarzia, Peter A. Dinda, Robert P. Dick, and Gokhan Memik. Indoor localization without infrastructure using the acoustic background spectrum. In Proceedings of the 9th international conference on Mobile systems, applications, and services, pages 155–168. ACM, 2011.

[60] Vahideh Moghtadaiee, Andrew G. Dempster, and Samsung Lim. Indoor localization using fm radio signals: A fingerprinting approach. In Indoor Positioning and Indoor Navigation (IPIN), 2011 International Conference on, pages 1–7. IEEE, 2011.

[61] Andrei Popleteev, Venet Osmani, and Oscar Mayora. Investigation of indoor localization with ambient FM radio stations. In Pervasive Computing and Communications (PerCom), 2012 IEEE International Conference on, pages 171–179. IEEE, 2012.

[62] Yin Chen, Dimitrios Lymberopoulos, Jie Liu, and Bodhi Priyantha. Fm-based indoor localization. In Proceedings of the 10th international conference on Mobile systems, applications, and services, pages 169–182. ACM, 2012.

[63] Sungro Yoon, Kyunghan Lee, and Injong Rhee. FM-based indoor localization via automatic fingerprint DB construction and matching. In Proceeding of the 11th annual international conference on Mobile systems, applications, and services, pages 207–220. ACM, 2013.

[64] Yin Chen, Dimitrios Lymberopoulos, Jie Liu, and Bodhi Priyantha. Indoor localization using fm signals. IEEE Transactions on Mobile Computing, 12(8):1502–1517, 2013.

[65] Soo-Yong Jung, Swook Hann, and Chang-Soo Park. TDOA-based optical wireless indoor localization using LED ceiling lamps. IEEE Transactions on Consumer Electronics, 57(4), 2011.

[66] W. Zhang and M. Kavehrad. A 2-D indoor localization system based on visible light LED. In Photonics Society Summer Topical Meeting Series, 2012 IEEE, pages 80–81. IEEE, 2012.

[67] Thomas Q. Wang, Y. Ahmet Sekercioglu, Adrian Neild, and Jean Armstrong. Position accuracy of time-of-arrival based ranging using visible light with application in indoor localization systems. Journal of Lightwave Technology, 31(20):3302–3308, 2013.

[68] Se-Hoon Yang, Deok-Rae Kim, Hyun-Seung Kim, Yong-Hwan Son, and Sang-Kook Han. Visible light based high accuracy indoor localization using the extinction ratio distributions of light signals. Microwave and Optical Technology Letters, 55(6):1385–1389, 2013.

[69] Muhammad Yasir, Siu-Wai Ho, and Badri N. Vellambi. Indoor localization using visible light and accelerometer. In Global Communications Conference (GLOBECOM), 2013 IEEE, pages 3341–3346. IEEE, 2013.

[70] Ming Liu, Kejie Qiu, Fengyu Che, Shaohua Li, Babar Hussain, Liang Wu, and C. Patrick Yue. Towards indoor localization using visible light communication for consumer electronic devices. In Intelligent Robots and Systems (IROS 2014), 2014 IEEE/RSJ International Conference on, pages 143–148. IEEE, 2014.

[71] Ye-Sheng Kuo, Pat Pannuto, Ko-Jen Hsiao, and Prabal Dutta. Luxapose: Indoor positioning with mobile phones and visible light. In Proceedings of the 20th annual international conference on Mobile computing and networking, pages 447–458. ACM, 2014.

[72] Qiang Xu, Rong Zheng, and Steve Hranilovic. IDyLL: indoor localization using inertial and light sensors on smartphones. In Proceedings of the 2015 ACM International Joint Conference on Pervasive and Ubiquitous Computing, pages 307–318. ACM, 2015.

[73] Manikanta Kotaru, Kiran Joshi, Dinesh Bharadia, and Sachin Katti. SpotFi: Decimeter Level Localization Using WiFi. In Proceedings of the 2015 ACM Conference on Special Interest Group on Data Communication, pages 269–282. ACM, 2015.

[74] Jie Xiong, Karthikeyan Sundaresan, and Kyle Jamieson. ToneTrack: Leveraging Frequency-Agile Radios for Time-Based Indoor Wireless Localization. In Proceedings of the 21st Annual International Conference on Mobile Computing and Networking, MobiCom '15, pages 537–549, New York, NY, USA, 2015. ACM.

[75] Jon Gjengset, Jie Xiong, Graeme McPhillips, and Kyle Jamieson. Phaser: Enabling Phased Array Signal Processing on Commodity WiFi Access Points. In Proceedings of the 20th Annual International Conference on Mobile Computing and Networking, MobiCom '14, pages 153–164, New York, NY, USA, 2014. ACM.

[76] Lei Yang, Yekui Chen, Xiang-Yang Li, Chaowei Xiao, Mo Li, and Yunhao Liu. Tagoram: Real-time Tracking of Mobile RFID Tags to High Precision Using COTS Devices. In Proceedings of the 20th Annual International Conference on Mobile Computing and Networking, MobiCom '14, pages 237–248, New York, NY, USA, 2014. ACM.

[77] Swarun Kumar, Ezzeldin Hamed, Dina Katabi, and Li Erran Li. LTE Radio Analytics Made Easy and Accessible. In Proceedings of the 2014 ACM Conference on SIGCOMM, SIGCOMM '14, pages 211–222, New York, NY, USA, 2014. ACM.

[78] Jie Xiong and Kyle Jamieson. ArrayTrack: A Fine-grained Indoor Location System. In Proceedings of the 10th USENIX Conference on Networked Systems Design and Implementation, nsdi'13, pages 71–84, Berkeley, CA, USA, 2013. USENIX Association.

[79] Peng Rong and Mihail L. Sichitiu. Angle of arrival localization for wireless sensor networks. In Sensor and Ad Hoc Communications and Networks, 2006. SECON'06. 2006 3rd Annual IEEE Communications Society on, volume 1, pages 374–382. IEEE, 2006.

[80] Carl Wong, Richard Klukas, and Geoffrey G. Messier. Using WLAN infrastructure for angle-of-arrival indoor user location. In Vehicular Technology Conference, 2008. VTC 2008-Fall. IEEE 68th, pages 1–5. IEEE, 2008.

[81] Asis Nasipuri and Ribal El Najjar. Experimental evaluation of an angle based indoor localization system. In Modeling and Optimization in Mobile, Ad Hoc and Wireless Networks, 2006 4th International Symposium on, pages 1–9. IEEE, 2006.

[82] Alex T. Mariakakis, Souvik Sen, Jeongkeun Lee, and Kyu-Han Kim. Sail: Single access point-based indoor localization. In Proceedings of the 12th annual international conference on Mobile systems, applications, and services, pages 315–328. ACM, 2014.

[83] Swarun Kumar, Stephanie Gil, Dina Katabi, and Daniela Rus. Accurate indoor localization with zero start-up cost. In Proceedings of the 20th annual international conference on Mobile computing and networking, pages 483–494. ACM, 2014.

[84] Ho-lin Chang, Jr-ben Tian, Tsung-Te Lai, Hao-Hua Chu, and Polly Huang. Spinning beacons for precise indoor localization. In Proceedings of the 6th ACM conference on Embedded network sensor systems, pages 127–140. ACM, 2008.

[85] Deepak Vasisht, Swarun Kumar, and Dina Katabi. Decimeter-level Localization with a Single WiFi Access Point. In Proceedings of the 13th Usenix Conference on Networked Systems Design and Implementation, NSDI'16, pages 165–178, Berkeley, CA, USA, 2016. USENIX Association.

[86] Sudhir Kurl, Sae Young Jae, Jussi Kauhanen, Kimmo Ronkainen, and Jari A. Laukkanen. Impaired pulmonary function is a risk predictor for sudden cardiac death in men. Annals of Medicine, 47(5):381–385, 2015.

[87] Sleepfoundation. Pregnancy and sleep, 2016. July 26, 2016.

[88] Francesca L. Facco, David W. Ouyang, Phyllis C. Zee, and William A. Grobman. Sleep disordered breathing in a high-risk cohort prevalence and severity across pregnancy. American Journal of Perinatology, 31(10):899–904, November 2014.

[89] Carole L. Marcus, Lee Jay Brooks, Kari A. Draper, David Gozal, Ann Carol Halbower, Jacqueline Jones, Michael S. Schechter, Stephen Howard Sheldon, Karen Spruyt, Sally Davidson Ward, Christopher Lehmann, and Richard N. Shiffman. Diagnosis and Management of Childhood Obstructive Sleep Apnea Syndrome. Pediatrics, 130(3):576–584, September 2012.

[90] Massimo R. Mannarino, Francesco Di Filippo, and Matteo Pirro. Obstructive sleep apnea syndrome. European Journal of Internal Medicine, 23(7):586–593, October 2012.

[91] Ann C. Halbower, Stacey L. Ishman, and Brian M. McGinley. Childhood obstructive sleep-disordered breathing: a clinical update and discussion of technological innovations and challenges. Chest, 132(6):2030–2041, December 2007.

[92] Meng-Chieh Yu, Jia-Ling Liou, Shuenn-Wen Kuo, Ming-Sui Lee, and Yi-Ping Hung. Non-contact respiratory measurement of volume change using depth camera. IEEE Engineering in Medicine and Biology Society., 2012:2371–2374, 2012.

[93] T. Kondo, T. Uhlig, P. Pemberton, and P. D. Sly. Laser monitoring of chest wall displacement. The European Respiratory Journal, 10(8):1865–1869, August 1997.

[94] J. Vargas and C. O. S. Sorzano. Quadrature Component Analysis for interferometry. Optics and Lasers in Engineering, 51(5):637–641, May 2013.

[95] L. Boccanfuso and J. O'Kane. Remote measurement of breathing rate in real time using a high precision, single-point infrared temperature sensor. In 2012 IEEE RAS EMBS International Conference on Biomedical Robotics and Biomechatronics (BioRob), pages 1704–1709, June 2012.

[96] Yanzhi Ren, Chen Wang, Jie Yang, and Yingying Chen. Fine-grained sleep monitoring: Hearing your breathing with smartphones. pages 1194–1202.

[97] Rajalakshmi Nandakumar, Shyamnath Gollakota, and Nathaniel Watson. Contactless Sleep Apnea Detection on Smartphones. In Proceedings of the 13th Annual International Conference on Mobile Systems, Applications, and Services, MobiSys '15, pages 45–57, New York, NY, USA, 2015. ACM.

[98] Jian Liu, Yan Wang, Yingying Chen, Jie Yang, Xu Chen, and Jerry Cheng. Tracking Vital Signs During Sleep Leveraging Off-the-shelf WiFi. In Proceedings of the 16th ACM International Symposium on Mobile Ad Hoc Networking and Computing, MobiHoc '15, pages 267–276, New York, NY, USA, 2015. ACM.

[99] S. Transue, P. Nguyen, Vu T., and Choi Min-Hyung. Real-time tidal volume estimation using iso-surface reconstruction. In 2016 The IEEE (CHASE), 2016.

[100] A. De Groote, M. Wantier, G. Cheron, M. Estenne, and M. Paiva. Chest wall motion during tidal breathing. Journal of Applied Physiology (Bethesda, Md.: 1985), 83(5):1531–1537, November 1997.

[101] David J. C. MacKay. Bayesian Methods for Adaptive Models. 1992.

[102] J. Ghaboussi, J. H. Garrett Jr, and X. Wu. KnowledgeBased Modeling of Material Behavior with Neural Networks. Journal of Engineering Mechanics, 117(1):132–153, 1991.

[103] MIT Press. Naturally Intelligent Systems, 2016.

[104] Radford Neal. Bayesian Training of Backpropagation Networks by the Hybrid Monte Carlo Method. Technical report, 1993.

[105] Vernier. Vernier Spirometer, 2016. July 26, 2016.

[106] Teng Wei, Shu Wang, Anfu Zhou, and Xinyu Zhang. Acoustic Eavesdropping Through Wireless Vibrometry. In Proceedings of Annual International Conference on Mobile Computing and Networking, MobiCom '15, pages 130–141, New York, NY, USA, 2015. ACM.

[107] Alexander Ihler, Jon Hutchins, and Padhraic Smyth. Learning to Detect Events with Markov-modulated Poisson Processes. ACM Trans. Knowl. Discov. Data, 1(3), December 2007.

[108] L. Ahlbom, A. Forsen, and L. Zetterberg. Signal processing for event detection. In Acoustics, Speech, and Signal Processing, IEEE International Conference on ICASSP '82., volume 7, pages 1890–1893, May 1982.

[109] M. A. Jaber and D. Massicotte. Fast method to detect specific frequencies in monitored signal. In 2010 4th International Symposium on Communications, Control and Signal Processing (ISCCSP), pages 1–5, March 2010.

[110] John G. Herriot and Christian H. Reinsch. Algorithm 507: Procedures for Quintic Natural Spline Interpolation [E1]. ACM Trans. Math. Softw., 2(3):281–289, September 1976.

[111] Hazewinkel Michiel. Spline interpolation. Encyclopedia of Mathematics, Springer, 2001.

[112] WARP. WARP Project, 2016.

[113] Inc Applied Motion Products. Applied motion. stm24s-3ee, 2016.

[114] Cinetics. Cinetics, 2016. Retreived in July, 2016.

[115] Krishna C. Garikipati and Kang G. Shin. Improving Transport Design for WARP SDR Deployments. In Proceedings of ACM Workshop on Software Radio Implementation Forum, SRIF '14, pages 1–6, New York, NY, USA, 2014. ACM.

[116] FlexReport. The economics of drone delivery. https://goo.gl/RN4irU, 2016. [Online; accessed Nov 01, 2016].

[117] Amazon. Amazon prime air. https://goo.gl/Ags0YJ, 2016. [Online; accessed Nov 01, 2016].

[118] Julien Fleureau et al. Generic Drone Control Platform for Autonomous Capture of Cinema Scenes. In ACM MobiSys Dronet, pages 35–40, 2016.

[119] Wired. Surrey now has the uk's 'largest' police drone project. https://goo.gl/VzrdQf, 2016. [Online; accessed Nov 01, 2016].

[120] Techcrunch. Firefighting drone serves as a reminder to be careful with crowdfunding campaigns. https://goo.gl/WwFgWk, 2016. [Online; accessed Nov 01, 2016].

[121] CNN. Dubai deploys a 'drone hunter' to keep its airport open. https://goo.gl/iXJMu3, 2016. [Online; accessed Nov 01, 2016].

[122] Washington Post. Prisons try to stop drones from delivering drugs, porn and cellphones to inmates. https://goo.gl/6DapQM, October 13, 2016.

[123] Bart Jansen. Drone crash at white house reveals security risks. USA Today, January 26, 2015.

[124] Patrick McGreevy. Private drones are putting firefighters in 'immediate danger,' california fire official says. LA Times, August 18, 2015.

[125] David Waldstein. Drone crash interrupts match. New York Times, September 3, 2015.

[126] CNN. Drone crashes onto piste, misses champion skier by inches. https://goo.gl/jtPdLh, 2015. [Online; accessed Nov 01, 2016].

[127] LA Times. To keep drones out of high-risk areas, companies try hijacking them and shooting them down. https://goo.gl/MqDag5, 2016. [Online; accessed Nov 01, 2016].

[128] Dinesh Sathyamoorthy. A review of security threats of unmanned aerial vehicles and mitigation steps.

[129] Reid Vander Schaaf. What technologies or integrating concepts are needed for the US military to counter future missile threats looking out to 2040? PhD thesis, US Army, 2014.

[130] TODD HUMPHREYS. Statement on the security threat posed by unmanned aerial systems and possible countermeasures, 2015.

[131] Johann-Sebastian Pleban et al. Hacking and securing the ar. drone 2.0 quadcopter: investigations for improving the security of a toy. In SPIE Electronic Imaging, 2014.

[132] BBC. Dutch police fight drones with eagles. https://goo.gl/PnJCcd, September 12, 2016.

[133] Zain Naboulsi. Drone detection: What works and what doesn't. https://goo.gl/MkfHoF, 2016. [Online; accessed Nov 01, 2016].

[134] Robert Mahony, Vijay Kumar, and Peter Corke. Multirotor aerial vehicles: Modeling, estimation, and control of quadrotor. IEEE robotics & automation magazine, pages 20–32, 2012.

[135] Gabriel Hoffmann et al. Quadrotor Helicopter Flight Dynamics and Control: Theory and Experiment. In AIAA Guidance, Navigation and Control Conference and Exhibit. 2007.

[136] Marketsandmarkets. Multirotor uav market worth $2.28 billion by 2020. https://goo.gl/1M43OD, 2016. [Online; accessed Nov 01, 2016].

[137] Reportbuyer. Global multi-rotor drone market - analysis and forecast 2016-2022 (focus on major applications payloads and, pricing). https://goo.gl/Z6Z2gF, 2017. [Online; accessed Apr 17, 2017].

[138] A. Tayebi and S. McGilvray. Attitude stabilization of a four-rotor aerial robot. In IEEE CDC, pages 1216–1221, 2004.

[139] I. C. Dikmen, A. Arisoy, and H. Temeltas. Attitude control of a quadrotor. In RAST, pages 722–727, 2009.

[140] Z. Zuo. Trajectory tracking control design with command-filtered compensation for a quadrotor. IET Control Theory Applications, pages 2343–2355, 2010.

[141] S. Bouabdallah, A. Noth, and R. Siegwart. PID vs LQ control techniques applied to an indoor micro quadrotor. pages 2451–2456, 2004.

[142] T. Madani and A. Benallegue. Backstepping Control for a Quadrotor Helicopter. In IEEE/RSJ IROS, pages 3255–3260, 2006.

[143] K. M. Zemalache, L. Beji, and H. Marref. Control of an under-actuated system: application a four rotors rotorcraft. In IEEEROBIO, pages 404–409, 2005.

[144] Guilherme V. Raffo and dothers. An Integral Predictive/Nonlinear H∞ Control Structure for a Quadrotor Helicopter. Automatica, pages 29–39, 2010.

[145] Castillo et al. Real-time stabilization and tracking of a four-rotor mini rotorcraft. IEEE Transactions on Control Systems Technology, pages 510–516, 2004.

[146] J. Escareno, S. Salazar-Cruz, and R. Lozano. Embedded control of a four-rotor UAV. In American Control Conference, page 6, 2006.

[147] H. Huang et al. Aerodynamics and control of autonomous quadrotor helicopters in aggressive maneuvering. In IEEE ICRA, pages 3277–3282, 2009.

[148] Endri Bregu, Nicola Casamassima, Daniel Cantoni, Luca Mottola, and Kamin Whitehouse. Reactive control of autonomous drones. In ACM MobiSys, pages 207–219, 2016.

[149] Ying-Chih Lai and Shau-Shiun Jan. Attitude estimation based on fusion of gyroscopes and single antenna GPS for small UAVs under the influence of vibration. GPS Solutions, pages 67–77, 2011.

[150] Ruth Heffernan et al. Vibration analysis of the SA349/2 helicopter. NASA Technical Memorandum 102794, 1991.

[151] Xianhua Liu and RB Randall. Blind source separation of internal combustion engine piston slap from other measured vibration signals. Mechanical Systems and Signal Processing, pages 1196–1208, 2005.

[152] Leo Leroy Beranek. Noise and vibration control engineering: principles and applications. Wiley, 1992.

[153] Parrot. Parrot Bebop Drone. https://goo.gl/xZ36IF, 2016. [Online; accessed Nov 01, 2016].

[154] DJI. DJI Phantom. http://www.dji.com/, 2016. [Online; accessed Nov 01, 2016].

[155] Sparkfun-InvenSense. Mpu 9150. https://goo.gl/Hh3viK, 2016. [Online; accessed Nov 01, 2016].

[156] Arduino. Pro mini. https://goo.gl/AGFeCN, 2016. [Online; accessed Nov 01, 2016].

[157] Bluetooth. Bluetooth hc-05. https://goo.gl/0PKs6r, 2016. [Online; accessed Nov 01, 2016].

[158] USRP. B200 Mini. https://goo.gl/7ssQDP, 2016. [Online; accessed Nov 01, 2016].

[159] Carl Taswell and Kevin C. McGill. Algorithm 735: Wavelet transform algorithms for finite-duration discrete-time signals. ACM Trans. Math. Softw., pages 398–412, 1994.

[160] David Tse and Pramod Viswanath. Fundamentals of Wireless Communication. 2005.

[161] L.-K. Shark and C. Yu. Design of Matched Wavelets Based on Generalized Mexican-hat Function. Signal Process., pages 1451–1469, 2006.

[162] Toni Giorgino. Computing and visualizing dynamic time warping alignments in R: The dtw package. Journal of Statistical Software, pages 1–24, 2009.

[163] Paolo Tormene et al. Matching incomplete time series with dynamic time warping: An algorithm and an application to post-stroke rehabilitation. Artificial Intelligence in Medicine, pages 11–34, 2008.

[164] Pimwadee Chaovalit et al. Discrete Wavelet Transform-based Time Series Analysis and Mining. ACM Comput. Surv., pages 6:1–6:37, 2011.

[165] S. G. Mallat. A Theory for Multiresolution Signal Decomposition: The Wavelet Representation. IEEE Trans. Pattern Anal. Mach. Intell., pages 674–693, July 1989.

[166] L-Com. 2.4 / 5.1-5.8 GHz 20dBi Flat Panel Antenna. https://goo.gl/77WdQD, 2016. [Online; accessed Nov 01, 2016].

[167] Farproc. Wifi analyzer. http://tinyurl.com/8yqxge9.

[168] Protocol New York. Dronium ONE - Special Edition WiFi. https://goo.gl/u4NjuS, 2016. [Online; accessed Nov 01, 2016].

[169] Skyrocket. Sky Viper. http://sky-viper.com/, 2016. [Online; accessed Nov 01, 2016].

[170] Swift Stream. Swiftstreamrc. https://goo.gl/sB0Kro, 2016. [Online; accessed Nov 01, 2016].

[171] Parrot. ARDrone. https://goo.gl/deJFd6, 2016. [Online; accessed Nov 01, 2016].

[172] Protocol New York. Protocol Galileo Stealth. https://goo.gl/TVGPkx, 2016. [Online; accessed Nov 01, 2016].

[173] Louise Hauzenberger and Emma Holmberg Ohlsson. Drone detection using audio analysis. Master's thesis, Department of Electrical and Information Technology, Lund University, Lund, Scania, Sweden, 2015. https://goo.gl/58BGoN.

[174] Artem Rozantsev, Vincent Lepetit, and Pascal Fua. Detecting Flying Objects using a Single Moving Camera. IEEE Transactions on Pattern Analysis and Machine Intelligence, pages 879 – 892, 2017.

[175] Artem Rozantsev, Vincent Lepetit, and Pascal Fua. Flying Objects Detection from a Single Moving Camera. In Conference on Computer Vision and Pattern Recognition (CVPR), 2015.

[176] Mark A. McHenry and Shyam Chunduri. Nsf spectrum occupancy measurement project summary. Shared Spectrum Company Report, 2005.

[177] Mark A. McHenry et al. C. s. chicago spectrum occupancy measurements and analysis and a long-term studies proposal. TAPAS, 2005.

[178] R. I. C. Chiang et al. A Quantitative Analysis of Spectral Occupancy Measurements for Cognitive Radio. In IEEE VTC, pages 3016–3020, 2007.

[179] M. H. Islam et al. Spectrum Survey in Singapore: Occupancy Measurements and Analyses. In EAI CROWNCOM, pages 1–7, 2008.

[180] Federal Communications Commission et al. Wireless e911 location accuracy requirements. Ps Docket, (07-114), 2015.

[181] USA Today. 911's deadly flaw: Lack of location data. https://goo.gl/Y7vjBX, 2018. [Online; accessed Sep 19, 2018].

[182] 3GPP. Study on indoor positioning enhancements for UTRA and LTE (TR 37.857 v13.1.0 Release 13), 2016. https://goo.gl/LSTvQ7.

[183] Innerspace. E911 the z-axis: Indoor location technology to the rescue. https://goo.gl/NEL9kX, 2018. [Online; accessed Sep 19, 2018].

[184] J. Li, Z. Xie, X. Sun, J. Tang, H. Liu, and J. A. Stankovic. An automatic and accurate localization system for firefighters. In 2018 IEEE/ACM Third International Conference on Internet-of-Things Design and Implementation (IoTDI), pages 13–24, April 2018.

[185] NASA. New technology could help track firefighters for safety. https://goo.gl/De1Cic, 2016. [Online; accessed Sep 19, 2018].

[186] P. Bahl and V. N. Padmanabhan. RADAR: an in-building RF-based user location and tracking system. In Proceedings IEEE INFOCOM 2000. Conference on Computer Communications. Nineteenth Annual Joint Conference of the IEEE Computer and Communications Societies, volume 2, pages 775–784, 2000.

[187] Abhishek Goswami, Luis E. Ortiz, and Samir R. Das. WiGEM: A Learning-based Approach for Indoor Localization. In Proceedings of the Seventh COnference on Emerging Networking EXperiments and Technologies, CoNEXT '11. ACM, 2011.

[188] Manuel Eichelberger, Kevin Luchsinger, Simon Tanner, and Roger Wattenhofer. Indoor Localization with Aircraft Signals. In Sensys '17. ACM, 2017.

[189] Z. Zhao, J. Wang, X. Zhao, C. Peng, Q. Guo, and B. Wu. Navilight: Indoor localization and navigation under arbitrary lights. In IEEE INFOCOM 2017 - IEEE Conference on Computer Communications, May 2017.

[190] Kiran Joshi, Steven Hong, and Sachin Katti. PinPoint: Localizing Interfering Radios. In Proceedings of the 10th USENIX Conference on Networked Systems Design and Implementation, nsdi'13. USENIX Association, 2013.

[191] Cisco. Best Practices: Location-Aware WLAN Design Considerations. https://goo.gl/pWkxYm, 2014. [Online; accessed Sep 19, 2018].

[192] Meraki. High Density Wi-Fi Deployment Guide. https://goo.gl/j7msX3, 2018. [Online; accessed Sep 19, 2018].

[193] FalTech GPS. Licensing of GPS Repeaters. https://goo.gl/7u883h, 2018. [Online; accessed Sep 19, 2018].

[194] James Bao-Yen Tsui. Fundamentals of Global Positioning System Receivers: A Software Approach. John Wiley & Sons, 2005.

[195] Johanson Technology Inc. 2450DM40A1575E. https://goo.gl/8cCn37, 2018. [Online; accessed Sep 19, 2018].

[196] Mini-Circuits. ZX60-V82-S+, High Dynamic Range Amplifier, 20 MHz to 6 GHz. https://goo.gl/38xoqT, 2017. [Online; accessed Sep 19, 2018].

[197] R. Schmidt. Multiple emitter location and signal parameter estimation. IEEE Transactions on Antennas and Propagation, 34(3):276–280, March 1986.

[198] Yunfei Ma, Nicholas Selby, and Fadel Adib. Minding the billions: Ultra-wideband localization for deployed rfid tags. In Proceedings of the 23rd Annual International Conference on Mobile Computing and Networking, MobiCom '17, pages 248–260, New York, NY, USA, 2017. ACM.

[199] J.A. Hartigan and M.A. Wong. A k-means clustering algorithm. Journal of the Royal Statistical Society. Series C (Applied Statistics), 28(1), 1979.

[200] Ettus Research. USRP N210. https://goo.gl/BVFpYV, 2018. [Online; accessed Sep 19, 2018].

[201] GNSS SDR. GNSS SDR: An open source Global Navigation Satellite Systems software-defined receiver. https://goo.gl/YqYe3x, 2018. [Online; accessed Sep 19, 2018].

[202] Frank van Diggelen. A-GPS : Assisted GPS, GNSS, and SBAS. Artech House, 2009.

[203] Google. Google Maps. https://www.google.com/maps, 2018. [Online; accessed Sep 19, 2018].

[204] Xiaochen Liu, Suman Nath, and Ramesh Govindan. Gnome: A practical approach to nlos mitigation for gps positioning in smartphones. In Proceedings of the 16th Annual International Conference on Mobile Systems, Applications, and Services, MobiSys '18, pages 163–177, 2018.

[205] Bosch. Glm 80 lithium-ion laser distance measurer. https://goo.gl/6ovD3v, 2018. [Online; accessed Sep 19, 2018].

[206] Guobin Shen, Zhuo Chen, Peichao Zhang, Thomas Moscibroda, and Yongguang Zhang. Walkie-markie: Indoor pathway mapping made easy. In Proceedings of the 10th USENIX Conference on Networked Systems Design and Implementation, nsdi'13, pages 85–98, Berkeley, CA, USA, 2013. USENIX Association.

[207] Mendhak. GPS Logger on Android. https://goo.gl/pw6jtG, 2018. [Online; accessed Sep 19, 2018].

[208] Ulox. UBX-G7020 series. https://goo.gl/U8wSc8, 2018. [Online; accessed Sep 19, 2018].

[209] hostapd: IEEE 802.11 AP, IEEE 802.1X/WPA/WPA2/EAP/RADIUS Authenticator. https://w1.fi/hostapd/, 2013. [Online; accessed Sep 19, 2018].

[210] iPerf - The ultimate speed test tool for TCP, UDP and SCTP. https://iperf.fr, 2018. [Online; accessed Sep 19, 2018].

[211] Andria Bilich and Kristine M. Larson. Mapping the GPS multipath environment using the signal-to-noise ratio (SNR). Radio Science, 42(6), December 2007.

[212] The Verge. GPS will be accurate within one foot in some phones next year. https://goo.gl/dAorqm, 2017. [Online; accessed Sep 19, 2018].

[213] Google. Raw GNSS Measurements. https://goo.gl/umG3vh, 2018. [Online; accessed Sep 19, 2018].

[214] Radford Neal. Bayesian Training of Backpropagation Networks by the Hybrid Monte Carlo Method. Technical report, 1993.

[215] Ron Balkissoon, Steve Lommatzsch, Brendan Carolan, and Barry Make. Chronic obstructive pulmonary disease: a concise review. The Medical Clinics of North America, 95(6):1125–1141, November 2011.

[216] Anders Hst-Madsen, Nicolas Petrochilos, Olga Boric-Lubecke, Victor M. Lubecke, Byung-Kwon Park, and Qin Zhou. Signal Processing Methods for Doppler Radar Heart Rate Monitoring. In Danilo Mandic, Martin Golz, Anthony Kuh, Dragan Obradovic, and Toshihisa Tanaka, editors, Signal Processing Techniques for Knowledge Extraction and Information Fusion, pages 121–140. Springer US, 2008. DOI: 10.1007/978-0-387-74367-7_7.

[217] P. Nguyen, X. Zhang, A. C. Halbower, and T. Vu. Continuous and fine-grained breathing volume monitoring from afar using wireless signals. In 2016 IEEE Conference on Computer Communications (INFOCOM), 2016.

[218] Russell C. Eberhart and Roy W. Dobbins. Neural Network PC Tools: A Practical Guide. Academic Press, San Diego, 1st edition edition, November 1990.

[219] Kurt Hornik. Approximation Capabilities of Multilayer Feedforward Networks. Neural Netw., 4(2):251–257, March 1991.

[220] P. Nguyen, X. Zhang, A. C. Halbower, and T. Vu. Poster: Continuous and Fine-grained Respiration Volume Monitoring Using Continuous Wave Radar. In Proceedings of the 21st Annual International Conference on Mobile Computing and Networking, MobiCom '15, pages 266–268, New York, NY, USA, 2015. ACM.

[221] Y. Li, C. Gu, T. Nikoubin, and C. Li. Wireless radar devices for smart human-computer interaction. In IEEE International Midwest Symposium on Circuits and Systems (MWSCAS), pages 65–68, August 2014.

[222] Nils Ole Tippenhauer, Christina Pöpper, Kasper Bonne Rasmussen, and Srdjan Capkun. On the requirements for successful gps spoofing attacks. In Proceedings of the 18th ACM conference on Computer and communications security, pages 75–86. ACM, 2011.

[223] Prieto. Proto-x remote reversing project. https://github.com/alvarop/protox, 2016. [Online; accessed Nov 01, 2016].

[224] S. Kamlar. Skyjack. http://samy.pl/skyjack/, 2016. [Online; accessed Nov 01, 2016].

[225] R.Sasi. Maldrone the first backdoor for drones. https://goo.gl/Xh3UIb.

[226] Nils Rodday. Hacking a professional drone. https://goo.gl/FCxa4U, 2016. [Online; accessed Nov 01, 2016].

[227] OPENWORKS. Skywall 100. https://goo.gl/EMlX6A, 2016. [Online; accessed Nov 01, 2016].

[228] Eagle for drone. https://goo.gl/n9iemp, 2016. [Online; accessed Nov 01, 2016].

[229] Giorgia Sinibaldi and Luca Marino. Experimental analysis on the noise of propellers for small uav. Applied Acoustics, 74(1):79–88, 2013.

[230] Weiqun Shi, Brett Bishop, Gus Arabadjis, John Yoder, Peter Hill, and Rich Plasse. Detecting, Tracking, and Identifying Airborne Threats with Netted Sensor Fence. INTECH Open Access Publisher, 2011.

[231] Joël Busset, Florian Perrodin, Peter Wellig, Beat Ott, Kurt Heutschi, Torben Rühl, and Thomas Nussbaumer. Detection and tracking of drones using advanced acoustic cameras. In SPIE Security+ Defence, pages 96470F–96470F. International Society for Optics and Photonics, 2015.

[232] How to shoot down a drone. http://tinyurl.com/p5zaso3.

[233] Joseph Serna. Lufthansa jet and drone nearly collide near lax. LA Times, March 19, 2016.

[234] Alison Morrow. Couple accuses neighbor of stalking with drone. USA Today, December 13, 2014.

[235] Julio. Parrot bebop quadcopter review: A (near) flawless drone with the skycontroller. http://tinyurl.com/h394ljk. FPV Drone Reviews, February 05, 2016.

[236] Mango Communications. Warp v3 kit. https://mangocomm.com/products/kits/warp-v3-kit.

[237] Ettus Research. USRP B200. https://www.ettus.com/product/details/UB200-KIT.

[238] Zhongli Liu, Zupei Li, Benyuan Liu, Xinwen Fu, Ioannis Raptis, and Kui Ren. Rise of mini-drones: Applications and issues. In Proceedings of the 2015 Workshop on Privacy-Aware Mobile Computing, ACM MobiHoc, pages 7–12, 2015.

[239] Amazon. Amazon prime air. http://www.amazon.com/b?node=8037720011.

[240] R. Bultitude. Measurement, characterization and modeling of indoor 800/900 MHz radio channels for digital communications. IEEE Communications Magazine, 25(6):5–12, June 1987.

[241] Parrot. Bebop. https://goo.gl/RI7Ftf, 2016. [Online; accessed Nov 01, 2016].

[242] Parrot. Parrot Airborne Night Maclane. https://goo.gl/Al9mpt, 2016. [Online; accessed Nov 01, 2016].

[243] B. K. Park, O. Boric-Lubecke, and V. M. Lubecke. Arctangent Demodulation With DC Offset Compensation in Quadrature Doppler Radar Receiver Systems. IEEE Transactions on Microwave Theory and Techniques, 55(5):1073–1079, May 2007.

[244] D. Gabor. Theory of communication. Journal of the Institution of Electrical Engineers - Part I: General, 94(73):58–, January 1947.

[245] J. A. Roberts and J. R. Abeysinghe. A two-state Rician model for predicting indoor wireless communication performance. In ICC '95 Seattle, 'Gateway to Globalization', 1995 IEEE International Conference on Communications, 1995, volume 1, pages 40–43 vol.1, June 1995.

[246] Endri Bregu, Nicola Casamassima, Daniel Cantoni, Luca Mottola, and Kamin Whitehouse. Reactive Control of Autonomous Drones. In ACM MobiSys, pages 207–219, 2016.

[247] Cleanflight Team. Clean Flight. http://cleanflight.com, 2016. [Online; accessed Nov 01, 2016].

[248] John Ashmead. Morlet Wavelets in Quantum Mechanics. Quanta, 1(1):58–70, November 2012.

[249] Matlab. Morelet wavelet. https://goo.gl/sNkMFf, 2016. [Online; accessed Nov 01, 2016].

[250] John L Crassidis, F Landis Markley, and Yang Cheng. Survey of nonlinear attitude estimation methods. Journal of guidance, control, and dynamics, 30(1):12–28, 2007.

[251] M Kemal Kıymık, Inan Güler, Alper Dizibüyük, and Mehmet Akın. Comparison of stft and wavelet transform methods in determining epileptic seizure activity in eeg signals for real-time application. Computers in biology and medicine, 35(7):603–616, 2005.

[252] Tomáš Krajník, Vojtěch Vonásek, Daniel Fišer, and Jan Faigl. Ar-drone as a platform for robotic research and education. In International Conference on Research and Education in Robotics, pages 172–186. Springer, 2011.

[253] Guobin Shen, Zhuo Chen, Peichao Zhang, Thomas Moscibroda, and Yongguang Zhang. Walkie-markie: indoor pathway mapping made easy. In Proceedings of the 10th USENIX conference on Networked Systems Design and Implementation, pages 85–98. USENIX Association, 2013.

[254] Anshul Rai, Krishna Kant Chintalapudi, Venkata N Padmanabhan, and Rijurekha Sen. Zee: zero-effort crowdsourcing for indoor localization. In Proceedings of the 18th annual international conference on Mobile computing and networking, pages 293–304. ACM, 2012.

[255] Pengfei Zhou, Mo Li, and Guobin Shen. Use it free: instantly knowing your phone attitude. In Proceedings of the 20th annual international conference on Mobile computing and networking, pages 605–616. ACM, 2014.

[256] He Wang, Souvik Sen, Ahmed Elgohary, Moustafa Farid, Moustafa Youssef, and Romit Roy Choudhury. No need to war-drive: unsupervised indoor localization. In Proceedings of the 10th international conference on Mobile systems, applications, and services, pages 197–210. ACM, 2012.

[257] Justin Gregory Manweiler, Puneet Jain, and Romit Roy Choudhury. Satellites in our pockets: an object positioning system using smartphones. In Proceedings of the 10th international conference on Mobile systems, applications, and services, pages 211–224. ACM, 2012.

[258] Alex T Mariakakis, Souvik Sen, Jeongkeun Lee, and Kyu-Han Kim. Sail: single access point-based indoor localization. In Proceedings of the 12th annual international conference on Mobile systems, applications, and services, pages 315–328. ACM, 2014.

[259] Industrial camera systems. http://industrialcamera.net/security-surveillance-system-products-services/uav-detection/.

[260] Androflight. https://sites.google.com/site/androflight/home.

[261] Ieee drone detection. http://spectrum.ieee.org/automaton/robotics/drones/small-drone-detection-strategies, Februrary.

[262] NCC Group. http://tinyurl.com/j8u44sx.

[263] Drone detection issues. http://tinyurl.com/gsm4n3t.

[264] Kelvin Hughes drone detection. http://tinyurl.com/jvxj4kx.

[265] Detect inc. http://tinyurl.com/d3jmkys.

[266] Drone shield. http://tinyurl.com/h4gyahs.

[267] Detect inc. http://www.enterprisecontrol.co.uk/product_detail.php/anti-uav-defence-system-auds.

[268] Drone detector (orelia). http://tinyurl.com/jcmbmep.

[269] Dedrone. http://tinyurl.com/ztfl5v6.

[270] Min Goo Yoo and Sung Kyung Hong. Dynamic system identification and validation of a quadrotor uav. International Journal of Applied Engineering Research, 11(2):1089–1093, 2016.

[271] Faa: Pilot uas reports, March 2016.

[272] Dianne Feinstein. Reckless consumer drone use threatens public safety in california, October 2015.

[273] Corrosion resistant aerial covert unmanned nautical system (cracuns), March 2016.

[274] Joseph Serna. Lufthansa jet and drone nearly collide near lax, March 2016.

[275] Yin Chen, Dimitrios Lymberopoulos, Jie Liu, and Bodhi Priyantha. FM-based Indoor Localization. In MobiSys '12, pages 169–182, New York, NY, USA, 2012. ACM.

[276] OpenWRT. Sharing raw NMEA GPS data over the network with multiple clients. https://goo.gl/ctwCdD, 2018. [Online; accessed Sep 19, 2018].

[277] M. S. Arulampalam, S. Maskell, N. Gordon, and T. Clapp. A tutorial on particle filters for online nonlinear/non-Gaussian Bayesian tracking. IEEE Transactions on Signal Processing, (2):174–188, February 2002.

[278] C. Fernndez-Prades, C. Avils, L. Estove, J. Arribas, and P. Closas. Design patterns for GNSS software receivers. In 2010 5th ESA Workshop on Satellite Navigation Technologies and European Workshop on GNSS Signals and Signal Processing (NAVITEC), pages 1–8, December 2010.

[279] Adrian Crenshaw. Inside the atheros wi-fi chips. https://goo.gl/sLxVQS, 2018. [Online; accessed Sep 19, 2018].

[280] Linux Wireless. Ath9k device driver. https://goo.gl/i9Mwb8, 2018. [Online; accessed Sep 19, 2018].

[281] Ubiquiti. Ubiquiti networks community. https://goo.gl/p7ZqWF, 2018. [Online; accessed Sep 19, 2018].

[282] Intel. Intel nuc. https://goo.gl/uFQa4B, 2018. [Online; accessed Sep 19, 2018].

[283] Ettus Research. VERT2450 Antenna. https://goo.gl/VKo7wo, 2018. [Online; accessed Sep 19, 2018].

[284] WIME. Wime - wireless measurement and experimentation. https://goo.gl/LQr25K, 2018. [Online; accessed Sep 19, 2018].

[285] WIME. Gps simulator. https://goo.gl/kGBkux, 2018. [Online; accessed Sep 19, 2018].

[286] Xi Liu. Gps error sources. https://goo.gl/99pDCE, 2018. [Online; accessed Sep 19, 2018].

[287] Four-Faith. F7436 WiFi GPS device. https://goo.gl/8VBYj3, 2018. [Online; accessed Sep 19, 2018].

[288] NMEA. NMEA Sentense Description. https://goo.gl/DR5Jbz, 2018. [Online; accessed Sep 19, 2018].

[289] Atheros AR9331. https://goo.gl/LAjPGJ, 2018. [Online; accessed Sep 19, 2018].

[290] Catb gpsd. gpsd a GPS service daemon. http://www.catb.org/gpsd/, 2018. [Online; accessed Sep 19, 2018].

[291] GlobalSat. GlobalSat ND-105C Micro USB GPS Receiver. https://goo.gl/e1vw2T, 2018. [Online; accessed Sep 19, 2018].

[292] Diymall. Diymall Vk172 Dongle Glonass Ublox Support Windows. https://goo.gl/NzPggj, 2018. [Online; accessed Sep 19, 2018].

[293] Stratux. Stratux GPYes u-blox 7 GPS unit. https://goo.gl/t5SPpa, 2018. [Online; accessed Sep 19, 2018].

[294] Stratux. Stratux Vk-162 Remote Mount USB GPS. https://goo.gl/11iDV4, 2018. [Online; accessed Sep 19, 2018].

[295] Garmin. Understanding the accuracy of the GPS elevation reading. https://goo.gl/Xd3Kpp, 2018. [Online; accessed Sep 19, 2018].

[296] M. Zargari et al. A single-chip dual-band tri-mode cmos transceiver for ieee 802.11a/b/g wireless lan. IEEE Journal of Solid-State Circuits, 39(12):2239–2249, Dec 2004.

[297] M. Zargari et al. A dual-band cmos mimo radio soc for ieee 802.11n wireless lan. IEEE Journal of Solid-State Circuits, 43(12):2882–2895, Dec 2008.

[298] Dean Banerjee. PLL Performance Simulation and Design Handbook. National Products, 2017.

[299] Justin Gregory Manweiler, Puneet Jain, and Romit Roy Choudhury. Satellites in our pockets: An object positioning system using smartphones. In Proceedings of the 10th International Conference on Mobile Systems, Applications, and Services, MobiSys '12, pages 211–224, New York, NY, USA, 2012. ACM.

[300] E.J. Lefferts, F.L. Markley, and M.D. Shuster. Kalman filtering for spacecraft attitude estimation. Journal of Guidance, Control, and Dynamics, 5(5):417–429, 1982.

[301] S. Gezici, Zhi Tian, G. B. Giannakis, H. Kobayashi, A. F. Molisch, H. V. Poor, and Z. Sahinoglu. Localization via ultra-wideband radios: a look at positioning aspects for future sensor networks. IEEE Signal Processing Magazine, 22(4):70–84, July 2005.

[302] IEEE-ComSoc. The power of Wi-Fi. https://tinyurl.com/y7bvvbam, 2018. [Online; accessed Sep 19, 2018].